OUKA
The University of Osaka
Institutional Knowledge Archive

Title	Relationship between repetitive transcranial magnetic stimulation and microstructural property in the human brain
Author(s)	木村, 一皓
Citation	大阪大学, 2023, 博士論文
Version Type	
URL	https://doi.org/10.18910/92126
rights	
Note	

The University of Osaka Institutional Knowledge Archive : OUKA

https://ir.library.osaka-u.ac.jp/

The University of Osaka

Relationship between repetitive transcranial magnetic stimulation and microstructural property in the human brain

反復経頭蓋磁気刺激と脳の微細構造の関係

A DOCTORAL THESIS

SUBMITTED TO THE GRADUATE SCHOOL

OF FRONTIER BIOSCIENCES OF OSAKA UNIVERSITY

Ikko Kimura

March, 2023

Abstract

Repetitive transcranial magnetic stimulation (rTMS) can noninvasively modulate human brain activity. Since its development in the late 20th century, rTMS has been widely applied to reveal the contribution of each brain area to certain behavior and to treat neurological or psychiatric diseases. However, the substantial inter-individual variability in the after-effect of rTMS has been a major concern in applying rTMS for neuroscientific research and clinical practice for over the past ten years. For these backgrounds, the studies in this thesis investigate the relationship between the after-effect of rTMS and the microstructural property in the human brain, which can be noninvasively assessed with diffusion magnetic resonance imaging (dMRI).

In the first study, I investigated whether the microstructural property assessed with dMRI can predict the magnitude of the after-effect of intermittent theta burst stimulation (iTBS), which is one of the patterned rTMS protocols. iTBS has an advantage for relatively short stimulation duration compared to other rTMS protocols and is widely applied for both neuroscientific and clinical purposes. Here, I evaluated the after-effect of iTBS over the right primary motor cortex (M1) in each individual by assessing the change in amplitude of motor-evoked potential (MEP). Then, I examined the correlation between the MEP change and the fractional anisotropy (FA) values in the gray and white matter, evaluated by dMRI scans obtained on the day before the iTBS experiment. As a result, the early-phase (5–10 min post-iTBS) of the MEP change was significantly correlated with the FA values in the white matter. In contrast, the late phase (15–30 min post-iTBS) of the MEP change was correlated with the FA values on the right cerebral cortex. This study will be useful for developing the predictive indicator of rTMS after-effect with pre-measured MRI data.

In the second study, I investigated whether rTMS could, in turn, induce the microstructural changes after the stimulation. Previous studies have reported conflicting results regarding the microstructural changes in the human brain immediately after rTMS. Moreover, the change in this property has not been directly compared between the excitatory and inhibitory protocols of rTMS. Therefore, by using quadri-pulse stimulation (QPS), whose after-effect is relatively strong and robust compared to other rTMS protocols, I compared the FA or mean diffusivity (MD) values in the white matter, cerebral cortex, and subcortical structures before and after the excitatory (QPS5) and inhibitory (QPS50) protocols of QPS. As a result, I found that the FA and MD values in the cerebral cortex and white matter were not significantly changed either after QPS5 or QPS50. In contrast, the MD values in the bilateral cerebellum were decreased after both QPS5 and QPS50. These results suggest that microstructural changes may not be observed immediately after QPS in most of the areas in the human brain.

The results of these two studies will provide an important basis for future studies to establish a predictive-indicator of rTMS after-effect and to clarify the mechanisms evoked by rTMS throughout the brain.

Table of Contents

Abstract **2**

Table of Contents **4**

Chapter 1. General introduction **6**

1.1 Repetitive transcranial magnetic stimulation 9

1.1.1 Principles of transcranial magnetic stimulation 9

1.1.2 Protocols for repetitive transcranial magnetic stimulation 12

1.1.3 Synaptic plasticity: mechanisms behind repetitive transcranial magnetic stimulation 14

1.2 Principles of Magnetic Resonance Imaging 19

1.2.1 Two major pulse-sequences for magnetic resonance imaging 20

1.2.2 Principles of functional magnetic resonance imaging 21

1.2.3 Principles of diffusion magnetic resonance imaging 23

1.3 Functional connectivity 26

1.3.1 Methods to calculate functional connectivity from resting-state functional magnetic resonance imaging 27

1.3.2 Several concerns of functional connectivity assessed with resting-state functional magnetic resonance imaging 28

1.4 Neuroimaging methods to probe the microstructural properties of the human brain 32

1.4.1 Microstructures in the human brain 32

1.4.2 Noninvasive methods to reveal the microstructural properties of the human brain 33

1.4.3 Metrics derived from diffusion magnetic resonance imaging 35

Chapter 2. Microstructural properties of the human brain can predict the after-effect of intermittent theta burst stimulation **40**

2.1 Introduction 40

2.2 Materials and Methods 42

2.2.1 Participants 42

2.2.2 Transcranial Magnetic Stimulation 44

2.2.3 Electromyography 45

2.2.4 Motor Evoked Potential Analysis 45

2.2.5 Image acquisition 46

2.2.6 Image analysis 47

2.2.7 Statistical analysis 49

2.3 Results 50

2.4 Discussion 59

2.4.1 Significant increase in MEP amplitude post-iTBS 59

2.4.2 Negative correlations of regional WM FA with early-phase MEP amplitude change 60

2.4.3 Negative correlations of regional gray matter FA with late-phase MEP amplitude change 61
2.4.4 Microstructural properties may influence the after-effect of iTBS 62
2.4.5 Limitations 64
2.4.6 Conclusions 65

Chapter 3. Microstructural changes induced by quadripulse stimulation 66
3.1 Introduction 66
3.2 Validation on the efficacy of a new developed QPS stimulator 68
3.3 Materials and Methods 74
3.3.1 Participants 75
3.3.2 Quadripulse Stimulation 75
3.3.3 Image Acquisition 76
3.3.4 Image Analysis 78
3.3.5 Statistical Analysis 83
3.4 Results 85
3.4.1 The change of the microstructural property after quadripulse stimulation 86
3.4.2 The relationship between the change of the functional connectivity on the stimulated region and that of the microstructural property of the brain after quadri-pulse stimulation 99
3.4.3 Possible confounding factors both within and across the session 102
3.5 Discussion 106
3.5.1 No significant change in the microstructural property of the gray matter in the cerebral cortex after QPS 106
3.5.2 No significant change in the microstructural property of the white matter after QPS 108
3.5.3 Limitation 109
3.5.4 Conclusion 110

Chapter 4. General discussion and conclusion 111
4.1 Integrative Summary 111
4.2 Diffusion MRI as an indicator for microstructural properties 111
4.3 Potentiality of diffusion MRI as a predictive indicator of the rTMS after-effect 112
4.4 Potentiality of cortico-cortico paired associative stimulation as a neuromodulation tool to modulate the microstructures 113
4.5 Concluding remarks 113

Chapter 5. References 114

Chapter 6. Acknowledgement 132

Chapter 7. Achievements 134
7.1 Related to this thesis 134
7.2 Other achievements 135

Chapter 1. General introduction

Noninvasive neuromodulation techniques are important for clarifying the direct contribution of each brain region to specific behaviors. These techniques include repetitive transcranial magnetic stimulation (rTMS), which utilizes electromagnetic induction. This technique repeatedly activates the stimulated region to modulate the activity of that region. Since its development in the early 20th century (Pascual-Leone et al., 1994), rTMS has been used in psychological experiments (Hallett, 2007) and clinical trials for the treatment of neurological or psychiatric disorders (Lefaucheur et al., 2020). Moreover, rTMS has now been approved by the U.S. Food and Drug Administration for the treatment of depression and obsessive-compulsive disorder (Horvath et al., 2010). Therefore, rTMS would be one of the most prominent neuromodulation techniques for clinical application in the next decade.

However, one concern with applying rTMS for neuro-investigational or clinical purposes is that its after-effects show substantial inter-individual variability (Ridding and Ziemann, 2010). This means that rTMS is effective for some participants but is not for others, requiring large sample sizes to draw scientific conclusions (López-Alonso et al., 2014). One way to solve this problem is to create a biomarker that predicts the effectiveness of rTMS for each region and then to select participants for whom rTMS is effective, although in some cases the selection bias should be taken into account. While age, sex, and genetic polymorphisms have been proposed as potential factors to determine the after-effect of rTMS (Corp et al., 2020; Ridding and Ziemann, 2010), these factors are general factors of synaptic plasticity and do not necessarily define the effectiveness of rTMS on each region.

Previous studies have addressed this issue by examining the functional connectivity (FC) on the stimulated region. FC is determined by the correlation of time-series between two regions. Intrinsic FC can be assessed by scanning functional magnetic resonance imaging (fMRI) while subject at rest (resting-state fMRI; rsfMRI; (Smith et al., 2009)). One study

showed that intrinsic FC can be a predictive biomarker for the efficacy of rTMS over the primary motor cortex (M1) (Nettekoven et al., 2015). However, another study failed to predict the rTMS after-effect over this region with this measure (Cárdenas-Morales et al., 2014). This inconsistency is partly due to the high intra-individual variability of FC. Indeed, FC can vary depending on several factors such as sleepiness (Stoffers et al., 2015) and mental state (Buckner et al., 2013). Moreover, though all participants are asked to simply rest, participants can have several different mental states across sessions (Gonzalez-Castillo et al., 2021).

In contrast, the microstructural properties of the brain, which can be noninvasively assessed with diffusion MRI (dMRI; (Basser et al., 1994)), are robust to sleepiness and mental states. Measures derived from dMRI have clarified the relationship between the microstructural properties and the inter-individual behavioral variability (Genon et al., 2022) or between those and the degree of neuroplasticity (Soulard et al., 2020) in the human brain. In addition, these measures have detected the acute phase (e.g., around one hour after the start of training) of microstructural changes in the living human brain induced by behavioral training (Sagi et al., 2012; Sampaio-Baptista et al., 2021; Scholz et al., 2009; Tavor et al., 2020). Taken together, dMRI has the potential to be a useful biomarker for predicting and assessing the after-effect of rTMS.

Therefore, in this thesis, I addressed two main questions using dMRI:

1. Does the microstructural property determine the effectiveness of rTMS? In the first study (Chapter 2), I attempted to clarify the correlations between the microstructural property of the human brain and effectiveness of intermittent theta-burst stimulation (iTBS). iTBS is one of the rTMS protocols that is easily applied to patients because of its short stimulation duration. Revealing the relationship between the microstructural property in the human brain and the

degree of the after-effect of iTBS is crucial for developing the predictive biomarker of the effectiveness of iTBS on each region for each individual.

2. If the microstructural property defines the effectiveness of rTMS, does rTMS in turn change this property in the human brain? In the second study (Chapter 3), I attempted to assess the microstructural change induced by quadripulse stimulation (QPS), whose after-effect is strong and robust compared to other rTMS protocols (Hamada et al., 2007; Tiksnadi et al., 2020). Furthermore, I investigated its relationship with functional changes assessed with rsfMRI.

In the rest of this chapter, I explain the backgrounds and principles of the first and second studies of this thesis. This overview includes (1) rTMS, (2) FC, and (3) the neuroimaging methods to noninvasively probe the microstructural properties of the brain.

1.1 Repetitive transcranial magnetic stimulation

rTMS modulates the brain activity even after the stimulation. This method utilizes the nature of synaptic plasticity, which was evoked by the repetitive activation of neurons (Citri and Malenka, 2008). In this section, I first provide the basic principles of TMS, on which rTMS is based. Then, I describe the four major protocols of rTMS, including intermittent theta burst stimulation (iTBS) and quadripulse stimulation (QPS), which were applied in the first and second studies, respectively. Finally, I explain the supposed mechanisms behind the after-effect of rTMS.

1.1.1 Principles of transcranial magnetic stimulation

rTMS activates the brain repeatedly and noninvasively by transcranial magnetic stimulation (TMS). A coil, which is equipped with the central unit of TMS-machine (Figure 1.1A), is placed on the head to noninvasively stimulate the target area of the brain. Inside the coil are wounded copper-wires, and electric pulses are transmitted to that wire from the central unit (Figure 1.1A). Generally, this electric pulse rises to the peak and back to the baseline within 1 ms, and this rapid change induces the magnetic field up to around 2.5T. That huge change in magnetic field around the coil evokes electric current in the neural cells nearby the coil (Figure 1.1B) following Faraday's principle of electromagnetic induction (Faraday, 1839).

Brain areas affected by TMS

The electromagnetic induction decays rapidly in the order of cubic distance from the coil. This means that a TMS is less likely to activate the brain areas far from the coil. The area affected by TMS depends on the intensity of electric pulse and the form of the coil (Deng et al., 2013). Nevertheless, TMS generally stimulates the brain region 1.5–2cm deep from the scalp with the surface area 2–4cm^2 (Hallett, 2007).

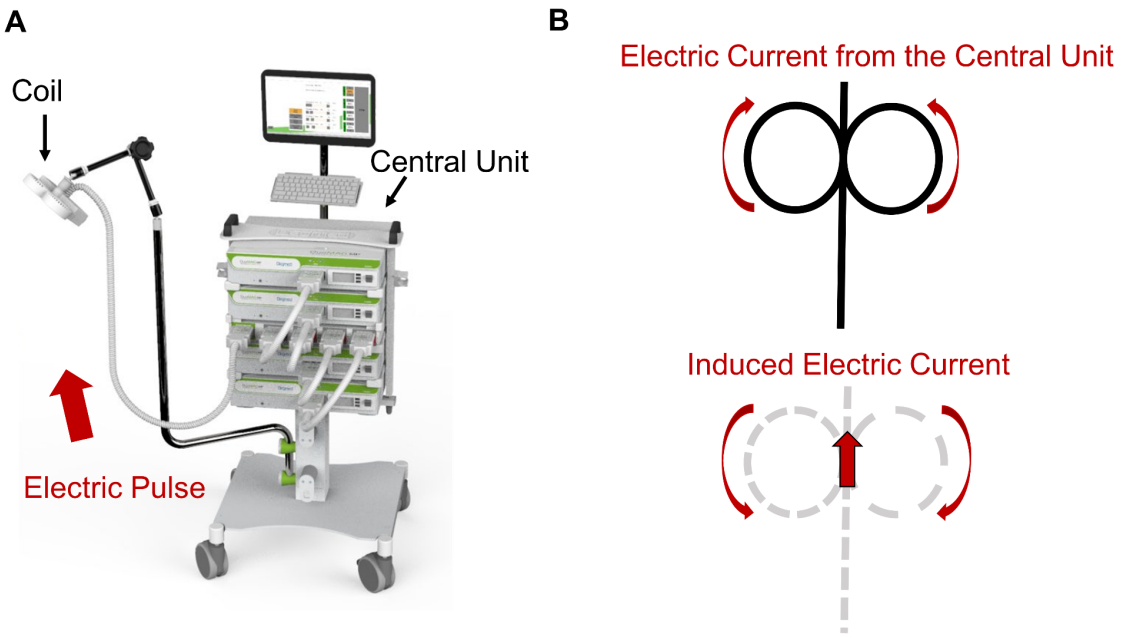

Figure 1.1 Transcranial magnetic stimulation (TMS) (A) The components of TMS-machine. (B) The direction of electric current transmitted by the central unit and the induced electric current nearby the coil.

The electric pulse-waveform transmitted to the coil also determines the neurons affected by rTMS (Hamada et al., 2013). The pulse-waveform can be divided by two major types: monophasic and biphasic pulses. The electric pulse to the coil induces the current to one direction and, then, to the inverse direction. A monophasic pulse induces the former current rapidly and the latter one gradually (Figure 1.2A). This is intended to make the effect induced by the latter less effective than the former. In contrast, a biphasic pulse induces the latter with the rate nearly the same as the rate of the former (Sommer et al., 2006). Both pulses induce current in both directions, but the main induced currents in monophasic and biphasic pulses are towards the former (Figure 1.2A) and latter (Figure 1,2B) direction, respectively (Sommer et al., 2006). Though the dissociation on the main induced current direction between a monophasic and biphasic pulse is not clear, this was assumed to be because of the timing and the intensity of the latter current. The latter current decreases the

membrane potential of the neurons increased by the former current and determines the degree of depolarization on these neurons (Sommer et al., 2018).

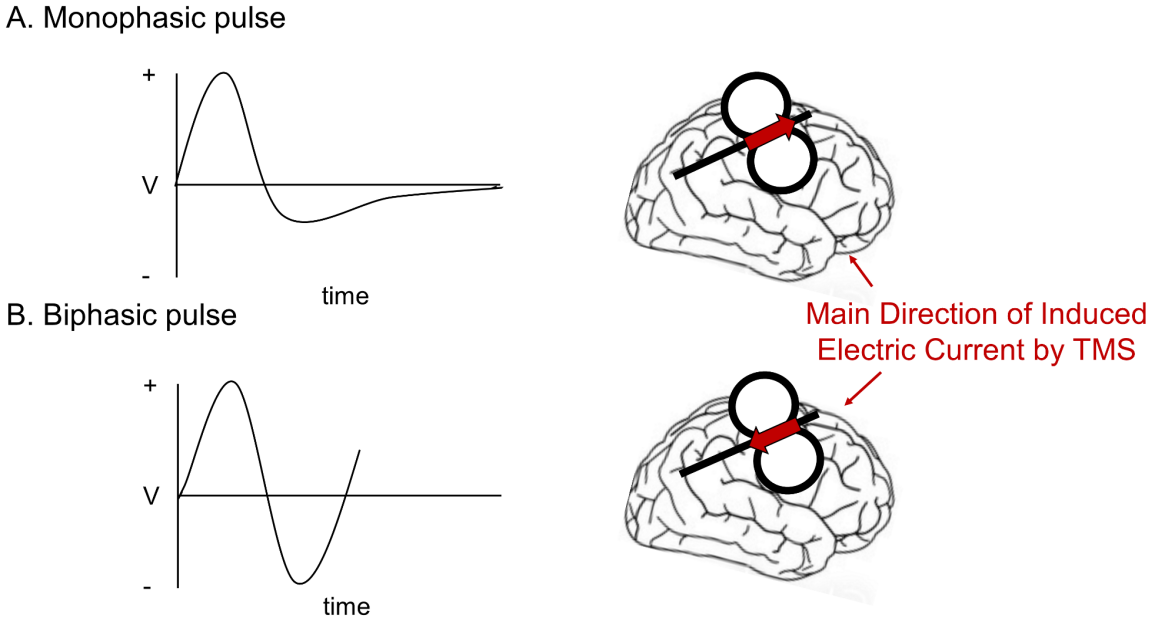

Figure 1.2 The difference of (A) monophasic and (B) biphasic electric pulses. The figures on the left side show the waveform of each pulse. The horizontal axes indicate the time-course of the change of electric pulse, while the vertical axes indicate the induced currents near the coil. The figures on the right side show the main direction of induced electric currents in the brain.

Though rTMS with a monophasic pulse is generally more effective than the one with biphasic pulse (Arai et al., 2007; Nakamura et al., 2016), a biphasic pulse is frequently used in high-frequency rTMS. This is because a biphasic pulse can stimulate the brain more frequently than a monophasic pulse since the pulse-width of a biphasic pulse is narrower than that of a monophasic one. Besides whether the pulse is monophasic or biphasic, pulse width and the maximum rate of the change of electric current in the electric pulse transmitted by a TMS-stimulator were also shown to determine the strength of electromagnetic induction in the brain (Drakaki et al., 2022; Sommer et al., 2018).

1.1.2 Protocols for repetitive transcranial magnetic stimulation

Several protocols have been developed for rTMS. Here, I overview the four major protocols of rTMS: conventional rTMS, paired-associative stimulation (PAS), TBS, and QPS (Figure 1.3).

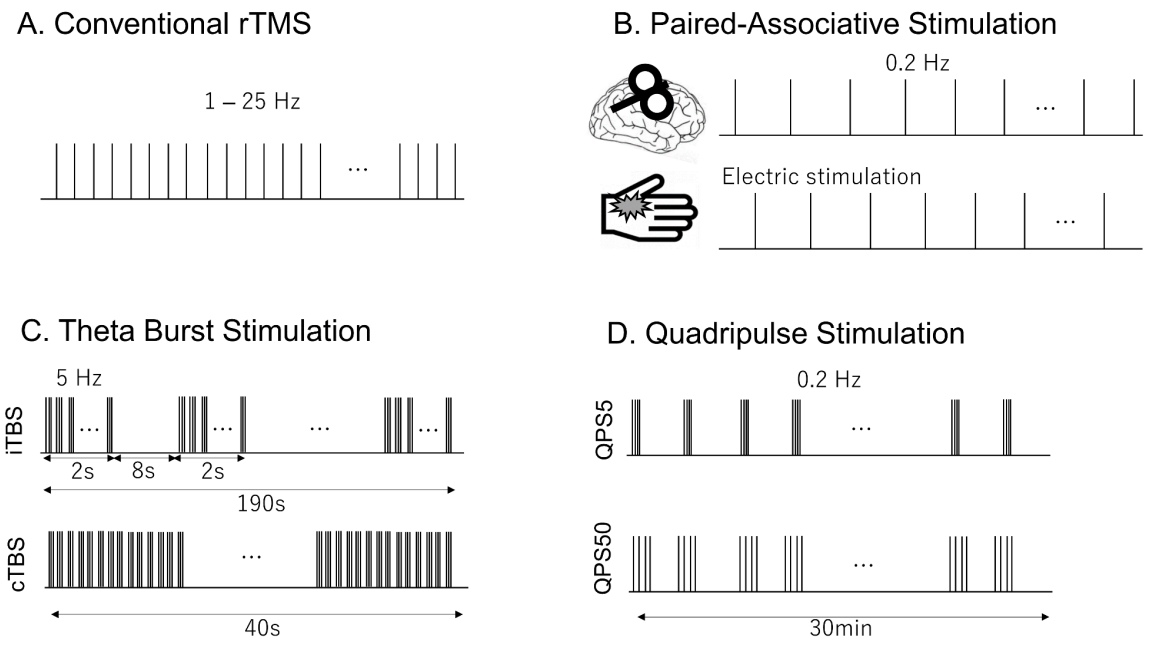

Figure 1.3 Overview of the four major protocols of rTMS. (A) Conventional rTMS (B) Paired-Associative Stimulation (C) Theta Burst Stimulation (D) Quadripulse Stimulation.

conventional rTMS protocols

Conventional rTMS repeatedly stimulates the brain with a fixed frequency (1 – 25 Hz; Figure 1.3A). rTMS with low frequency (typically 1Hz) suppresses the activity of the stimulated region, while rTMS with high frequency (typically more than 5Hz) enhances that activity (Pascual-Leone et al., 1994). Low-frequency rTMS is applied to the brain continuously, while high-frequency rTMS is applied intermittently due to the coil-overheating. Specifically, a typical high-frequency rTMS stimulates the brain for 2–5s every 30–60s (Oberman, 2014). The after-effect of rTMS sustains from half to full-length of the stimulation length (Oberman, 2014).

paired-associative stimulation

PAS targets the M1 and the stimulations by TMS are associated with the afferent electric stimulation of the target muscle (Figure 1.3B). The mechanism behind PAS is a spike timing-dependent plasticity (STDP; (Caporale and Dan, 2008)). STDP depends on the timing of the activation of the pre- and post-synapse. While LTP occurs when the activation of pre-synapse precedes the activation of post-synapse, LTD occurs when the activation of post-synapse precedes the activation of pre-synapse. This protocol typically stimulates the brain every 5s for 15min.

Cortico-cortical PAS is the derivative of PAS, placing two coils on the head. Instead of inducing the electric stimulation on the target muscle, this protocol stimulates the brain with TMS. This method can be used outside M1 and bidirectionally modulates the network between the two regions where the two coils are placed (Romei et al., 2016).

theta-burst stimulation

TBS intends to replicate the bursts in the hippocampus with theta frequency ,which is crucial in evoking synaptic plasticity (Larson and Lynch, 1986). TBS evokes three 50Hz-pulses with theta frequency (i.e., 5Hz) (Figure 1.3C). While applying TBS continuously suppresses the brain activity of the stimulated region, applying TBS intermittently (typically 2s train with inter-train interval of 8s) enhances the brain activity (Huang et al., 2005). The former and latter protocols are termed continuous TBS (cTBS) and intermittent TBS (iTBS), respectively.

The strength of TBS is that the short stimulation-length can induce long after-effects. Just 40s of cTBS or 3min of iTBS are required to change the brain activity for 30–45min, while stimulation-length more than 30min is required for conventional rTMS for such length

of the after-effect (Oberman, 2014). Due to this simplicity, both cTBS and iTBS have gained attention for their clinical applications over the past decade (Blumberger et al., 2018; Chen et al., 2021; Oberman et al., 2011).

quadripulse stimulation

QPS stimulates the brain every 5s with four pulses for 30min (Figure 1.3D). QPS with short interpulse intervals (less than 15 ms) enhances the brain activity of the stimulated region. In contrast, QPS with long interpulse intervals (more than 20 ms) suppresses that activity (Hamada et al., 2008). In most studies, the interpulse interval of 5 ms (QPS5) and 50 ms (QPS50) is applied for facilitatory and inhibitory protocols of QPS, respectively, since these two protocols showed the strongest after-effect (Hamada et al., 2008).

The advantage of QPS is its strength and robustness of the after-effect. Its after-effect was shown to last more than an hour after the stimulation (Hamada et al., 2008) and the inter-individual variability of its after-effect was reported to be small (Nakamura et al., 2016). Moreover, the after-effect of QPS was shown to be stronger and more robust than that of PAS (Hamada et al., 2007) or that of TBS (Tiksnadi et al., 2020). Therefore, QPS would be one of the most promising neuromodulation techniques (Matsumoto and Ugawa, 2020).

1.1.3 Synaptic plasticity: mechanisms behind repetitive transcranial magnetic stimulation

Synaptic plasticity plays a pivotal role in the after-effect of rTMS. Several studies showed that the blockade of *N*-methyl-D-aspartate (NMDA) receptors diminishes the after-effect of rTMS (Huang et al., 2007; Stefan et al., 2002; Teo et al., 2007). An NMDA receptor is specifically important for long-term plasticity, which is one form of synaptic plasticity. Therefore, this plasticity has long been assumed to play a major role in the rTMS after-effect (Reti, 2015).

On the contrary, one study reported that the NMDA receptor antagonist did not diminish the after-effect of 5Hz rTMS with low stimulus intensity (Sommer et al., 2013). This study implies that the after-effect of rTMS might be sustained by several mechanisms other than long-term plasticity, at least in some protocols. Besides long-term plasticity, short-term plasticity is also included in synaptic plasticity and this type of plasticity might also contribute to the after-effect of rTMS (Ugawa, 2012). I detail these two forms of plasticity below.

short-term plasticity

Short-term plasticity occurs during or after the stimulation and lasts on the order of milliseconds to minutes (Zucker and Regehr, 2002). Several functions are included in this type of plasticity: synaptic facilitation, synaptic augmentation, synaptic potentiation, and synaptic depression.

Synaptic facilitation enhances the calcium level of the pre-synapse. The increase of the calcium level by the action potential in pre-synapse lingers for a certain period. If the subsequent action potential arrives at a presynaptic terminal soon enough, the increase in the calcium level is summed to the increase evoked by the previous action potential. This gradual increase of the calcium level enhances the release of neurotransmitters from pre-synapse.

Synaptic augmentation also increases the release of neurotransmitters from pre-synapse. This enhancement was proposed to be mediated by the pre-synaptic protein termed munc-13 (Zhou et al., 2013), which is activated by the increase of calcium level in pre-synapse. These two mechanisms diminish right after the stimulation and are less likely to contribute to the after-effect of rTMS for more than a minute.

In contrast, synaptic potentiation lasts more than minutes. This mechanism also facilitates the release of neurotransmitters in pre-synapse, but this is mediated by several

kinases in the presynapse. Since this mechanism requires several activations of kinases, more times are required than those required for synaptic facilitation or augmentation to occur, but this effect sustains tens of seconds to minutes. This process is also called post-tetanic potentiation and was proposed to be involved in the after-effect of excitatory rTMS (Sommer et al., 2013).

Synaptic depression is caused by the shortage of neurotransmitters in the pre-synapse (Betz, 1970). Repetitive activation of pre-synapse releases neurotransmitters frequently. When that release is frequent enough, the neurotransmitters are released faster than the reuptake of neurotransmitters in pre-synapse. As a result, the release of neurotransmitters gradually decreases and post-synapse becomes less sensitive to the activity of pre-synapse.

long-term plasticity

A long-term plasticity also occurs after the repetitive activation of the human brain, whose effect prolongs longer (minutes–weeks) than that of short-term plasticity (milliseconds–minutes). Though the mechanisms induced in inhibitory neurons for long-term plasticity remain to be elucidated, several studies have clarified those in excitatory, or glutamatergic, neurons (Malenka and Bear, 2004).

Glutamatergic neurons have two major ionotropic receptors; α-amino-3-hydroxy-5-methyl-4-isoxazolepropionic acid (AMPA) and NMDA receptors. The glutamate released by the pre-synapse binds both two receptors in post-synapse. Under this condition alone, while an AMPA receptor opens its channel, an NMDA receptor does not. This is because the pore of an NMDA receptor is blocked by the magnesium ion at the normal state. The inflow of positive ions through AMPA receptors increases the membrane potential of post-synapse. When the membrane potential depolarizes, the magnesium at the NMDA receptor is dislocated and the NMDA receptor allows the inflow of calcium towards

the post-synapse. Then, the increase in calcium level at post-synapse, in turn, evokes several steps required for long-term plasticity. Therefore, NMDA receptors in post-synapse play a fundamental role in long-term plasticity.

Long-term plasticity can be divided by the direction of change (facilitation or suppression) and the onset time (early or late). The plasticity facilitating and suppressing the brain activity are termed long-term potentiation (LTP) and long-term depression (LTD), respectively. In the early LTP, AMPA receptors in post-synapse are phosphorylated (i.e., upregulated) and the number of AMPA receptors in post-synapse increases. In the late LTP, the gene transcriptions related to synaptic plasticity are modulated. These changes in transcriptions not only increase the number of AMPA receptors but also modulate the structure of neurons, such as increasing the surface area and the number of dendrites of the post-synapse connecting to the pre-synapse (Engert and Bonhoeffer, 1999).

In contrast, the mechanisms behind LTD are more complicated and less clear (Malenka and Bear, 2004). The different mechanisms are induced by LTD in different regions. For example, LTD in cerebellum was shown to be mediated by the metabotropic glutamate receptor in post-synapse (Vogt and Canepari, 2010), while that in other brain regions was shown to involve the cannabinoid receptor in pre-synapse (Sjöström et al., 2003). Nevertheless, several animal studies confirmed that, in early LTD, the number of AMPA receptors in post-synapse is decreased by the phosphorylation (i.e., downregulation) of AMPA receptors in post-synapse, which was opposed to the mechanisms evoked by early LTP (Malinow and Malenka, 2002). As in late LTP, late LTD also changes the gene transcriptions, however, which expressions of protein are modulated are less clear (Purves, 2017).

The precise mechanisms determining LTP and LTD are still not clear. One explanation is that the direction of the plasticity is dependent on the membrane potential at

post-synapse. If that membrane potential is high enough, the magnesium of an NMDA receptor is fully unblocked. In contrast, when the potential at post-synapse is not high enough, the magnesium of an NMDA receptor is partially unblocked. Several studies suggest that the full dislocation of magnesium from an NMDA-receptor induces LTP, whereas the partial dislocation induces LTD. This hypothesis has long been known as the Bienenstock-Cooper-Munro theory (Cooper and Bear, 2012). On the other hand, several animal studies suggest that the rate or the total amount of inflow of calcium to the post-synapse is important (Huang et al., 2011). While the rapid rate of the increase of calcium at post-synapse was shown to evoke LTP, the total amount of the calcium was reported to evoke LTD.

1.2 Principles of Magnetic Resonance Imaging

Magnetic resonance imaging (MRI) can noninvasively explore the functions and structures of the human brain. This technique utilizes the magnetic resonance phenomenon of hydrogen. First, MRI emits the radio-frequency (Rf) pulse from the transmit coil. This pulse penetrates the tissue in the scanner and excites the hydrogen which precesses at the same frequency as the Rf pulse. This precessing hydrogen emits the signal called free-induction decay (FID) signal. After the Rf pulse vanishes, the hydrogen begins to return to its original state and the FID signal gradually decays. The FID signal can be detected by the other coil equipped with an MRI scanner (a receiving coil), and is utilized to reconstruct the image in the tissue.

The signal S obtained from the receiving coil can be described as the following formula (Figure 1.4):

$$S = M_0 (1 - e^{-TR/T1}) e^{-TE/T2} \qquad (1\text{-}1)$$

TR is the time to emit the Rf pulse and the next Rf pulse (repetition time), while TE is the time to detect the FID signal after the emission of the Rf pulse (echo time). T1 and T2 are the time constants. $(1 - e^{-TR/T1})$ shows that the FID signal increases if more time is taken to excite the hydrogen. In contrast, $e^{-TE/T2}$ indicates that the FID signal decays over time after the emission of the Rf pulse. This signal decay occurs because the coherence of the precession of hydrogen gradually decreases after the excitation and this decrease of the coherence is occurred due to (1) the inhomogeneity of the external magnetic field and (2) the interactions between hydrogens (Hashemi et al., 2012).

In the rest of this section, I firstly explain the two major pulse-sequences for MRI, namely spin-echo (SE) and gradient-echo (GRE) sequences. Then, I show the basic principles of fMRI and dMRI, which were applied in the study of Chapter 3 and Chapter 2 and 3, respectively.

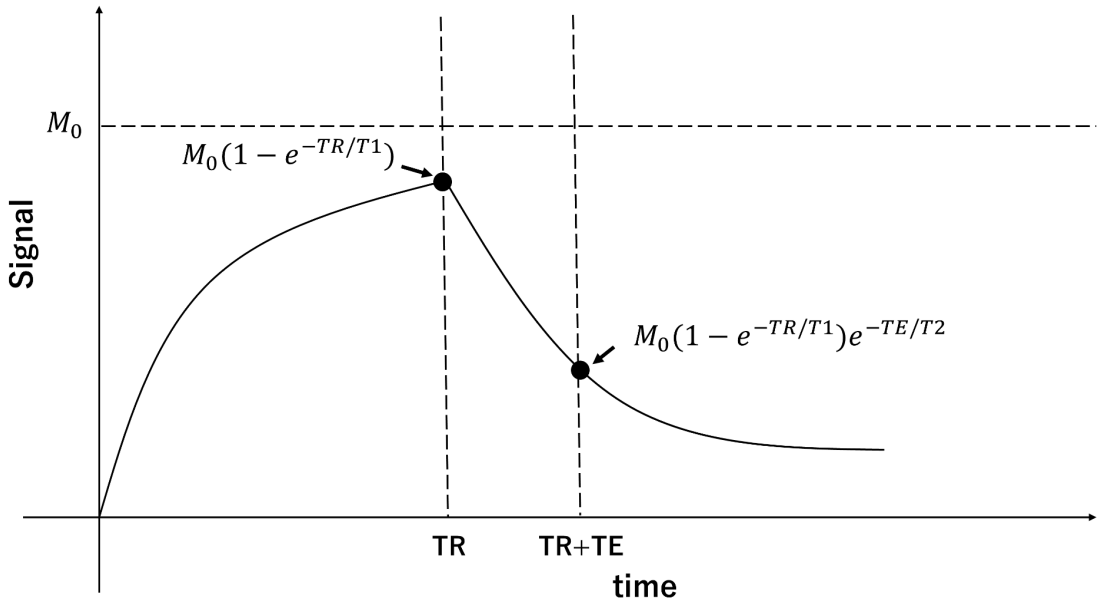

Figure 1.4 The signal obtained by the receiving coil changing TR and TE. The x-axis indicates the time-course, while the y-axis indicates the intensity of the signal. TR and TE are the time to emit the Rf pulse and the next Rf pulse (repetition time) and the time to detect the signal after the emission of the Rf pulse (echo time).

1.2.1 Two major pulse-sequences for magnetic resonance imaging

The contrast of the signals obtained by MRI is determined by when and how an Rf pulse penetrates to the tissue. Pulse-sequences can be divided by two major subsets: SE and GRE sequences. A SE sequence is composed of two Rf pulses: 90° and 180° Rf pulse (Figure 1.5A). A 90° Rf pulse tilts the spin of hydrogen nuclei by 90°. Though the FID signal gradually decays after the Rf pulse stops, by adding the 180° Rf pulse at the time τ after the 90° Rf pulse, the amplitude of the FID signal increases at the time 2τ (Figure 1.5A). This increase occurs because the coherence of precession is recovered at this time by the 180° Rf pulse (Hashemi et al., 2012).

In contrast, a GRE sequence utilizes α° Rf pulse and reversed gradient magnetic field instead of 90° and 180° Rf pulses, respectively (Figure 1.5B). This pair also increases the amplitude of the FID signal as with a SE sequence, but the recovery of coherence of the precession is imperfect. Due to this imperfection, this sequence is sensitive to the local

inhomogeneity of the magnetic field. Another feature of a GRE sequence, compared to a SE sequence, is that its acquisition time is fast since the FID signal magnifies faster in a GRE sequence than in a SE sequence. Most fMRI studies apply GRE sequences. This is because fMRI utilizes the local inhomogeneity of the magnetic field caused by the hemoglobin without oxygen (deoxy-Hb) and TR is shorter (i.e., more samples can be obtained in a certain amount of time) in a GRE sequence (Huettel et al., 2009). In contrast, most dMRI studies apply a sequence based on a SE sequence since the signal loss induced by the local inhomogeneity of the magnetic field is less and the signal-to-noise ratio is higher in a SE sequence than in a GRE sequence (Johansen-Berg and Behrens, 2013).

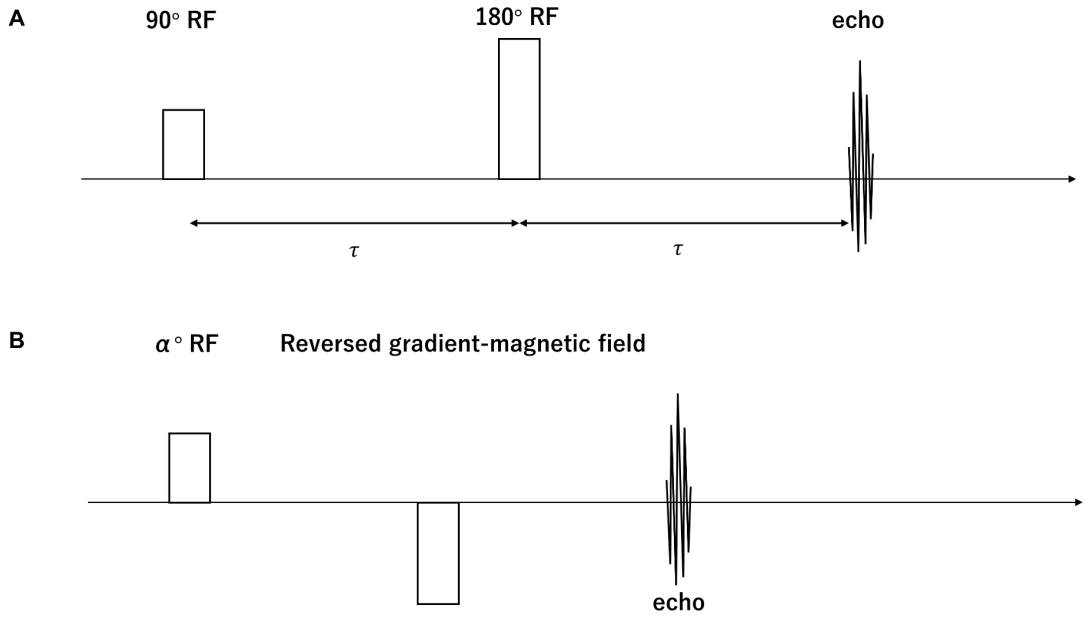

Figure 1.5 Pulse sequence of a spin-echo sequence (A) and a gradient-echo sequence (B). While a spin-echo sequence is constituted by two radio-frequency (Rf) pulses, a gradient-echo sequence is composed of one Rf pulse and one gradient magnetic field.

1.2.2 Principles of functional magnetic resonance imaging

The method to quantitatively evaluate the brain activity is crucial for clarifying the role of each brain region. In the early 1990s, Ogawa and colleagues found the activation in each

region can be inferred by assessing the signal obtained with fMRI (Ogawa et al., 1990). The advantage of fMRI, compared to other modalities, such as electroencephalography (EEG), is its high spatial resolution. While the spatial resolution of EEG is several centimeters, that of fMRI is 0.5–4 mm (Huettel et al., 2009). Moreover, fMRI can investigate neural activity deep in the brain, while EEG cannot. From below, I illustrate the principles of this method.

fMRI utilizes the difference of signal between a hemoglobin with oxygen (oxy-Hb) and deoxy-Hb in vein. This difference occurs because magnetization, which lowers FID signal, is different between oxy- and deoxy-Hb. Magnetization changes the local magnetic field of the tissue by the following equation:

$$B = (1 + \chi) H \qquad (1\text{-}2)$$

Here, B is the induced magnetic field, χ is the magnetic susceptibility of a material, and H is the magnetic field strength that the material is exposed to. While materials with $\chi < 0$ induce low magnetization (diamagnetic), those with $\chi > 0$ induce high magnetization (paramagnetic). oxy-Hb and deoxy-Hb are diamagnetic and paramagnetic, respectively, which means that the signal of deoxy-Hb is lower than that of oxy-Hb.

The neural activation increases the blood flow nearby the region (Huettel et al., 2009). Though the exact mechanism of this increase is still less clear, the blood flow was supposed to be enhanced by the several messengers, namely nitric oxide and adeno triphosphate, or the activation of astrocytes induced by the neural activation of nearby region (Huettel et al., 2009). Due to this increase, the supply of oxy-Hb outweighs the demand of the neural cells. As a result, the concentration of oxy-Hb in the vein near these neural cells increases, which, in turn, increases the signal in the vein. This signal is termed blood oxygen-level dependent (BOLD) signal and the neural activity can be inferred from this signal. The ideal time-course

of changes on this signal is shown in Figure 1.6.

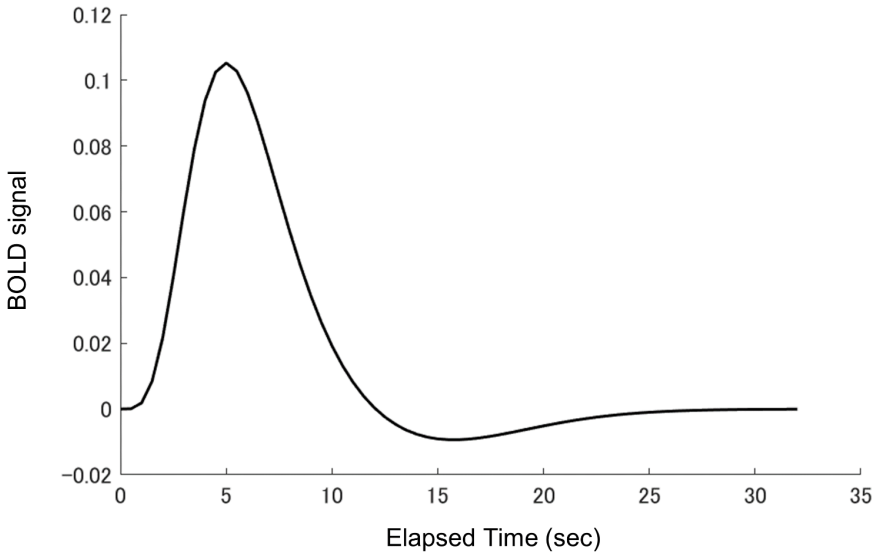

Figure 1.6 Ideal blood-oxygen level dependent (BOLD) signal after the neural activation. X-axis indicates the time-course after the neural activations, while the y-axis indicates the BOLD signal nearby the neurons.

1.2.3 Principles of diffusion magnetic resonance imaging

dMRI measures the loss of signals caused by the movement of water in each voxel. Typical dMRI sequence is called a single-shot SE echo-planar-imaging sequence (Johansen-Berg and Behrens, 2013), which is based on a SE sequence. As described in section 1.2.1, a SE sequence is composed of two Rf pulses; 90° and 180° Rf pulses (Figure 1.7A). A single-shot SE echo-planar-imaging sequence adds one pair of motion probing gradients (MPG) in one direction to a SE sequence (Figure 1.7B).

By adding MPG, the diffusivity of the water of that direction in each voxel can be probed. The first MPG deviates the phase of the spin of the hydrogen nuclei. If that nuclei does not move in the tissue, the deviation of these phases is aligned by the second MPG,

whose direction is the inverse of the first MPG. In contrast, if the nuclei moves substantially, these phases cannot be aligned by the second MPG, because the second MPG at the different location provides different magnitudes of the gradient of the magnetic field from the one at the original location. The deviation of the phases is reflected by the attenuations of the signal in the FID signal at 2τ. In this way, dMRI informs the water diffusivity in each voxel.

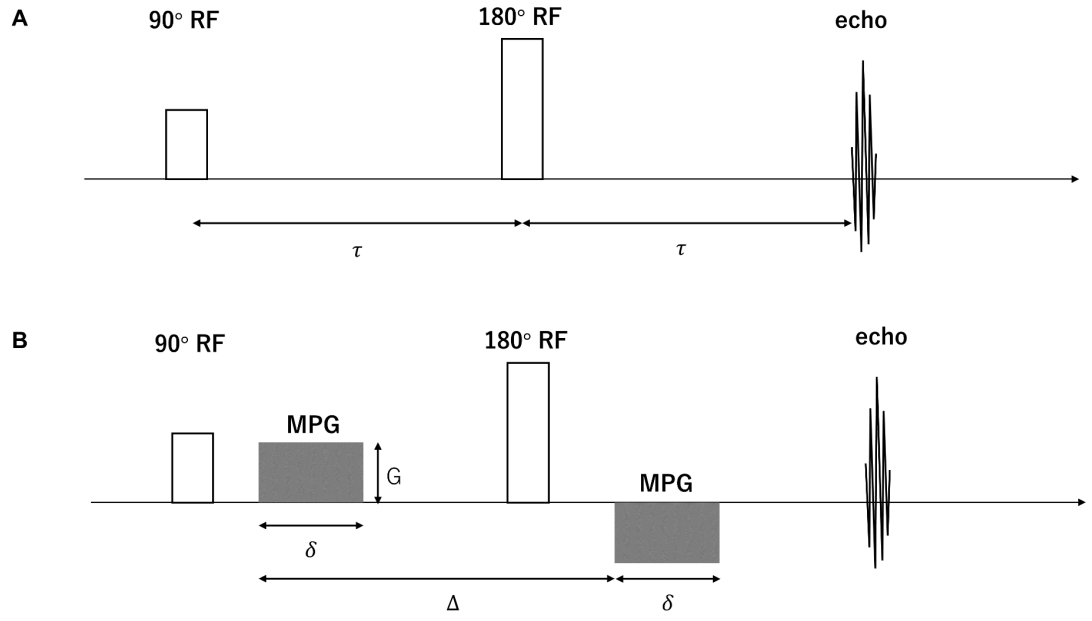

Figure 1.7 Typical pulse sequence of diffusion MRI (dMRI). (A) depicts the pulse sequence for spin-echo, on which the typical dMRI pulse sequence is based. This pulse sequence is constituted by two radio-frequency (Rf) pulses. (B) shows the typical sequence of dMRI, adding one pair of motion probing gradients (MPG) to the pulse sequence for spin-echo.

Under the condition that water can diffuse freely, the diffusivity of the water follows normal distributions and the signal decay produced by MPG can be generally described as the following equation:

$$log(\frac{S}{S_0}) = -\int_0^{\Delta+\delta}\left[\int_0^{t'}\gamma \cdot G(t'')dt''\right]dt' \cdot D \cdot \int_0^{\Delta+\delta}\left[\int_0^{t'}\gamma \cdot G(t'')dt''\right]dt' \quad (1\text{-}4)$$

S and S_0 represents the signal with and without MPG, respectively. γ denotes the gyromagnetic ratio, while G(t) represents the gradient field function. D is the diffusion tensor

as follows:

$$\begin{bmatrix} D_{xx} & D_{xy} & D_{xz} \\ D_{yx} & D_{yy} & D_{yz} \\ D_{zx} & D_{zy} & D_{zz} \end{bmatrix} \quad (1\text{-}5)$$

For example, D_{xx} denotes the diffusion coefficient when MPG was applied in the x-axis. If MPG is applied in the x-axis with the magnitude *G*, equation 1-4 can be simplified as the following:

$$log(\frac{S}{S_0}) = -\gamma^2 D_{xx} G^2 \delta^2 (\Delta - \frac{\delta}{3}) \quad (1\text{-}6)$$

And when *b* is defined as:

$$b = \gamma^2 G^2 \delta^2 (\Delta - \frac{\delta}{3}) \quad (1\text{-}7)$$

Equation 1-6 can be simply described as follows:

$$log(\frac{S}{S_0}) = -bD_{xx} \quad (1\text{-}8)$$

This equation is known as the Stejskal-Tanner equation (Stejskal and Tanner, 1965) and *b* in the equation 1-7 is called b-factor or b-value. The equation 1-8 has been the basis for modeling the diffusivity of the water from the dMRI signal.

1.3 Functional connectivity

The brain communicates across regions (Buzsaki, 2006). Over the past few decades, these inter-regional communications have been thought to mediate the mental process, such as perception (Friston, 2012), consciousness (Tononi et al., 2016), memory (Rabinovich and Varona, 2011), and action (Friston et al., 2011). Moreover, the disruptions of the inter-regions communications have long been thought to induce several neurological and psychiatric

diseases. For example, the motor and non-motor symptoms of Parkinson's Disease are caused by the disruptions of interactions between frontal areas and striatum (Bloem et al., 2021). The progression of Alzheimer Disease is also believed to be caused by the decrease of communications within the default mode network (Dennis and Thompson, 2014). Therefore, investigating the inter-regional brain communications is crucial to clarify the neural correlates of human behavior and the pathogenic mechanisms of neurological or psychiatric diseases. The degree of inter-regional brain communications are termed functional connectivity (FC; (Bullmore and Sporns, 2009)) and many studies investigate the FC at rest because of its simplicity (Koike et al., 2021). In the rest of this section, I first provide the methods to calculate FC from rsfMRI, which is applied in Chapter 3. Then, I overview the general limitations of FC calculated by rsfMRI.

1.3.1 Methods to calculate functional connectivity from resting-state functional magnetic resonance imaging

The most classical way of quantifying FC is to calculate the correlations between the time-series of two regions from fMRI. This method requires two steps: the definition of the interested region (region of interest; ROI) and calculating the correlations. As for the ROI definitions, ROIs can be typically determined from the predefined atlas (Glasser et al., 2016b) or from the results of the task fMRI (Watanabe et al., 2014). Another way is to define each voxel as a ROI (dense connectome; (Smith et al., 2013)) or to define one region from the predefined atlas and the other as each other voxel in the whole brain (seed-based correlation analysis; (Bijsterbosch et al., 2017)).

There are also several methods to calculate the correlations between the two regions. The most typical way is to calculate Pearson's correlation coefficient (Bijsterbosch et al., 2017). Another method is to calculate the partial correlation of the interested regions to alleviate the indirect correlations between the two regions (Smith et al., 2011). Though there

are more other ways to calculate the correlations between the two regions (Smith et al., 2011), the simulation study showed that the accuracy of the most typical method (i.e., Pearson's correlation coefficient) was comparable to or better than that of other methods (Smith et al., 2011). Due to this, most studies use Pearson's correlation coefficient to calculate FC (Koike et al., 2021).

One drawback of quantifying FC by calculating the correlations between the time-series of two regions is that the FC can be biased by the definition of interested regions. In fact, a slight difference of the definition of a seed was shown to change the functional connectivity in seed-based correlation analysis (Cole et al., 2010). To circumvent this seed-selection bias, some studies define the interested network with independent component analysis (Smith et al., 2009). This method firstly performs spatial independent component analysis towards concatenated fMRI data across participants. The timecourses of meaningful components were then regressed on each participant to derive the spatial map of each component on every individual. Though this method is free from the seed-selection bias, the interpretation obtained from this method can be hard since the difference of spatial map in a component does not reveal which connectivity is specifically different (Bijsterbosch et al., 2017). In chapter 3, I applied seed-based correlation analysis to assess the change of interactions between the stimulated and non-stimulated regions.

1.3.2 Several concerns of functional connectivity assessed with resting-state functional magnetic resonance imaging

Here, I overview the general concerns of applying FC calculated by rsfMRI in quantifying the inter-regional brain communications. These concerns are two folded: (1) intra-individual variability is high and (2) BOLD signal does not completely reflect the brain activity on each region.

intra-individual variability is high in FC

The low reproducibility of the results obtained by FC is gaining attention in recent years (Botvinik-Nezer et al., 2020; Eklund et al., 2016; Marek et al., 2022; Rosenberg and Finn, 2022). This failure is partly due to the high intra-individual variability of FC. Marek and colleagues showed that intra-subject correlation of FC was 0.39–0.78 (Marek et al., 2022), whereas that of cortical thickness was more than 0.96 (Kharabian Masouleh et al., 2020).

Several reasons can account for this high intra-individual variability. One reason is that alertness can fluctuate FC. This means that if a participant is sleepy in one session and is alerted in the other, the FC are different between these two sessions. One study investigated the correlations between FC and sleepiness obtained by a questionnaire (Stoffers et al., 2015). They found that the FC when subjects are alerted was higher in visual, sensorimotor, and default mode networks than when subjects are less alerted. This tendency was also observed in the other studies using EEG as the measure of alertness (Haimovici et al., 2017). Although several attempts have been made to exclude these confounds with electrocardiography or EEG (Falahpour et al., 2018; Laumann et al., 2017), it is still difficult to quantify the alertness during the MRI scans both precisely and easily.

Another reason for the high intra-individual variability of FC will be that a subject can have different mental states across different sessions. While subjects can feel itches or thirst in one session, they can have goal-directed mental thoughts, such as a future plan for vacations, in another session (Gonzalez-Castillo et al., 2021). Moreover, one study revealed that the FC can be affected by different mental states (Stoffers et al., 2015). They showed that the FC of visual and sensorimotor network increased when the subjects were more engaged in imagining visual objects, whereas the FC of sensorimotor network alone increased when the subjects felt more comfortable. Taken together, FC can be modulated by several factors other

than the neural communications between two regions, which might compromise the reliability of this measurement.

Blood-oxygen level dependent signal does not always reflect the brain activity on each region

Several studies revealed the discrepancy between the BOLD signal and the brain activity quantified with other methods. Park and colleagues compared the FC of face patches calculated by the rsfMRI and that with single-unit recording, which measures the activity of each neuron (Park et al., 2017). Surprisingly, spatial patterns of FC with single-unit recordings resembled those patterns with rsfMRI in only around 16% of neurons. Moreover, though TMS activates the brain activity of the stimulated region as described in Chapter 1.1, recent systematic review concluded that the brain activity investigated by fMRI failed to observe the neural activation evoked by TMS (Rafiei and Rahnev, 2022). These results imply that the BOLD signals partially reflect the brain activity in each region. Here, I illustrate the several possibilities accounting for these reasons.

One reason for the inability for fMRI to reflect the brain activity can be that the increase of the brain activity does not always increase the BOLD signal (Drew, 2022). Bergel and colleagues compared the electrical neural activity and the blood flow, revealed by a functional ultrasound imaging, when rodents ran freely (Bergel et al., 2020). While the blood flow was increased after the neural activation in hippocampus and thalamus, that in primary motor cortex was decreased. Moreover, Shi and colleagues revealed that the blood flows of caudate and putamen decreased after the neural activation (Shih et al., 2011). Therefore, a BOLD signal does not necessarily reflect the brain activity in its region.

Another reason can be that a GRE sequence is more likely to reflect the signal from the pial vein on the cortical surface than the vein from the deep layers of cerebral cortices (Koopmans et al., 2010; Logothetis, 2003; Logothetis and Wandell, 2004). This is because

the vein on the surface is larger than that in the deep layers of cerebral cortices. Several studies also showed that, by comparing the BOLD signal and electrophysiological activity, BOLD signals preferentially reflect the input signal from other areas and the activity of interneurons, compared to the output signal to the other areas observed mainly in the deep layers of the gray matter (Logothetis, 2008).

All these concerns noted above indicate that the other measurements are required to predict or assess the after-effect of rTMS.

1.4 Neuroimaging methods to probe the microstructural properties of the human brain

Exploring the microstructural property of the human brain is crucial to understand its function. The advantage of this property over the FC described in the previous section is that this is robust to the mental states or alertness during the scans. In this section, I first describe the components of microstructures in the gray and white matter of the brain. Then, I provide a broad overview of noninvasive methods to quantify the microstructural properties. These methods include dMRI, which was applied in this thesis. Lastly, I explain how the several metrics to quantify the microstructural properties of the brain can be calculated from dMRI.

1.4.1 Microstructures in the human brain

The brain can be divided into two major components: the gray and white matter (Kandel et al., 2021). In the cerebral cortex, the gray matter is on the surface of the brain. The main compositions of the gray matter are the cell bodies, dendrites, or axons of both pyramidal neurons and interneurons. Both pyramidal neurons in the surface layer of the gray matter (i.e., layer Ⅱ/Ⅲ) and interneurons are supposed to contribute to the after-effect of rTMS (Di Lazzaro et al., 2010; Hamada et al., 2013; Li et al., 2019; Siebner et al., 2022). In contrast, the main composition of the white matter is the axons connecting neurons in the gray matter, and the cell bodies scarcely prevail in the white matter (García-Marín et al., 2010). Generally, axons are surrounded by myelin, which is important for the fast neuro-transmission and metabotropic support of axons (Micu et al., 2018).

Besides neurites, blood vessels exist in the gray matter and to a lesser extent in the white matter (Doucette et al., 2019). Glial cells are also located both in the gray and white matter. Glial cells include oligodendrocytes, astrocytes, and microglial cells. Oligodendrocytes form myelin, which surrounds axons as described above. The main role of

astrocytes is regulating the concentration of extracellular ions, while that of microglial cells is phagocytosing extracellular debris and regulating neuroimmune systems (Purves, 2017).

1.4.2 Noninvasive methods to reveal the microstructural properties of the human brain

MRI has been applied to noninvasively quantify the microstructural properties as well as the neural activity of each region in the human brain. Here, I illustrate three major MRI-techniques assessing the microstructural properties: MR relaxometry, T1-weighted/T2-weighted ratio, and dMRI. MR relaxometry quantifies the microstructural property more precisely than other two methods (Oishi et al., 2020) but the required scanning time is long. In contrast, the scanning time of T1-weighted/T2-weighted ratio is short, but this method is susceptible to the bias-field. The required scanning time is also short in dMRI and the measurements calculated by this method were shown to be comparable to the histological data (Lazari and Lipp, 2021). Therefore, I utilized dMRI to noninvasively quantify the microstructural property in this thesis.

MR relaxometry

First method is MR relaxometry (Hashemi et al., 2012). This method collects multiple MR images with various parameters to quantify the density of certain components in each voxel, such as lipid, iron, or water. For example, lipid content is sensitive to the longitudinal relaxation time (T1) obtained from the MR signal. The relationship between T1 and MR signal follows the following equation:

$$S(t) = A - B \cdot exp(-t/T1) \qquad (1\text{-}3)$$

Here t is the inversion time, which is one of the parameters in obtaining MRI. The signals acquired from MR images with multiple inversion times are fitted to the equation 1-3 to calculate the precise T1 value in each voxel. Since myelin is rich in lipid content, T1 has been proposed to be the indicator for the density of myelin in the brain. Recent meta analysis also

showed that T1 significantly correlated with the density of myelin revealed by the histological indicators (Lazari and Lipp, 2021).

Myelin water imaging (MWI; (Alonso-Ortiz et al., 2015)) and quantitative MRI (qMRI; (Mezer et al., 2013)) are the major derivatives of MR relaxometry. MWI obtains multiple T2w images, whose signal is sensitive to the water, with variable echo times (TE). These images derive the distributions of three components in each voxel; water trapped by the lipid bilayers of myelin, that in intra or extracellular water, and that in cerebrospinal fluid. The density of myelin can be estimated by the ratio of myelin-related water components divided by the water from all three components. In contrast, qMRI obtains two types of MR images. These two are spoiled gradient echo images with multiple flip angles and spin-echo inversion recovery echo-planar images with multiple inversion times, which were mainly used for the estimation of non-water or myelin content and field-bias correction, respectively. This method not only calculates T1 but also the density of water in each voxel. Moreover, this technique has successfully disentangled the microstructural properties of the subcortical regions (Oishi et al., 2020) and the correlations between these properties and the inter-individual variability of behavior (Gomez et al., 2017; Oishi et al., 2018). However, the problem of MR relaxometry is the relatively long scanning-time (25–45 min).

T1-weighted/T2-weighted ratio

To alleviate the issue of long scanning-time described above, a more simple method called T1-weighted (T1w)/T2-weighted (T2w) ratio was developed (Glasser and Van Essen, 2011). This method obtains only T1w and T2w images to divide the signal of T1w image by that of T2w image. T1w/T2w ratio was shown to capture the region-specific characteristic of the gray matter (Glasser et al., 2016a). However, this method is susceptible to the bias field of the Rf pulse emitted by the transmit coil (Glasser et al., 2021). This has been the major obstacle

in accurately quantifying the structural property of the human brain (Arshad et al., 2017; Uddin et al., 2018a, 2018b).

diffusion MRI

dMRI is another approach to assess the microstructural property with MRI (Basser et al., 1994). This method measures the diffusivity of the water in each voxel with multiple directions. Exploring the restrictions of water-diffusivity in each voxel was supposed to reveal the structural characteristics of several components, such as the diameter of axons and the density of myelin or neural cells (Le Bihan, 2003; Le Bihan et al., 2001). Though this method generally lacks in specificity, the metrics derived from dMRI were significantly correlated with those from MWI (Uddin et al., 2019) and from qMRI (Oishi et al., 2018). Moreover, these measurements have been shown to be correlated to the histological indicators (Lazari and Lipp, 2021) and have successfully revealed structure-function relationships of the human brain (Bullmore and Sporns, 2009; Kanai and Rees, 2011; Thomason and Thompson, 2011). Therefore, dMRI is the simple and promising method to explore the microstructural properties of the human brain.

1.4.3 Metrics derived from diffusion magnetic resonance imaging

Several metrics can be calculated from dMRI data. Diffusion tensor imaging (DTI) is the classical way of quantifying the microstructures with dMRI (Basser et al., 1994). Neurite orientation dispersion and density imaging (NODDI) is the more sophisticated method to investigate the microstructures of the living human brain, assessing the complex microstructures more accurately than DTI (Zhang et al., 2012). Here, I detail these two techniques with several derivatives.

Diffusion tensor imaging

DTI-model is the classical way of modeling the diffusivity of the water in the human brain. It assumes that the diffusivity of the water is distributed following multivariate normal distributions. DTI-model models the signal from dMRI as follows:

$$\frac{S}{S_0} = exp(- bg^T D\, g) \qquad (1\text{-}9)$$

Here, S, S_0, b, and D are the same as the equations 1-4 and 1-8. g denotes the gradient vector of MPG. Applying singular-value decomposition to the diffusion tensor described in equation 1-3, three eigenvectors with three eigenvalues (λ_1, λ_2, and λ_3 [$\lambda_1 \geq \lambda_2 \geq \lambda_3$]) can be obtained. The eigenvector with the highest eigenvalue is supposed to be parallel to the major direction of the axon in a voxel, while the other two eigenvectors to be perpendicular to the axon.

From these three eigenvalues, three major metrics can be calculated; fractional anisotropy (FA), mean diffusivity (MD), and radial diffusivity (RD). These metrics can be defined as follows:

$$FA = \sqrt{\frac{3}{2}} \frac{\sqrt{(\lambda_1 - < D >)^2 + (\lambda_2 - < D >)^2 + (\lambda_3 - < D >)^2}}{\sqrt{\lambda_1^2 + \lambda_2^2 + \lambda_3^2}} \qquad (1\text{-}10)$$

$$MD = < D > \qquad (1\text{-}11)$$

$$RD = \frac{\lambda_2 + \lambda_3}{2} \qquad (1\text{-}12)$$

<D> is the mean of the three eigenvalues. FA and RD are assumed to be the indicators of the myelin content, whereas MD is to be the indicator of cell density in each voxel.

Though DTI is an oversimplified model to quantify the microstructure of the brain (Jeurissen et al., 2013), the advantage of this model is that the required sample sizes are relatively small for the robust estimation (around 30 in b = 1000 datasets) compared to other complex modelings (Johansen-Berg and Behrens, 2013). This means that the required acquisition time is short, and this model is easily applied in clinical practice and in

investigating the microstructural change even when that change is transient and its duration is short.

Several studies revealed the usefulness of DTI in assessing the microstructural property of the human brain. First, the spatial patterns of these metrics in the human brain were shown to be matched with that of histological indicators, including myelin (Lazari and Lipp, 2021), astrocytes (Sagi et al., 2012), and microglial cells (Yi et al., 2020). Second, these measures were reported to be useful in distinguishing the brain of patients with psychiatric diseases from that of controls (Thomason and Thompson, 2011). Third, they also detected the acute phase of structural change in the living human brain induced by behavioral training (Sagi et al., 2012; Sampaio-Baptista et al., 2021; Scholz et al., 2009; Tavor et al., 2020). Taken together, the DTI-model is useful for assessing or detecting the change in the microstructural property of the human brain.

Neurite orientation dispersion and density imaging

Neurite orientation dispersion and density imaging (NODDI) is developed to quantify the dispersion of axons and the distribution of three major components; intra-cellular, extra-cellular, and cerebro-spinal fluid (CSF) compartments (Zhang et al., 2012). This models the signal from dMRI as follows:

$$\frac{S}{S_0} = (1 - f_{iso})(f_{ic}A_{ic} + (1 - f_{ic})A_{ec}) + f_{iso}A_{iso} \qquad (1\text{-}13)$$

Here *f, A, ic, ex,* and *iso* indicate fraction, diffusion signal normalized by the signal without MPG (i.e., S/S_0), intracellular compartment, extracellular compartment, and CSF compartment, respectively. f_{ic} is termed as neurite density index (NDI).

A_{ic} (i.e., normalized signal within the axon) is modeled as follows:

$$A_{ic} = \int exp(-bd(g \cdot n)^2) \cdot f(n)dn \qquad (1\text{-}14)$$

Here *d* denotes the intrinsic diffusivity of the water in the human brain, while *n* and *f(n)* indicate the orientation of the fiber and its distribution function in a voxel, respectively. The equation 1-14 assumes that the diffusivity of the water within an axon as a cylinder, which means the movement of the water parallel to the axon is unrestricted whereas the movement perpendicular to the axons is strictly restricted (i.e., no movement). The orientation of the fiber in each voxel is assumed to follow a Watson distribution with concentration parameter κ , and κ is used to for orientation dispersion index (ODI) denoted as below:

$$ODI = \frac{2}{\pi} arctan(\frac{1}{\kappa}) \qquad (1\text{-}15)$$

In contrast, A_{ec}(i.e., normalized signal outside the axon and CSF) is modeled as follows:

$$A_{ec} = exp(- bg^{T}(\int D(n) \cdot f(n)dn)g) \qquad (1\text{-}16)$$

Here D(n) is the diffusion tensor. This tensor models the diffusivity of the water as an ellipsoid (same as the DTI-model), whose principal direction is *n*. The diffusivity of the water in the direction parallel to *n* is unrestricted, while the diffusivity of the water perpendicular to *n* is restricted as the fraction of axons (i.e., f_{ic}) increases (Szafer et al., 1995). A_{iso} (i.e., normalized signal within CSF) is modeled such that the diffusivity of the water is unrestricted in all directions. Though the NODDI model is a still oversimplified model to capture the microstructures in the human brain (Lampinen et al., 2017), NDI and ODI were respectively correlated to each metric calculated by histological indices (Grussu et al., 2017). Therefore, this model at least represents the density and dispersion of neurites in each voxel.

There are other models assuming several compartments in a voxel: Free water imaging (Hoy et al., 2014), Ball and stick model (Jbabdi et al., 2012), and Composite hindered and restricted model of diffusion (CHARMED, (Assaf and Basser, 2005)). These models are more or less simple versions of the NODDI-model. Free water imaging assumes

that the axons in a voxel are oriented in one direction as in the DTI-model, but assumes that each voxel has two compartments: cellular and CSF compartments. Ball and stick model also assumes the two compartments as in Free water imaging, but assumes more number of orientations of axons in one voxel (typically 2–3 orientations (Sotiropoulos et al., 2013)). In contrast, CHARMED assumes that the diffusivity of the water is composed of the diffusivity of the water within and outside of the axons.

In this study, I mainly applied the DTI-model, and, to clarify the microstructural bases of DTI-derived metrics, I further utilized the NODDI-model in Chapter 2.

Chapter 2. Microstructural properties of the human brain can predict the after-effect of intermittent theta burst stimulation

This chapter is adapted from "Microstructural Properties of the Human Brain Revealed by Fractional Anisotropy Can Predict the After-effect of Intermittent Theta Burst Stimulation." Cerebral Cortex Communications, 3 (1), 1-12, 2022, Ikko Kimura, Hiroki Oishi, Masamichi J. Hayashi, Kaoru Amano.

2.1 Introduction

rTMS is widely used to modulate cortical excitability for experimental investigations and for the treatment of neurological or psychiatric diseases such as major depression, movement disorders and chronic pain (Lefaucheur et al., 2020). Thus, it is of great experimental and clinical value to predict those participants or patients most responsive prior to application. Intermittent theta burst stimulation (iTBS) is a rTMS protocol consisting of three pulses at 50 Hz repeated at 200-ms intervals (5 Hz) and delivered intermittently for 191 s (600 pulses in total) (Huang et al., 2005). This protocol was FDA-approved for treating treatment-resistant depression (Chen et al., 2021), and has now been currently the focus of preclinical (Rounis and Huang, 2020) and clinical trials (Blumberger et al., 2018; Chen et al., 2021; Cole et al., 2022; Li et al., 2018, 2014). This is because this pattern can enhance the brain activity of the stimulated region longer than the conventional rTMS protocols (e.g., 5 or 10 Hz rTMS). Specifically, iTBS over the primary motor cortex (M1) can evoke a long-term potentiation (LTP)-like after-effect in corticospinal excitability for around 30 min (Corp et al., 2020; Huang et al., 2005)), while the conventional facilitatory rTMS protocols can induce such an effect for around a few minutes (Oberman, 2014).

A major concern when using iTBS, however, is the substantial inter-individual variability in the magnitude of the after-effect (Corp et al., 2020; Hamada et al., 2013; Hinder et al., 2014; Leodori et al., 2021; López-Alonso et al., 2014; Ozdemir et al., 2021). Thus, prior assessment of iTBS susceptibility would be useful for obtaining robust results in rTMS experiments (López-Alonso et al., 2014) and for identifying patients most likely to benefit from clinical application. Previous studies have found that age, genetic polymorphisms, time of the day iTBS is delivered and hormone levels are associated with inter-individual variability in the after-effect (for review, see (Suppa et al., 2016), and for the result from the meta-analysis, see (Corp et al., 2020)). However, these factors are not region specific, and underlying neuro-modulatory mechanisms critical for the iTBS after-effect are unknown.

Recently, Nettekoven and colleagues reported that the functional connectivity (FC) values between M1 and other cortical regions predicted the magnitude of the iTBS after-effect (Nettekoven et al., 2015). This result suggests that the strengths of neural connections with iTBS targets may also influence the inter-individual variability. However, given that FC fluctuates depending on the subject's state of mind and alertness (Rosenberg et al., 2016), anatomical connectivity, which is independent of these factors, may be a more robust predictor. Fractional anisotropy (FA), a metric of diffusion magnetic resonance imaging (dMRI) that quantifies the anisotropy in directionality of water diffusion, is associated with the microstructural properties of neural tissue such as cell density and the orientation, diameter and myelination of axons (Beaulieu, 2002; Le Bihan, 2003; Le Bihan et al., 2001). Furthermore, several studies have found that FA values can predict the ability to learn new motor skills (Lehmann et al., 2019; Schulz et al., 2015; Tomassini et al., 2011), recovery rate of motor function after stroke (Kumar et al., 2016; Puig et al., 2017; Soulard et al., 2020) and degree of behavioral change induced by rTMS (Vanbellingen et al., 2020), suggesting that FA is associated with synaptic plasticity within motor-associated regions.

I speculated that the microstructural properties reflected by dMRI are associated with inter-individual differences in the after-effect of iTBS. To test this hypothesis, I examined whether regional FA values within the human brain, which reflect local microstructural properties of white and gray matter, are correlated with inter-individual variability in the iTBS after-effect over M1. I report that FA values in certain white and gray matter regions predict the magnitude of the after-effect during the early and late phases, respectively, while other factors, such as sex and age, had little influence. These findings suggest that metrics derived from dMRI measurement, such as FA, are strong predictive indicators of regional responses to iTBS and possibly to other rTMS protocols.

2.2 Materials and Methods

The experiment required two days for completion by each participant. On day 1, MRI data were collected. On day 2, the after-effect of iTBS was assessed by measuring the amplitude of motor evoked potentials (MEPs) pre- (baseline) and post-iTBS (Figure 2.1a).

2.2.1 Participants

Eighteen healthy adult volunteers (13 males and 5 females; age 20–24 years; mean ± standard deviations (SD), 21.7 ± 1.0 years) participated in this study. All subjects were right-handed according to the Edinburgh handedness inventory (Oldfield, 1971) and reported no history of neuropsychiatric diseases. The experiments were approved by the institutional ethics and safety committees of the National Institute of Information and Communications Technology and were performed in accordance with the Declaration of Helsinki. All participants provided informed consent after a full explanation of study protocols and aims.

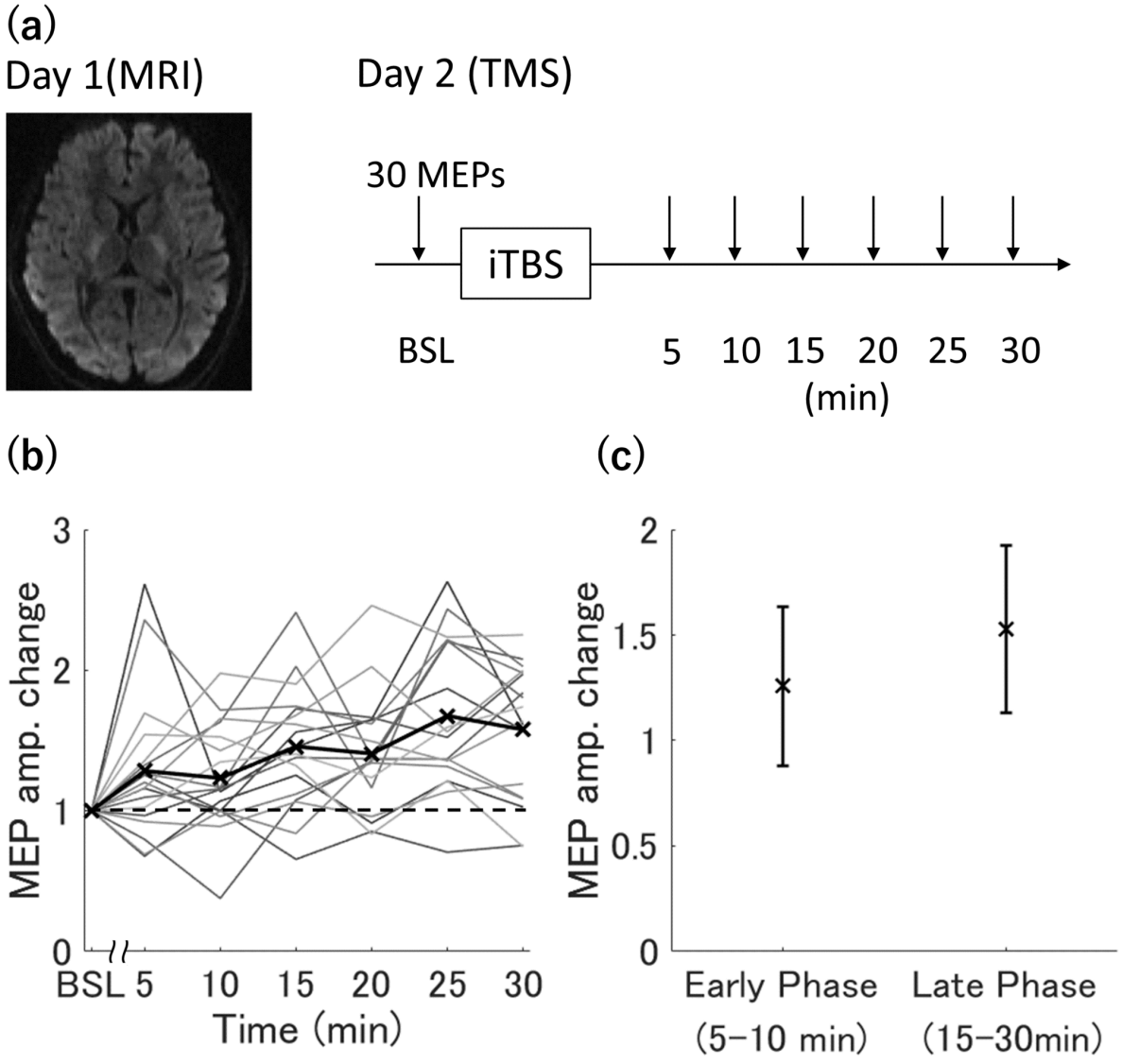

Figure 2.1 Overview of the experimental protocol for measuring changes in the MEP amplitude after iTBS over the primary motor cortex. (a) On day 1, MRI data were acquired. On day 2, a TMS experiment was performed in which MEPs were measured before and after iTBS. (b) Individual time courses of MEP amplitude changes for all participants (n = 18). The horizontal axis indicates the time after iTBS, while the vertical axis indicates the MEP amplitude normalized to baseline amplitude (BSL). Thick black line and cross indicate the mean change in MEP amplitude across individuals. (c) Changes in MEP amplitude during the early phase (5–10 min post-iTBS) and late phase (15–30 min post-iTBS). The black cross indicates the mean change and error bars indicate ±1 SD.

2.2.2 Transcranial Magnetic Stimulation

The iTBS was applied over the right M1 to target the left first dorsal interosseous (FDI) muscle. I note that the after-effect of iTBS showed no significant difference when TBS was applied over M1 of the dominant versus non-dominant hemisphere (Suppa et al., 2008). Each session was performed in the afternoon, starting around 1 pm or 3 pm, to mitigate known diurnal variations in response (Suppa et al., 2016). To determine the optimal stimulator output for MEP measurement and iTBS, resting motor threshold (RMT) and active motor threshold (AMT) were defined for each participant prior to the iTBS session using the relative-frequency method (Rossini et al., 2015). The MTs defined by this conventional method were nearly the same as those defined by the recently proposed adaptive-threshold hunting method (Ah Sen et al., 2017). The RMT was defined as the lowest intensity that evoked a MEP of at least 50 mV on 5 out of 10 trials in the left FDI muscle at rest (Rossini et al., 2015), while AMT was defined as the lowest intensity that evoked a MEP of at least 200 mV on 5 out of 10 trials in the left FDI muscle during volitional contraction at ~10% of maximum (Rossini et al., 2015). Thirty MEPs from the left FDI muscle were recorded ~10 min before iTBS (baseline) and for up to 60 min after iTBS at 5-min intervals, with the stimulator output set to 120% of the RMT. The stimulation was targeted to the hotspot over M1 evoking the strongest MEP in the left FDI muscle. Coil orientation was also optimized to elicit the largest MEPs, with the coil handle pointing backward and ~45° from the midline. Before iTBS, alertness of the participants was also assessed by the Stanford Sleepiness Scale (SSS) (Hoddes, 1972). All MEPs for determination of RMT and the iTBS after-effect were evoked using a monophasic Magstim 200^2 stimulator (Magstim, Whitland, UK) with a figure-of-eight 70-mm standard coil, while AMT was determined using a biphasic Magstim Rapid^2 stimulator (Magstim, Whitland, UK) with a figure-of-eight 70-mm air film coil.

The iTBS was delivered with the same stimulator and coil as used for AMT measurements. The stimulation was targeted to the hotspot over the M1 evoking the strongest MEP in the left FDI muscle. The iTBS protocol was the same as that introduced by Huang et al. (Huang et al., 2005), consisting of 2-s trains of three pulses at 50 Hz repeated every 200 ms (5 Hz). Trains were repeated 20 times at an 8-s inter-train interval for 191 s (a total 600 pulses). The stimulation intensity was basically set to 80% of the AMT. However, when 80% AMT exceeded the system's upper limit for TBS protocols (corresponding to 50% maximum stimulator output [MSO]), the stimulator output was set at this upper limit. The coil position and orientation during iTBS remained the same as the ones optimized for RMT measurements, following Huang's original paper (Huang et al., 2005). The coil position was monitored and recorded using a Brainsight neuronavigation system (Rogue Research Inc, Montreal, Canada), and the mean deviation of coil position from the mean stimulated location across trials was calculated for each participant.

2.2.3 Electromyography

MEPs from the left FDI muscle were recorded as surface electromyogram (EMG) signals using pre-gelled Ag-AgCl electrodes, with the active electrode placed on the muscle belly and the reference electrode on the metacarpophalangeal joint of the left index finger. The MEP signals were amplified and recorded with 16 Hz to 470 Hz band-pass filtering and 3 kHz digitisation using Brainsight (Rogue Research Inc, Montreal, Canada).

2.2.4 Motor Evoked Potential Analysis

MEP amplitudes were measured using custom software and the Veta-Toolbox (Jackson and Greenhouse, 2019) implemented in Matlab (MathWorks, Natick, Massachusetts). For three participants, I was unable to measure MEPs 35 min post-iTBS due to coil overheating and hence only the time points up to 30 min post-iTBS were used for subsequent analysis. At

each time point, MEPs larger than 2.5 SDs from the mean of 30 trials were rejected as outliers (Fried et al., 2017) and the remaining MEP amplitudes were averaged and divided by the mean baseline MEP amplitude to calculate the after-effect of iTBS. Since previous studies have reported bimodal changes in MEP amplitude after iTBS, with a trough at 12.5 min post-iTBS (Huang et al., 2005), I separated the time points into two phases, early (5 and 10 min post-iTBS) and late (15–30 min post-iTBS), and the change in amplitude at each time point within each phase relative to baseline was averaged. To validate this phase stratification, I performed hierarchical clustering analysis. First, similarity measures were calculated between each time point as the Euclidean distance between vectors of MEP amplitude for all participants and then clustering analysis was conducted using the single linkage method (Murtagh and Contreras, 2012). I also performed a two-tailed one-sample Student's t-test for the MEP amplitude changes in the early and late phases. In each phase, I confirmed that the MEP amplitude change was not affected by the outlier rejection method. In particular, the MEP amplitude changes were highly correlated between outlier rejection by raw data (0.018% rejected) and log-transformed data (0.015% rejected) (Early phase, rho = 0.99, $P < 0.001$; Late Phase, rho = 0.99, $P < 0.001$)).

2.2.5 Image acquisition

Prior to the iTBS session, diffusion-weighted MRI (dMRI) data with b = 1000 s/mm^2 and b = 2000 s/mm^2 were collected from each participant using a Siemens Vida 3T scanner and 64-channel array head-neck coil (Siemens, Erlangen, Germany). Both diffusion-weighted images were obtained using a multislice 2D single-shot spin-echo echo-planar sequence with the following parameters: voxel size = 2 × 2 × 2 mm, matrix size = 106 × 106 × 75, iPAT reduction factor = 2, Multiband Acceleration Factor = 3, phase-encoding direction = A-P, and TR = 5300 ms. The number of directions and TE differed between the two datasets, with number of directions = 30 and TE = 71 ms for the b = 1000 s/mm^2 dataset and number of

directions = 60 and TE = 86 ms for the b = 2000 s/mm^2 dataset. Eight non-diffusion-weighted (b = 0 s/mm^2) images were also acquired to minimize EPI distortion, five images with the same TE as in the b = 1000 s/mm^2 dataset with three images reversed phase-encoding directions (i.e., P-A), and three images with the same TE and phase-encoding directions (i.e., A-P) as in the b = 2000 s/mm^2 dataset. Total acquisition time for dMRI was around 10 min for each participant.

For neuronavigation of TMS coil position and surface-based analysis, a T1-weighted MP-RAGE image was also obtained for each participant (voxel size = 1 × 1 × 1 mm, TE = 2.48 ms, TR = 1900 ms, flip angle = 9°).

2.2.6 Image analysis

The dMRI data were preprocessed using tools from the FMRIB software library (FSL 6.0.1, https://fsl.fmrib.ox.ac.uk/fsl). The FSL topup tool was used to correct for EPI distortions due to inhomogeneity in the magnetic field (Andersson et al., 2003) and the eddy tool was used to correct for eddy current (Andersson and Sotiropoulos, 2016) with outlier replacement and slice-volume correction (Andersson et al., 2016). Non-brain tissue was removed using Brain Extraction Tool (Smith, 2002). FA was calculated for each b = 1000 s/mm^2 and b = 2000 s/mm^2 dataset using the DTIFIT application of FSL, and averaged across individual datasets to obtain individual FA maps.

To determine whether the difference in FA reflects the density and/or dispersion of orientation of neurites (Zhang et al., 2012), neurite density index (NDI) and orientation dispersion index (ODI) were calculated using the NODDI toolbox v1.0.3 (www.nitrc.org/projects/noddi_toolbox). NODDI considers the neurite compartment as a set of sticks, which restrict the diffusivity of water along their perpendicular direction. The density of neuritic compartments was defined as NDI, while the orientation dispersion of the

neurites was defined as ODI. Because dendrites and axons are mainly located in the gray and white matter, respectively, the NDI/ODI in gray and white matters were considered to provide microstructural indices for dendrites and axons, respectively (Zhang et al., 2012). Before fitting the NODDI model, diffusion-weighted images at each b value were divided by the mean non-diffusion-weighted image obtained with the same TE value to merge each dataset (Chang et al., 2015; Owen et al., 2014; Palacios et al., 2020). The fitting was performed using the default settings for white matter (WM), while the intrinsic free diffusivity parameter was changed to 1.1×10^{-3} mm^2/s for gray matter (GM) (Fukutomi et al., 2019, 2018; Guerrero et al., 2019).

The Tract-Based Spatial Statistics (TBSS) tool of FSL (Smith et al., 2006) was used for whole-brain voxel-wise analysis of WM. First, the FA map for each participant was non-linearly registered to $1\times1\times1$ mm^3 MNI152 space (McConnell Brain Imaging Centre, Montreal Neurological Institute). From the mean FA image across participants, a common skeleton was extracted to represent the main WM structure. This skeleton was thresholded at FA > 0.2 (Default) and FA data warped to the MNI standard space were then projected onto this skeleton. The NDI and ODI were also projected onto the skeleton using the same warp used for FA.

For surfaced-based analysis, FreeSurfer (Version 6.0.0, https://surfer.nmr.mgh.harvard.edu/) was used to obtain individual cortical surfaces (Fischl et al. 1999). After removing non-brain tissues, the structural brain image was normalized into Talairach space and the intensity of each image was normalized. The normalized brain image was then segmented into GM, WM and cerebrospinal fluid (CSF). The GM–WM boundary (WM surface) and GM–CSF boundary (pial surface) were used for surface reconstruction. Utilizing the folding pattern, the surface was registered to the standard surface space (fsaverage). All dMRI-derived GM metrics were sampled from the mid-points of white and

pial surfaces as the partial-volume effect is less likely to impact the results (McNab et al., 2013). The sampled data was warped to fsaverage space, and smoothed with a Gaussian Kernel of 10-mm FWHM across the cortical surface according to a previous study using FA for surface-based analysis (Stock et al., 2020).

2.2.7 Statistical analysis

The FSL "randomise" tool was used to test the statistical significance of associations between each phase of MEP amplitude change and the TBSS data. For the surface-based analysis, the FSL Permutation Analysis of Linear Models tool was used to test these associations in GM. In both WM and GM, I performed 5000 permutation tests and employed Threshold-Free Cluster Enhancement to control for multiple testing (Smith and Nichols, 2009). To specify locations significantly correlated with MEP amplitude change, significantly associated WM and GM voxel clusters were labeled using the Johns Hopkins University white-mater tractography atlas (https://fsl.fmrib.ox.ac.uk/fsl/fslwiki/Atlases) and Desikan-Killiany atlas (Desikan et al., 2006), respectively. To distinguish the microstructural properties contributing to inter-individual variability in FA, I calculated Pearson's correlation coefficients between mean FA and mean NDI or ODI in each cluster and tested the significance by 5000 permutation tests. In all analyses, Bonferroni correction was used to adjust for possible spurious findings due to multiple testing.

I also calculated Pearson's correlation coefficients between all measured continuous variables and MEP amplitude change within each phase, while two-tailed unpaired t-tests were performed to assess how MEP amplitude change is affected by sex and iTBS intensity (80% of AMT or 50% of MSO). A $P < 0.05$ was considered significant for all tests. These analyses were performed using JASP (ver. 0.13.1 for Windows, https://jasp-stats.org/).

2.3 Results

All participants completed both MRI scans and iTBS experiments, and no adverse events occurred during these procedures. The mean deviation of the stimulated location from the mean stimulated location across trials was 0.85 mm (range: 0.33–1.64 mm) (See Figure 2.2 for the error bar of the trial-by-trial deviation for each participant). Plotting the individual time courses of MEP amplitude changes post-iTBS relative to baseline revealed substantial inter-individual variation (Figure 2.1b), in accord with previous reports (Hamada et al., 2013; López-Alonso et al., 2014). Consistent with the previous study showing the two phases of MEP amplitude change after iTBS (Huang et al., 2005), the hierarchical clustering analysis revealed the similar separation in the time course (early phase; 5 and 10 min post-iTBS, late phase; 15–30 min post-iTBS) (Figure 2.3). Therefore, the relationships between the MEP amplitude change and brain microstructural properties were analyzed separately for the early and late phases. MEP amplitudes post-iTBS were significantly facilitated in both phases (early phase, $t = 2.89$, $P = 0.020$; late phase, $t = 5.68$, $P < 0.001$).

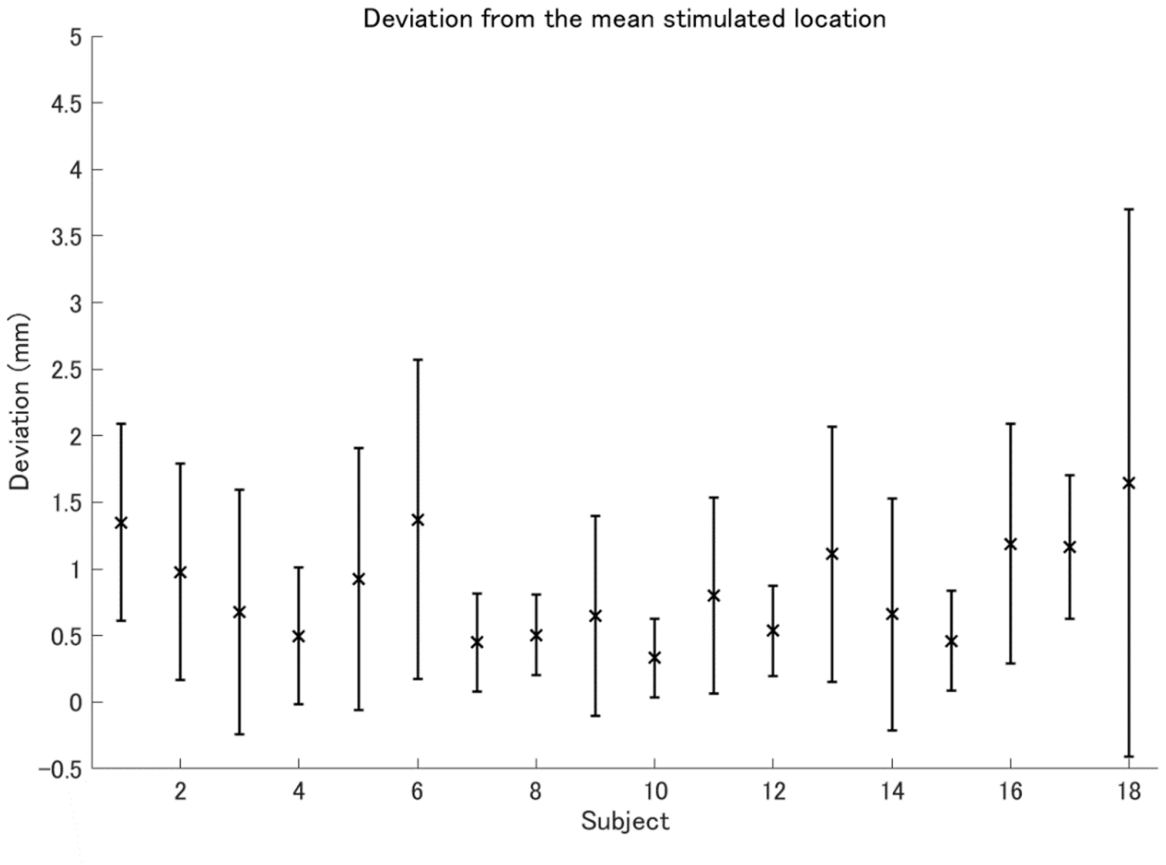

Figure 2.2 Trial-by-trial deviation of the coil position from the mean stimulated location in each iTBS session. The horizontal axis indicates the subject number, while the vertical axis indicates the deviation of the coil position from the mean stimulated location in each session. The black cross indicates the mean and the error bar indicates ±1 standard deviation (S.D.).

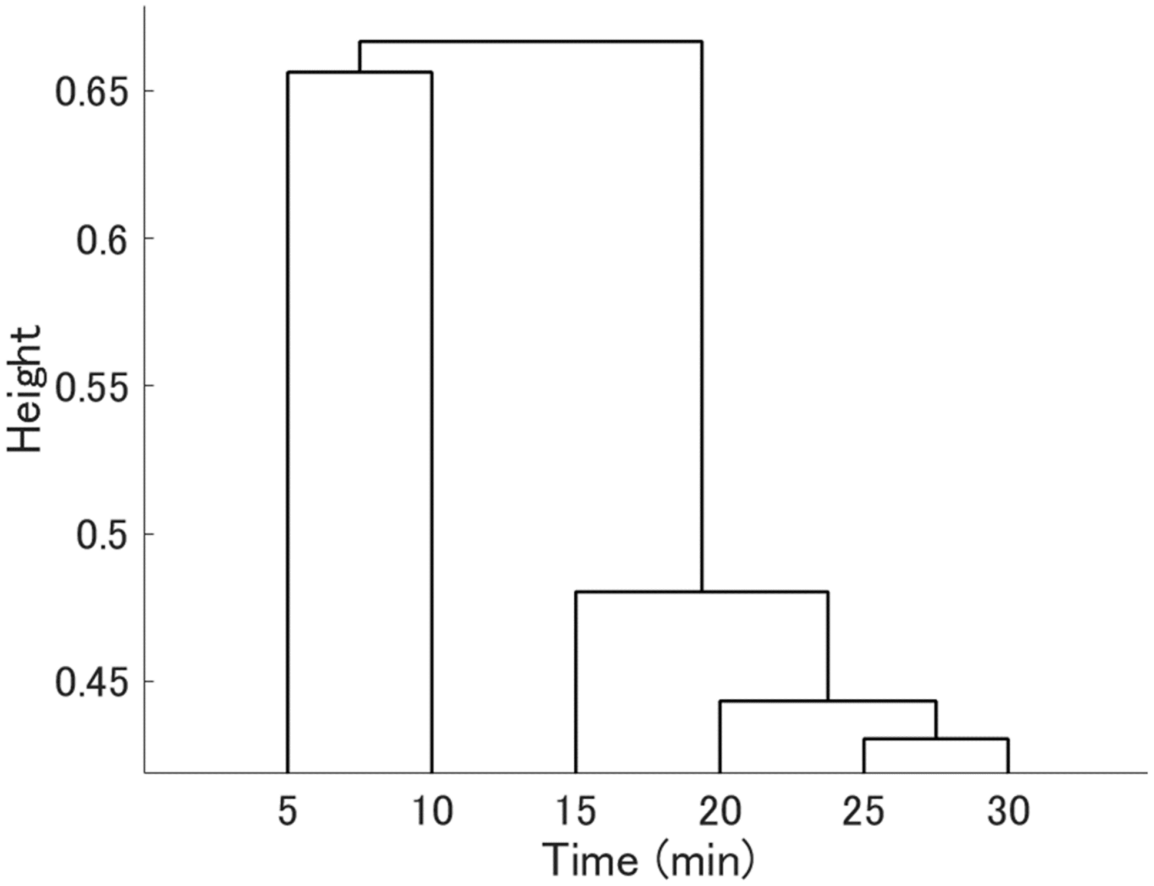

Figure 2.3 Dendrogram of hierarchical clustering across the time course of motor evoked potential (MEP) amplitude change confirming distinct early and late phases. The vertical axis indicates the time after iTBS and the horizontal axis indicates the Euclidean distance.

I first tested the associations between regional FA and MEP amplitude change. During the early phase, MEP amplitude change was significantly and negatively correlated with FA of WM tracts anatomically connected to M1 (Figure 2.4a; for the spatial maps in all slices, see Figure 2.5), including right superior longitudinal fasciculus, right posterior corona radiata, right internal capsule and right corticospinal tract. This voxel cluster is defined as WM 1 and other significant clusters as WM 2–10 in Figure 2.4a. There were also significant negative correlations between MEP amplitude change and FA in bilateral corpus callosum (WM 2 and 3), right forceps minor (WM 4 and 5), left anterior limb of the internal capsule (WM 6), left retrolenticular part of the internal capsule (WM 7), left posterior limb of the

internal capsule (WM 8) and right uncinate fasciculus (WM 9 and 10). Conversely, regional FA in the GM was not correlated with the early-phase MEP amplitude change.

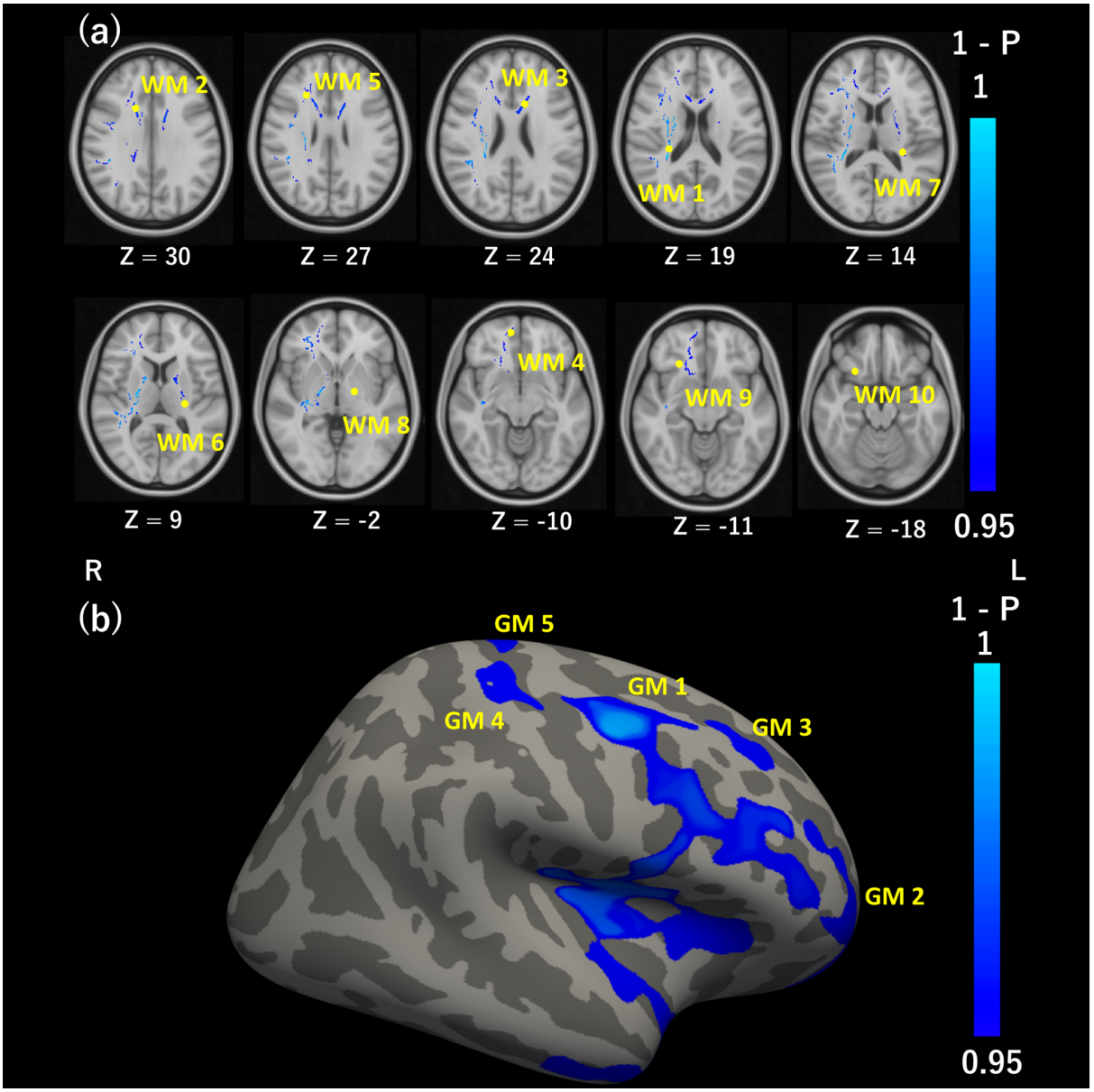

Figure 2.4 Correlations between regional FA and MEP amplitude changes during early and late phases. (a) TBSS analysis of significant correlations between FA in WM and early-phase MEP amplitude change. Clusters in blue represent voxels showing significant negative correlations with FA. The numbers (WM 1–10) correspond to individual voxel clusters. Yellow dots indicate the lowest T-values (strongest correlations) in each cluster. The axial slices are displayed according to radiological convention (left on the picture is right in the brain) with the range in MNI coordinates from z = 30 (top left) to z = −18 (bottom right). (b) Surface-based analysis of significant correlations between FA in GM and late-phase MEP amplitude change. Clusters in blue represent voxels showing significant negative correlations with FA. The numbers (GM 1–5) correspond to the individual voxel clusters.

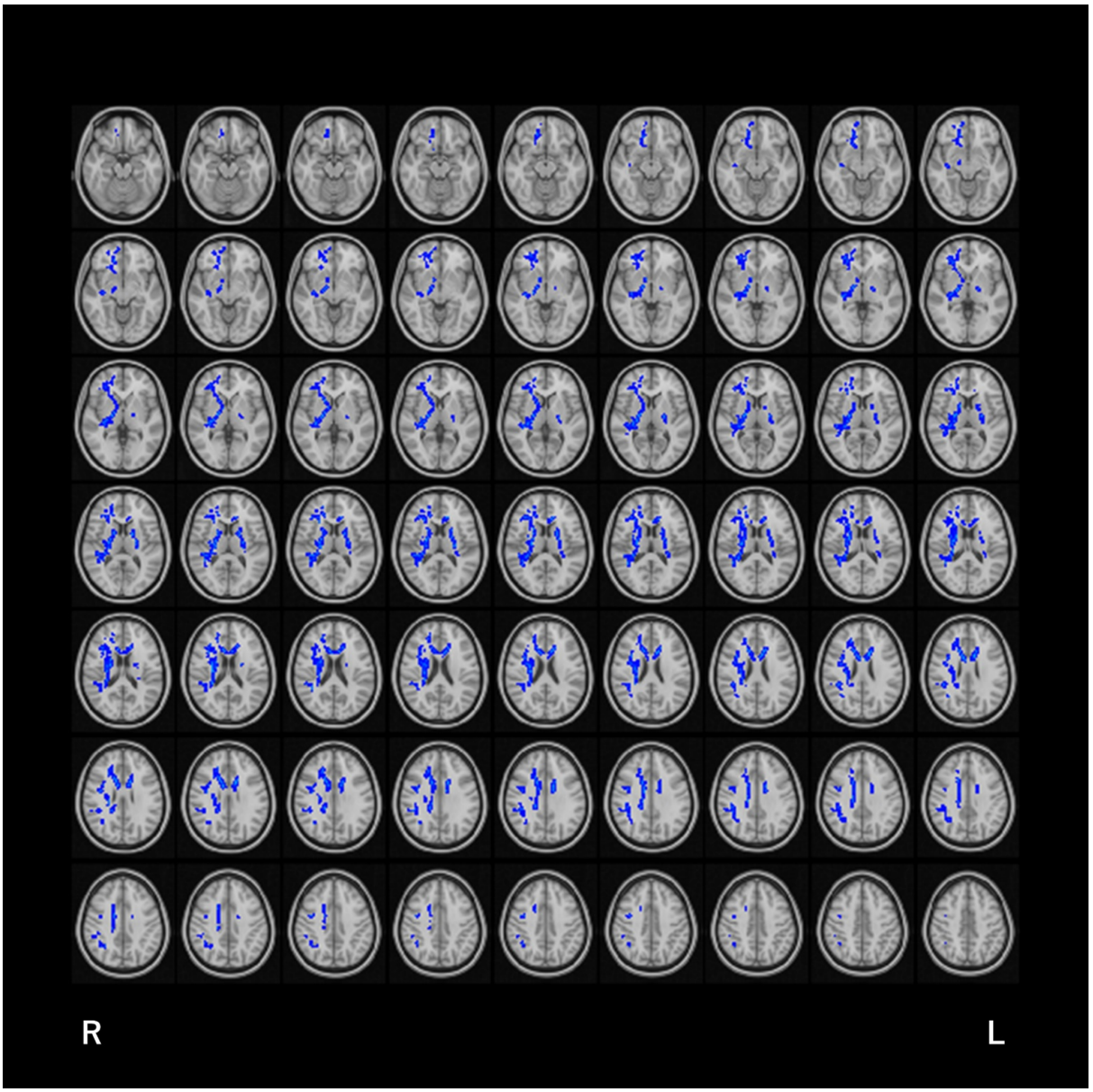

Figure 2.5 Spatial map of correlations between fractional anisotropy (FA) and early-phase motor evoked potential (MEP) amplitude change in all slices (z = −18 – 44) rendered on the standard MNI template. Blue voxels represent regions in which FA was negatively correlated with early-phase MEP amplitude change. The significant voxels are filled using the FSL tbss_fill application to aid visualization.

In contrast to the early phase of MEP amplitude change, the late-phase change was negatively correlated with FA exclusively in GM regions (Figure 2.4b), including the right caudal middle frontal region, right pars opercularis, right insula, right superior temporal and right middle temporal regions (GM 1). Negative correlations were also found between late-phase MEP amplitude change and FA in the anterior part of the right rostral middle

frontal region (GM 2), dorsal part of the right rostral middle frontal region (GM 3), right postcentral gyrus (GM 4) and right precentral and postcentral gyrus (GM 5). There were no significant correlations between the late-phase MEP amplitude change and FA in the WM.

I also tested whether inter-individual differences in MEP amplitude change during the early and late phases were associated with other collected measurements (Table 1). Age, handedness, and interval between the MRI scan and iTBS session were not significantly correlated with either early- or late-phase MEP amplitude change ($P > 0.05$). Similarly, stimulus intensity for MEP induction, iTBS intensity, Stanford Sleepiness Scale score, mean baseline MEP amplitude and mean deviation of stimulated locations from the mean stimulated location across trials were not significantly correlated with the MEP amplitude change ($P > 0.05$). Unpaired t-test also revealed no significant differences in MEP amplitude change between sexes (early phase, $t = 0.77$, $P = 0.45$; late phase, $t = 0.26$, $P = 0.80$) or between subjects receiving iTBS at 80% of AMT or 50% of MSO (early phase, $t = 1.27$, $P = 0.33$; late phase, $t = -0.23$, $P = 0.82$).

Finally, to identify the factors contributing to FA values in each voxel cluster associated with MEP amplitude change, I investigated the correlations between mean FA and mean NDI or ODI, which respectively reflect neurite density or the dispersion of the orientation of neurite within a voxel (Zhang et al., 2012). The FA was positively correlated with NDI in WM 1 (right superior longitudinal fasciculus and right corticospinal tract), WM 4 and 5 (right forceps minor) and WM 6 (left anterior limb of internal capsule) (Figure 2.6a), while FA was negatively correlated with ODI in all WM clusters (Figure 2.6b). The FA values of GM 1–3 (right frontal regions, right insula and right temporal regions) were also negatively correlated with ODI (Figure 2.7a), while FA values of GM 4–5 (the right postcentral gyrus) were positively correlated with NDI (Figure 2.7b).

Table 1.

Correlation between MEP amplitude changes and other measured factors

Factors	MEP change (Early Phase)		MEP change (Late Phase)	
	ρ	*P*	ρ	*P*
Age	-0.10	0.68	-0.00	1.00
Handedness	0.28	0.27	0.23	0.37
Visit Interval	0.07	0.79	-0.13	0.60
RMT	-0.31	0.21	-0.09	0.72
Intensity MEP	-0.22	0.39	-0.10	0.71
Intensity iTBS	-0.46	0.06	-0.22	0.38
SSS	0.06	0.80	-0.16	0.52
Amplitude (baseline)	-0.07	0.78	-0.35	0.16

Note: MEP, motor evoked potential; RMT, resting motor threshold; MEP stimulus intensity, stimulus intensity to induce MEP; iTBS intensity, stimulus intensity to perform intermittent theta burst stimulation; SSS, stanford sleepiness scale; Baseline MEP amplitude, mean size of MEP amplitude before iTBS (baseline).

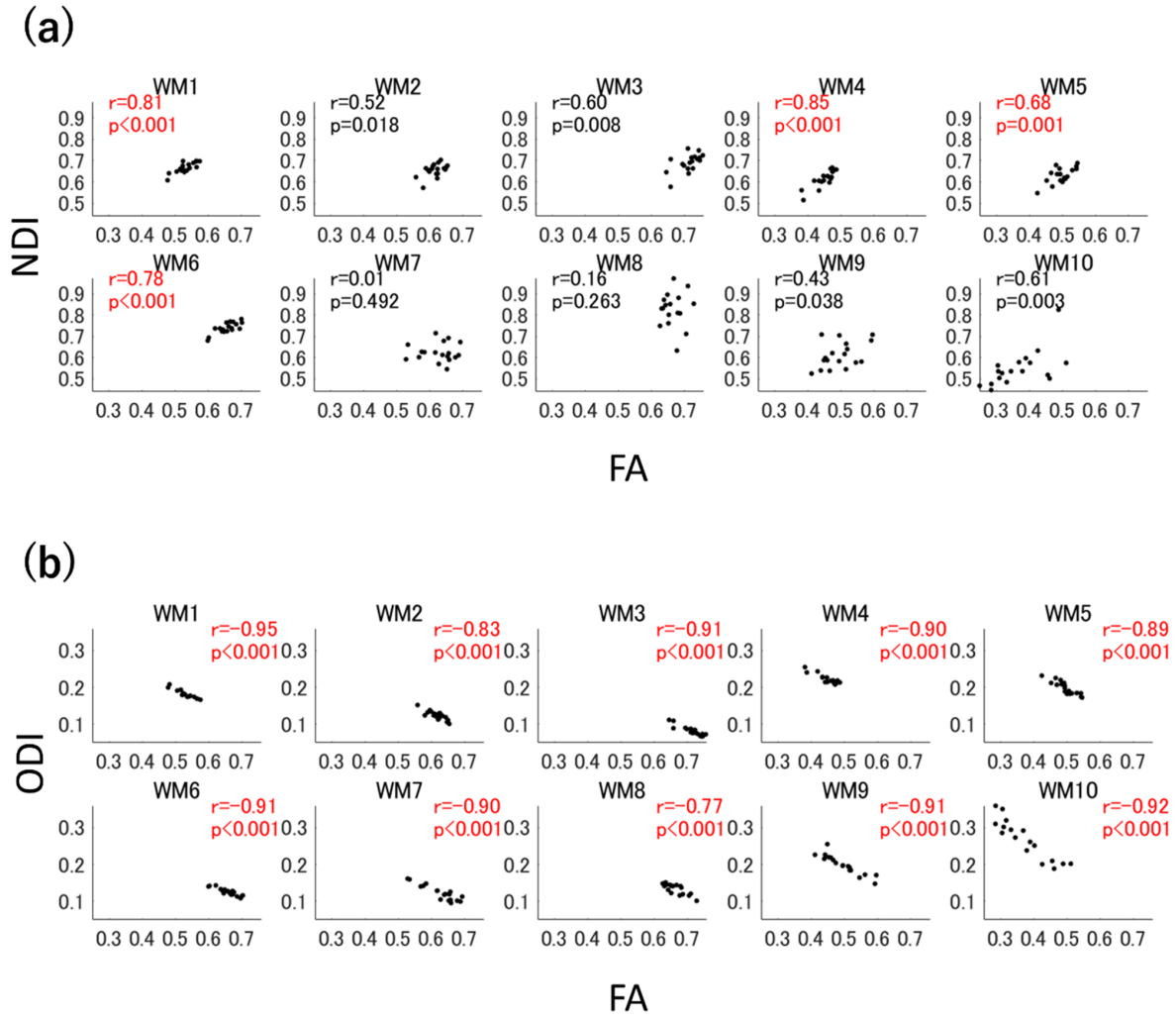

Figure 2.6 (a) Scatter plots of the mean neural density index (NDI) versus the mean fractional anisotropy (FA) in each cluster showing significant negative correlations with early-phase motor evoked potential (MEP) amplitude change. Cluster numbers (WM 1–10) correspond to the labels assigned in Figure 1. The horizontal axis shows the mean NDI in each cluster, while the vertical axis shows the mean FA in each cluster. (b) Scatter plots of mean orientation dispersion index (ODI) versus mean FA in each cluster showing significant negative correlations with early-phase MEP amplitude change. The horizontal axis shows the mean ODI in each cluster, while the vertical axis shows the mean FA in each cluster. The text in red indicates that Pearson's correlation coefficient was significant after Bonferroni correction (i.e., $P < 0.05/20 = 0.0025$).

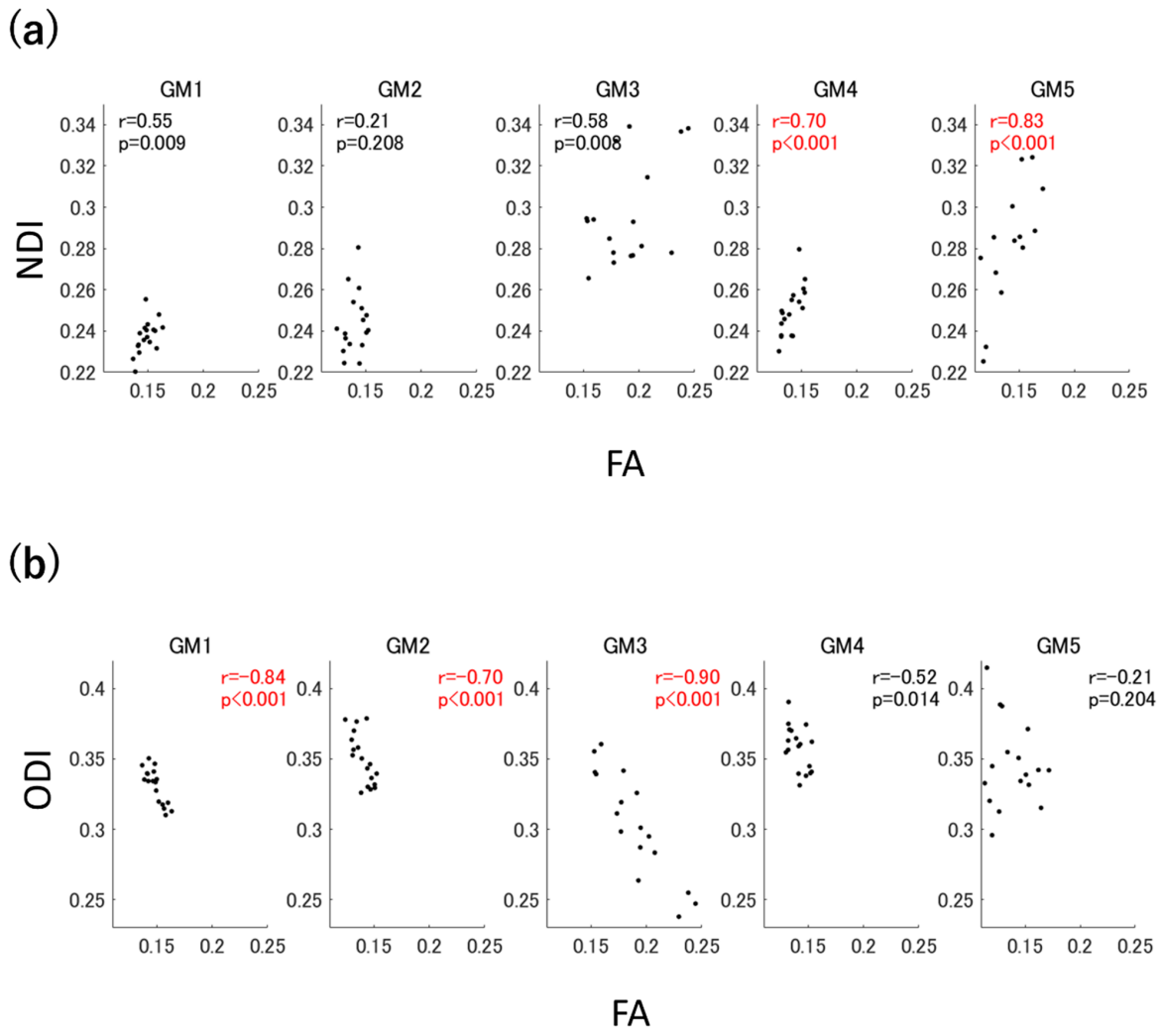

Figure 2.7 (a) Scatter plots of the mean neural density index (NDI) versus the mean fractional anisotropy (FA) in each cluster showing significant negative correlations with early-phase motor evoked potential (MEP) amplitude change. Cluster numbers (WM 1–10) correspond to the labels assigned in Figure 1. The horizontal axis shows the mean NDI in each cluster, while the vertical axis shows the mean FA in each cluster. (b) Scatter plots of mean orientation dispersion index (ODI) versus mean FA in each cluster showing significant negative correlations with early-phase MEP amplitude change. The horizontal axis shows the mean ODI in each cluster, while the vertical axis shows the mean FA in each cluster. The text in red indicates that Pearson's correlation coefficient was significant after Bonferroni correction (i.e., $P < 0.05/20 = 0.0025$).

2.4 Discussion

In this study, I demonstrated multiple significant associations between MEP amplitude change after iTBS over M1 (the iTBS-induced after-effect) and the microstructural properties of GM and WM regions associated with M1. No other measured factors showed significant associations. Thus, individual variation in these microstructural properties can explain, at least in part, the known individual variation in iTBS after-effect, thereby providing a potential method to predict responsive individuals prior to neuroscientific investigations and possibly iTBS-based therapy.

The early-phase MEP amplitude change was negatively correlated with regional FA values in WM tracts including right superior longitudinal fasciculus, corpus callosum, right forceps minor, left internal capsule and right uncinate fasciculus. In contrast, the late-phase MEP amplitude change was negatively correlated with regional FA in GM areas such as right frontal cortex, right insula, right temporal cortex and right postcentral gyrus. Collectively, these findings might suggest that distinct mechanisms underlie the early and late phases of the iTBS after-effect.

2.4.1 Significant increase in MEP amplitude post-iTBS

I noted a significant and continuous increase in the MEP amplitude until 25 min post-iTBS. In contrast, Hamada and colleagues reported no significant facilitation in the MEP amplitude after iTBS (Hamada et al., 2013). A recent meta-analysis investigating the after-effect of iTBS also showed that the increase of MEP amplitude attenuated 20–30 min post-iTBS (Corp et al., 2020). Given that MEP amplitude measured 25 min post-iTBS previously showed a sustained facilitation for young participants (18–28 years), but returned to baseline for older participants (65–76 years) (Dickins et al., 2015), the apparent discrepancy between my results

and those of previous studies (Corp et al., 2020; Hamada et al., 2013) may be due to the difference in participants age. In the studies by Hamada et al. and Corp et al., the mean age was 30.3 and 41.9 years, respectively, whereas participants in the present study were all in the range of young participants (20–24 years, mean age 21.7 years).

2.4.2 Negative correlations of regional WM FA with early-phase MEP amplitude change

The early-phase MEP amplitude change was negatively correlated with regional FA values in WM tracts related to motor function, including the right corticospinal tract (WM 1), right superior longitudinal fasciculus (WM 1) and corpus callosum (WM 2 and 3), which are functionally and anatomically connected to M1 (Catani and de Schotten, 2012). The corticospinal tract sends output from M1 to the contralateral spinal cord and ultimately to distal muscles (Lemon, 2008) and output strength (number of motor neurons recruited) determines MEP amplitude (Bestmann and Krakauer, 2015). The superior longitudinal fasciculus is the main intra-hemispheric tract connecting frontal areas (e.g., premotor cortex, dorsolateral prefrontal cortex [DLPFC], and M1) and parietal areas (e.g., angular gyrus and supramarginal gyrus), and is crucial for motor planning, motor imagery, and visuo-motor tasks (Nakajima et al., 2020). The corpus callosum connects the bilateral M1 (Hofer and Frahm, 2006) and mediates both interhemispheric inhibition (Ferbert et al., 1992) and facilitation (Hanajima et al., 2001).

The FA values within a part of the corpus callosum that connects bilateral frontal regions (WM 2 and 3), right forceps minor (WM 4, 5, 9, and 10), and left internal capsule (WM 6–8) were also negatively correlated with MEP amplitude change. Given that these tracts are not directly connected to the right M1, their microstructural properties may be similar to those of the WM connecting to the right M1. The similarity is possibly mediated by factors affecting the general WM functional properties, such as the gene polymorphisms of

the brain derived neurotrophic factor, which was known to influence the microstructural properties of WM (Chiang et al., 2011).

Further examination of the associations between regional FA values in WM and both NDI and ODI, which respectively reflect the density and the dispersion of orientation of neurites within a voxel (Zhang et al., 2012), provided clues to the nature of these microstructural differences underlying individual variation in iTBS after-effect. A larger MEP change was associated with lower FA in multiple tracts, and in several of these tracts (including right superior longitudinal fasciculus and right corticospinal tract of WM 1, right forceps minor in WM 4 and 5, and left anterior limb of internal capsule in WM 6), FA was negatively correlated with NDI (Figure 2.5a), while FA and ODI were negatively correlated in all clusters (Figure 2.5b). Therefore, lower FA values in WM 1, 4, 5, 6, and 10 are associated with larger MEP amplitude change, less consistent fiber orientation (higher dispersion), and a smaller neurite fraction, possibly reflecting smaller diameter of neural fibers or lower myelination. Alternatively, lower FA values in the other WM clusters may reflect only less consistent fiber orientation.

2.4.3 Negative correlations of regional gray matter FA with late-phase MEP amplitude change

In contrast to the early phase, the late-phase MEP amplitude change was negatively correlated with regional gray matter FA, primarily in the right frontal cortex (GM 1–3). These regions include right premotor cortex (GM 1), right DLPFC (GM 1), and right anterior prefrontal cortex (aPFC) (GM 2), all of which are implicated in motor function. The premotor cortex is crucial for motor planning and encoding these plans to M1 for execution (Hoshi and Tanji, 2007), while the DLPFC integrates inputs from multiple sensory modalities to decide on the action to take (Yarrow et al., 2009) and the aPFC is important for motor response

inhibition such as in go/no-go tasks (Boecker et al., 2007; Wriessnegger et al., 2012). Both the premotor cortex (Bäumer et al., 2009; Civardi et al., 2001; Groppa et al., 2012; Koch et al., 2007) and DLPFC (Cao et al., 2018; Hasan et al., 2013) modulate the activity of ipsilateral M1. Furthermore, the premotor cortex was shown to modulate the plasticity of ipsilateral M1 (Huang et al., 2018).

The late-phase MEP amplitude change was also negatively correlated with FA in the right postcentral gyrus (GM 4 and 5) and right insula (GM 1). The postcentral gyrus provides sensory feedback to M1 (Kaelin-Lang et al., 2002) and M1 modulates activity of the postcentral gyrus (Katayama and Rothwell, 2007), suggesting reciprocal functional connections. The insula is a part of the saliency network and facilitates motor responses indirectly via the anterior cingulate cortex (Menon and Uddin, 2010).

The FA values of GM 1–3 (right frontal regions, right insula, and right temporal regions) were also negatively correlated with ODI (Figure 2.6b), indicating that the greater MEP amplitude change associated with lower FA may reflect more complex dendritic branching (Zhang et al., 2012). By contrast, the FA values of GM 4–5 (the right postcentral gyrus) were positively correlated with NDI (Figure 2.6a), suggesting that a larger late-phase after-effect may be facilitated by a lower density of apical dendrites (Ball et al., 2013; Zhang et al., 2012). Therefore, I speculate that the structure of dendrites in the GM might affect the late-phase MEP amplitude change.

2.4.4 Microstructural properties may influence the after-effect of iTBS

I found that the microstructural properties of non-M1 regions correlated with the iTBS after-effect. In addition to M1, non-M1 regions structurally connected to M1 were previously shown to regulate the MEP amplitudes. For example, the MEP amplitudes were affected by activities in M1 located contralateral to the stimulated side (Dickins et al., 2015), but also in

ipsilateral prefrontal regions, such as premotor cortex and DLPFC, connected to the stimulated M1 (Bäumer et al., 2009; Cao et al., 2018; Civardi et al., 2001; Groppa et al., 2012; Hasan et al., 2013; Koch et al., 2007). Moreover, the activities of prefrontal regions were shown to modulate the iTBS after-effect on ipsilateral M1 (Huang et al., 2018). These studies suggest that the activities of non-M1 regions contribute to determining the iTBS after-effect on M1. However, the degree of contribution to the early- and late-phase after-effect and its relationship to the microstructural properties of white and gray matters are still open questions.

Besides the contribution of non-M1 regions, several neural mechanisms might explain the distinct early- and late-phase iTBS after-effects. First, short-term potentiation is reflected more in the early phase than in the late phase (Ugawa, 2012). Second, gene expression associated with the long-term potentiation of excitatory and inhibitory interneurons were facilitated 10–20 min after iTBS (i.e., during the early phase), while that of inhibitory interneurons was suppressed 20–40 min after iTBS (i.e., during the late phase) (Hoppenrath and Funke, 2013). While these results suggest the involvement of different mechanisms in the early and late phases of MEP amplitude change, how they respectively relate to the white and gray matter structures remains unclear. Future studies are warranted to clarify the physiological mechanisms which underlies the relationship between microstructural properties and the MEP amplitude changes.

One might also ask how the iTBS after-effect is coupled with the functional and structural changes in remote regions. The after-effect on remote regions can be assessed with structural (Jung and Lambon Ralph, 2021) and functional (Jung and Lambon Ralph, 2016; Nettekoven et al., 2014) MRI. It would be appealing to investigate the relationship between structural and functional changes measured by MRI and the iTBS after-effect. Future studies

are also necessary to compare the MEP and MRI measurements between pre- and post-iTBS and investigate its relationship.

Surprisingly, in the current study, the FA in M1 was not predictive of the MEP amplitude change. Substantial differences between the anatomical structure of M1 and other cortical areas might explain the significant effects in remote regions contrary to M1. First, layer V in M1 is much thicker than that in other cortical areas (Brodmann, 1909). Second, the giant pyramidal neurons named "giant Bets cells" were exclusively localized to the layer V of M1 (Lassek, 1941). Because of these unique properties of M1, we speculate that the restriction of water determining the FA values in M1 mainly reflects a microstructural property of the somata of layer V neurons. By contrast, the restriction of water determining FA values in the prefrontal regions would reflect the property of dendrites, structures which are mainly found across layers. Supporting the idea that dendrites are key for determining the after-effect of iTBS, I found a correlation with the MEP amplitude change in prefrontal regions but not in M1. Future neuroimaging studies with a higher spatial resolution are needed to determine whether the microstructural properties of the GM in M1 predict the magnitude of iTBS after-effect.

2.4.5 Limitations

Potential limitations of this study include the use of FA to evaluate the microstructural properties of GM, as FA may not be as sensitive an indicator of GM properties due to the relatively large partial-volume effect (Aggarwal et al., 2015). To resolve this issue, I analyzed FA only in the middle part of the GM (Stock et al., 2020) or along the major structures of the WM (Smith et al., 2006), which I believe helped to minimize the impact of the partial-volume effect. Furthermore, previous dMRI studies with higher spatial resolution have demonstrated the validity of FA for quantifying and distinguishing the structures of cortical layers

(Aggarwal et al., 2015; McNab et al., 2013). Nonetheless, I cannot rule out the possibility that the analyzed regions are affected by partial-volume effects from surrounding areas. Future neuroimaging studies with higher spatial resolution are needed to clarify how microstructural properties in regions associated with M1 influence the after-effect following iTBS.

Constituting another limitation of the current study, I stimulated the right M1 instead of the left M1, contrary to previous studies investigating the after-effect of iTBS on M1 (Corp et al., 2020). Nevertheless, several iTBS studies targeted the right M1 to assess the plasticity of M1 (Ding et al., 2021; Platz et al., 2018; Suppa et al., 2008). Furthermore, Suppa and colleagues reported that performing TBS over M1 of the dominant or non-dominant hemisphere did not significantly affect the MEP amplitude change on the contralateral FDI muscle (Suppa et al., 2008). This finding suggests that stimulating the right instead of left M1 in the current study would not affect the MEP amplitude changes.

2.4.6 Conclusions

The microstructural properties of certain WM regions are negatively associated with the magnitude of the early-phase iTBS after-effect, while the microstructural properties of certain gray matter regions are negatively associated with the magnitude of the late-phase iTBS after-effect. These results suggest that FA measured by dMRI can be a powerful tool for prediction of experimental and therapeutic iTBS responses.

Chapter 3. Microstructural changes induced by quadripulse stimulation

This chapter is partly adapted from "Quadripulse stimulation: A replication study with a newly developed stimulator." Brain Stimulation, 15 (3), 579-581, Ikko Kimura, Yoshikazu Ugawa, Masamichi J. Hayashi, Kaoru Amano.

3.1 Introduction

Neural activity shapes the underlying structure of its activity. Several animal studies have suggested that repeated activation of neurons increases dendritic spines (Engert and Bonhoeffer, 1999), enlargens astrocytes (Sagi et al., 2012), and induced myelination in the white matter near the activated neurons (Gibson et al., 2014) (See (Sampaio-Baptista and Johansen-Berg, 2017) for a review). Several human studies have also observed microstructural changes in the brain 24 h after neural intervention (Lazari et al., 2022; Sampaio-Baptista et al., 2021; Scholz et al., 2009), suggesting that structural plasticity may also occur in the adult human brain. Since brain functions can change in both normal (e.g., behavioral training) and abnormal (e.g., stroke, brain tumor, or epilepsy) situations, it is crucial to elucidate how functional changes are related to microstructural changes.

While many studies have examined structural plasticity more than a day after neural interventions (Sampaio-Baptista and Johansen-Berg, 2017), several studies suggest that microstructural changes can also occur immediately after the intervention (Johansen-Berg et al., 2012). Sagi et al. showed that the microstructures revealed by diffusion MRI (dMRI) were modulated immediately after a single session of a spatial memory task (Sagi et al., 2012). A recent study also showed that microstructural changes can be observed immediately after 45 min of motor training (Tavor et al., 2020). Although this type of structural plasticity

in the ultra-acute phase is also important in unraveling its association with functional changes, behavioral training only enhances brain activity (Bueichekú et al., 2019). Therefore, it is still unclear whether the microstructure changes immediately after an increase or decrease in brain activity of a specific region. The comparison between facilitation and suppression is crucial because facilitation (e.g., epilepsy) or suppression (e.g., stroke or brain tumor) of brain activity can occur in abnormal situations; hence, it is important to reveal the differences in underlying mechanisms induced after the facilitation and suppression of brain activity.

Brain activity can be bidirectionally modulated by repetitive transcranial magnetic stimulation (rTMS). This method can noninvasively facilitate or suppress the brain activity of a specific region to examine the direct effects of neural intervention (Walsh and Cowey, 2000).Therefore, microstructural changes after both facilitation and suppression of brain activity in the left primary motor cortex (M1) by rTMS were studied, whereas a few previous studies have investigated microstructural changes immediately after either the excitatory (Niehaus et al., 2000) or inhibitory (Abe et al., 2014; Duning et al., 2004; Mottaghy et al., 2003) rTMS protocol. I hypothesized that the microstructural properties would also change immediately after both excitatory and inhibitory rTMS protocols, and that the degree of change might differ after the facilitation or suppression of brain activity. This knowledge is important not only for clarifying the structural plasticity in the ultra-acute phase but also for elucidating the potential of rTMS as a method to modulate the microstructural properties of the human brain.

3.2 Validation on the efficacy of a new developed QPS stimulator

Here, I evaluated the after-effect of QPS by the stimulator applied in this experiment. QPS is one of patterned rTMS protocols, inducing four pulses every 5s for 30min (Hamada et al., 2007). While QPS with short interpulse interval (QPS5) enhances the brain activity of the stimulated region, QPS with long interpulse interval (QPS50) suppresses the activity (Hamada et al., 2007). Compared to other rTMS protocols, namely PAS (Hamada et al., 2007) and TBS (Tiksnadi et al., 2020), the after-effect of QPS was shown to be relatively strong and robust. Moreover, the after-effect of QPS targeting the left M1 was not affected by the gene polymorphisms of brain derived neurotrophic factor (Nakamura et al., 2011) and the muscle contraction after the stimulation (Kadowaki et al., 2016), both of which generally affect the rTMS after-effect (Ridding and Ziemann, 2010). Therefore, QPS is one of the promising rTMS protocols for neuro-modulational research and treatment.

The stimulator I applied in this experiment was a new stimulator specifically designed for QPS recently developed by DeyMed Diagnostic (DuoMAG MP-Quad, https://deymed.com/duomag-qps). The properties of the after-effect with this stimulator were expected to parallel those obtained with another stimulator, the Magstim stimulator, which is currently used in psychological and clinical research but not commercially available anymore (Hamada et al., 2008; Matsumoto and Ugawa, 2020). Nevertheless, experimental validation of DuoMAG MP-Quad is still warranted since the degree of after-effect may differ across stimulators considering that the waveform of stimulation pulses slightly differs between manufacturers (Wessel et al., 2019). Therefore, I studied the QPS after-effect induced by the DuoMAG MP-Quad stimulator.

The participants were thirteen healthy adult volunteers comprising five females, 20–24 years of age (mean ± standard deviation: 21.5 ± 1.3). They were right-handed without a history of neurological or psychiatric disorders. The experiments were approved by the

local ethics committee and safety committees at the National Institute of Information and Communications Technology and were performed in accordance with the Declaration of Helsinki. All participants provided informed consent. My study comprised two sessions with a within-subject design, applying either QPS5 or QPS50 in each session. These two sessions were separated by over a week, while their order was randomly assigned and counterbalanced across the participants. QPS was delivered over the left primary motor cortex (M1) using DuoMAG MP-Quad (Deymed Diagnostic s.r.o., Hronov, Czech Republic) with a butterfly-shaped 70-mm air-cooling coil (DuoMAG 70BF Air Cooled Coil; Deymed Diagnostic s.r.o., Hronov, Czech Republic). Throughout the session, motor evoked potentials (MEPs) were recorded from the right first dorsal interosseous (FDI) muscle using a Brainsight surface-electromyogram (Rogue Research Inc., Montreal, Canada).

In each session, I first localized the hotspot, defined as the location evoking the largest MEPs, for the right FDI, and measured active motor threshold (AMT), defined as the intensity evoking MEPs larger than 100 mV in 5 out of 10 trials, with a slight contraction of the right FDI (around 10% of maximum voluntary contraction). I then measured 30 MEPs at the intensity evoking around 500 mV of MEPs in the relaxed FDI as a baseline (pre-QPS). I further assessed alertness of the participants with a Stanford Sleepiness Scale (SSS; one participant presenting SSS larger than four was excluded) (Hoddes, 1972). Subsequently, I applied QPS over the hotspot with one burst of four monophasic pulses delivered every 5 s for 30 min with an intensity of 90% AMT (Hamada et al., 2008). After applying QPS, I measured 20 MEPs every 10 min until 90 min after QPS (post-10 to post-90) using the same intensity as for the pre-QPS. The coil position was monitored with a Brainsight (Rogue Research Inc., Montreal, Canada) to confirm stable coil position.

To evaluate the overall after-effect in QPS5 and QPS50, I first compared the MEPs between pre- and post-QPS (post-10 to post-90) for each QPS protocol. The grand mean

MEP amplitudes of post-QPS normalized to pre-QPS (normalized MEP) was 1.71 ± 0.41 (from below mean ± standard deviation) in QPS5 and 0.82 ± 0.23 in QPS50 (Figure 3.1A). Two-tailed paired Student's t-tests of the absolute MEP amplitude between pre- and post-QPS revealed significant enlargement after QPS5 ($P < 0.001$, $d' = 1.40$) and significant reduction after QPS50 ($P = 0.019$, $d' = -0.80$).

To evaluate the time-course of MEPs, I separated the time-course into three time-blocks (post-10–30, post-40–60, and post-70–90), then averaged MEPs among each time-block (Tiksnadi et al., 2020). The mean of normalized MEP in post-10–30, post-40–60, and post-70–90 was 1.51 ± 0.36, 1.79 ± 0.48, 1.79 ± 0.48, respectively, for QPS5 (Figure 3.1B), and 0.84 ± 0.32, 0.80 ± 0.26, and 0.83 ± 0.17, respectively, for QPS50 (Figure 3.1C) (see Figure 3.2 for the individual time courses of MEPs). Repeated-measures one-way ANOVA revealed significant effect of time-block in QPS5 ($P < 0.001$, $\eta^2 = 0.60$) and moderate effect of time-block in QPS50 ($P = 0.051$, $\eta^2 = 0.24$). Post-hoc paired t-tests of the absolute MEP amplitude with correction for multiple comparisons using the Holm's method also showed significant enlargement in all time-blocks by QPS5 (post-10–30, $P = 0.002$, $d' = 1.14$; post-40–60, $P = 0.001$, $d' = 1.35$; post-70–90, $P = 0.001$, $d' = 1.42$), together with a moderate reduction in post-10–30 and significant reduction in post-40–60 and post-70–90 by QPS50 (post-10–30, $P = 0.093$, $d' = -0.53$; post-40–60, $P = 0.030$, $d' = -0.90$; post-70–90, $P = 0.047$, $d' = -0.76$). In terms of baseline physiological parameters, no significant differences were found in AMT ($P = 0.73$), stimulus intensity (SI) for recording MEPs ($P = 0.49$), SI for applying QPS ($P = 0.68$) or mean baseline MEP amplitude ($P = 0.29$) (Figure 3.1D) between the QPS5 and QPS50 sessions. These findings confirm steady experimental conditions across the sessions.

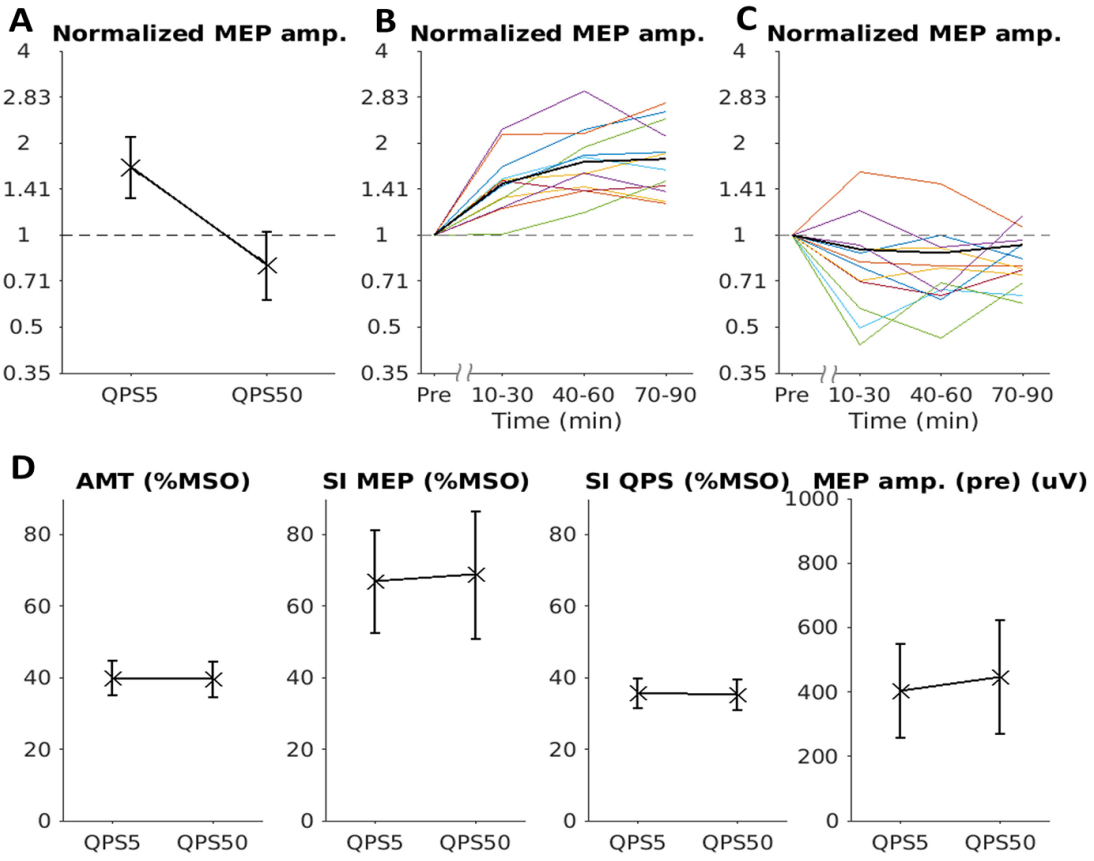

Figure 3.1 (A–C) Motor evoked potentials (MEPs) measured after QPS. (A) shows the grand-mean MEP amplitudes pooled across all post periods (post-10 to post-90), while (B) and (C) show the individual time courses of MEP amplitudes after QPS5 and QPS50, respectively. The vertical axis indicates the MEP amplitudes normalized by the baseline MEP amplitude in log scale, while the horizontal axes indicate QPS condition (A) or the time-block after QPS (B, C). (D) Comparison of baseline neurophysiological features between the QPS5 and QPS50 protocols. The active motor threshold (AMT), stimulus intensity (SI) for recording MEPs, SI for applying QPS, and mean baseline MEP amplitude are shown. The vertical axis of the left three panels shows the percentage of maximum stimulator output (% MSO), while the vertical axis of the rightmost panel shows the mean baseline MEP amplitude (micro volt). The mean (black cross) and standard error (error bar) are also provided.

As expected from previous studies using the Magstim stimulator (The Magstim Co. Ltd., Whitland, UK) (Hamada et al., 2008; Nakamura et al., 2016; Tiksnadi et al., 2020),

MEPs were bidirectionally modulated for over 60 min by QPS with the newly developed

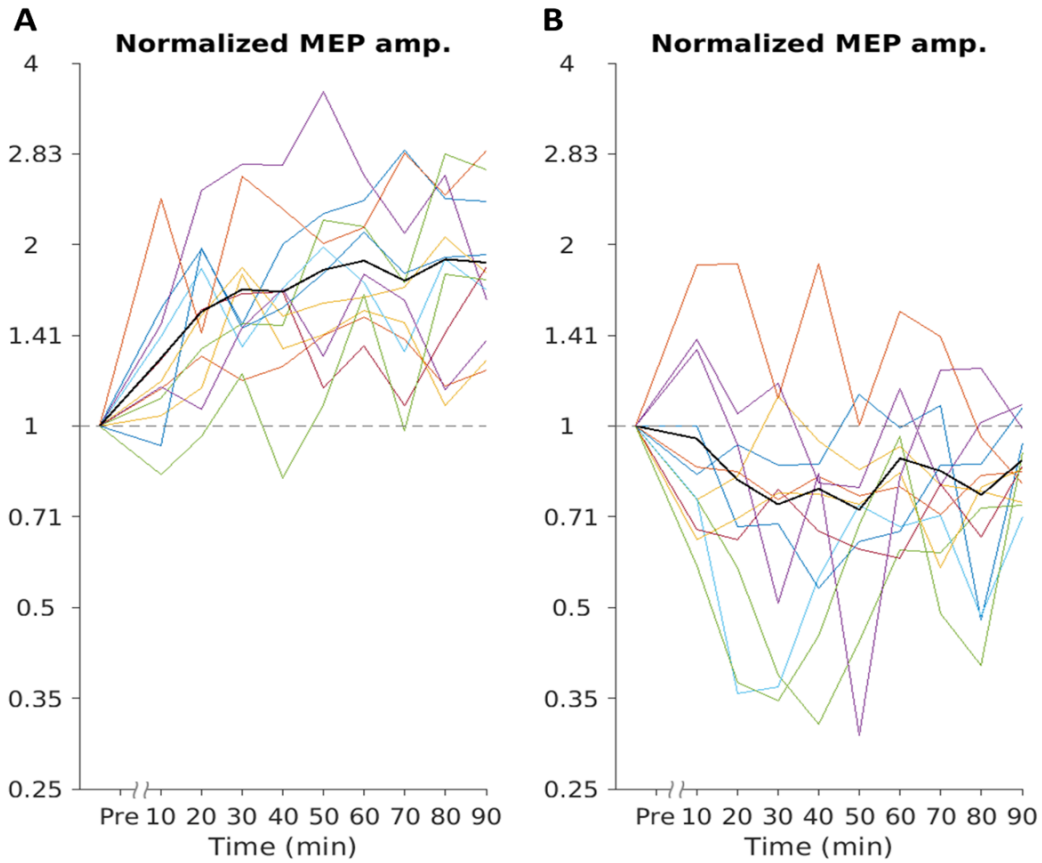

Figure 3.2 Individual time courses of MEP amplitude after QPS5 (A) and QPS50 (B). The vertical axis indicates the MEP amplitude normalized by the baseline MEP amplitude in log scale, while the horizontal axis indicates the time after QPS in minutes.

stimulator. In previous studies, the grand mean normalized MEP was around 2.0 (Hamada et al., 2008), 1.60 (Nakamura et al., 2016), and around 1.2 (Tiksnadi et al., 2020) in QPS5, versus around 0.5 (Hamada et al., 2008), 0.67 (Nakamura et al., 2016), and around 0.8 (Tiksnadi et al., 2020) in QPS50. The grand means of normalized MEP measured in the present study (1.71 ± 0.41 in QPS5 and 0.82 ± 0.23 in QPS50) were comparable to those induced by the Magstim stimulator. These effects induced by the newly developed stimulator are supported by previous observations showing that short-interval intracortical inhibition is not sensitive to slight differences in TMS pulse waveform (Wessel et al., 2019). In the present study, the effect sizes of MEP-changes after QPS50 were found to be smaller than those

measured after QPS5. A similar trend was reported in previous studies (Hamada et al., 2008; Nakamura et al., 2016; Tiksnadi et al., 2020).

Together, these findings reveal that the newly developed QPS stimulator is as effective as the original QPS stimulator (Hamada et al., 2008). A promising approach to boost the after-effect of QPS50 would be to combine QPS with afferent electric stimulation of the peripheral nerves using paired-associative QPS (Wiratman et al., 2017).

3.3 Materials and Methods

The study consisted of three days of experiments (Figure 3.3). On Day 1, task functional MRI (fMRI) data were collected to localize the M1 responsible for the right FDI muscle. Structural MRI data were collected on the same day (Figure 3.3A). On Days 2 and 3, the participants underwent either QPS5 or QPS50. Before and after quadri-pulse stimulation (QPS), resting-state fMRI (rsfMRI) and dMRI data were obtained to assess the functional and microstructural changes in QPS, respectively (Figure 3.3B). Days 2 and 3 were both performed in the afternoon, from 1 pm to 3 pm, and were separated for more than a week to avoid any cumulative effects. QPS5 and QPS50 were randomly assigned to Days 2 and 3 and the order was counterbalanced across participants.

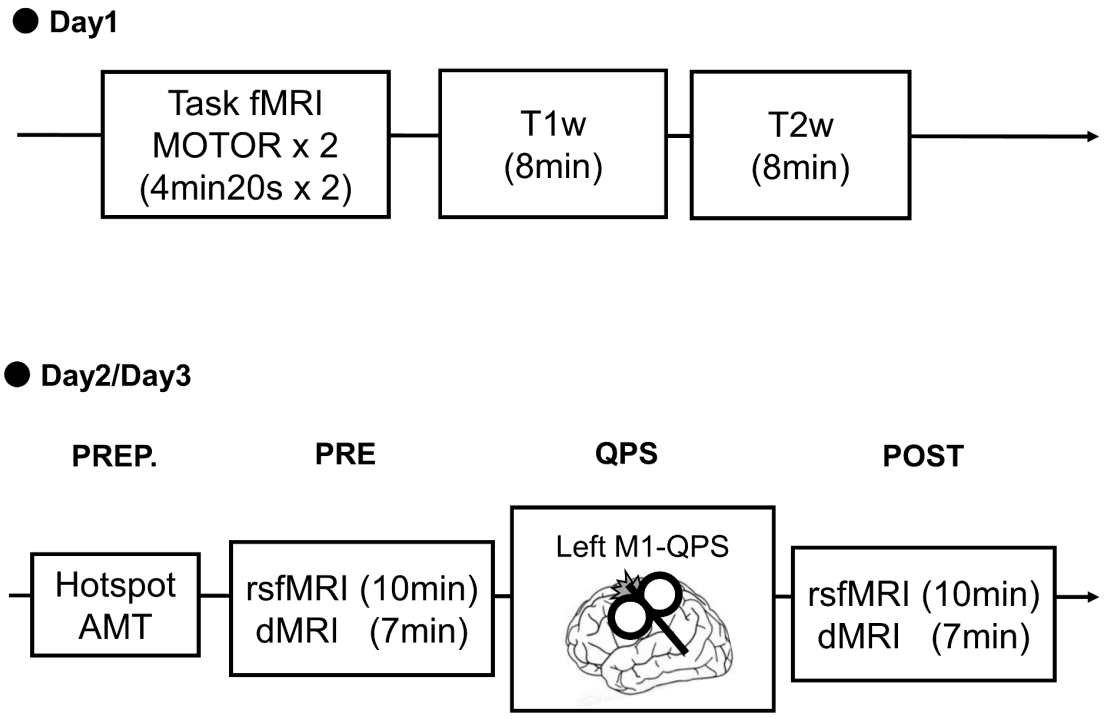

Figure 3.3 Overview of the experimental protocol to assess the microstructural changes after QPS over the primary motor cortex (M1). On Day 1, task fMRI (tfMRI) data were acquired during a finger tapping task (MOTOR) to localize the left M1, while T1w and T2w images were obtained to spatially normalize the diffusion MRI (dMRI) and resting-state fMRI (rsfMRI) data. On Days 2 and 3, either QPS5 or QPS50 was performed. First, stimulus location (hotspot for left M1) and stimulus intensity (active motor threshold; AMT) were

defined in the preparation step (PREP.). Before and after QPS, participants underwent dMRI and rsfMRI scans.

3.3.1 Participants

Sixteen healthy adult volunteers (eight males; age range 20–25 years; mean age 22.7 years, standard deviation (SD) 1.4 years) participated in this study. All participants were right-handed according to the Edinburgh handedness inventory (mean score 95.05, SD 9.8) and reported no history of neurological or psychiatric disorders. The experiments were approved by the Institutional Ethics and Safety Committees of the National Institute of Information and Communications Technology, and were performed in accordance with the Declaration of Helsinki. Informed consent was obtained from all participants after providing them with a full explanation of the study protocols and objectives.

3.3.2 Quadripulse Stimulation

Participants underwent QPS5 or QPS50 over the left M1, targeting the right FDI muscle, using the same procedure as described in Section 3.2. In brief, the motor hotspot for the right FDI muscle was first determined, and from this hotspot, the active motor threshold (AMT) was defined (evoking motor evoked potentials [MEPs] larger than 100 mV in 5 out of 10 trials with mild contraction of the right FDI). The QPS was then applied with a burst of four monophasic pulses every 5 s for 30 min, and the stimulus intensity was set at 90% of the AMT. The inter-pulse interval for QPS5 was 5 ms, while that for QPS50 was 50 ms. These procedures were performed with a DuoMAG MP-Quad (Deymed Diagnostic s.r.o., Hronov, Czech Republic) equipped with a butterfly-shaped 70-mm air-cooling coil (DuoMAG 70BF Air Cooled Coil; Deymed Diagnostic s.r.o., Hronov, Czech Republic), and MEPs were collected using a Brainsight surface-electromyogram (Rogue Research Inc., Montreal,

Canada). To quantitatively assess the stability of the coil position during QPS, the position was recorded using a Brainsight (Rogue Research Inc., Montreal, Canada). The mean distance error of the coil position and the mean angle or twist error of the coil handle relative to the target position of the coil were calculated in each QPS session to evaluate the quality of QPS application in each session.

3.3.3 Image Acquisition

On Day 1, two sessions of task fMRI data during a finger tapping task and structural MRI data were acquired using a Siemens PrismaFit 3T scanner equipped with a 32-channel array head coil (Siemens, Erlangen, Germany). On Day 2 and 3 , rsfMRI and dMRI data before and after QPS were obtained using a Siemens Vida 3T scanner equipped with a 64-channel array head-neck coil (Siemens, Erlangen, Germany).

Functional MRI data during a finger tapping task

To identify the left M1 responsible for the right index finger and define its location as the seed region for the subsequent seed-based correlation analysis, two sessions of fMRI data were collected while participants tapped their right or left index fingers, as described in a previous study (Watanabe et al., 2014). Each session consisted of six blocks of 20 s with an inter-block interval of 20 s and took 4 min 20 s in total. In each block, participants were required to tap their left or right index fingers synchronized with the center red circle (radius 1 °) flashing at 1 Hz. These fMRI data were collected with a gradient-echo echo-planar sequence, and the slices were collected in an interleaved order. The other acquisition parameters were as follows: flip angle, 60 °; voxel size, 2 × 2 × 2 mm; matrix size, 108 × 108 × 78; Multiband Acceleration Factor = 6, phase-encoding direction, anterior-posterior; TR, 1000 ms; and TE, 30 ms.

A pair of B0 field maps in both phase-encoding directions (i.e., anterior–posterior and posterior–anterior) were also obtained to correct for susceptibility-induced distortion in fMRI data. These field maps were collected using a spin-echo echo-planar sequence with the following parameters: flip angle = 90 °, voxel size = 2 × 2 × 2 mm, matrix size = 108 × 108 × 78, Multiband Acceleration Factor = 1, TR = 8330 ms, and TE = 63.40 ms.

Structural MRI data

T1-weighted (T1w) and T2-weighted (T2w) images were obtained for neuronavigation of the TMS coil during QPS on Days 2 and 3 and for spatial normalization of MRI data. A T1w image was obtained with a magnetization-prepared rapid acquisition with a gradient echo (MPRAGE) sequence with the following parameters: flip angle = 8 degrees, voxel size = 0.8 × 0.8 × 0.8 mm, matrix size = 224 × 320 × 320, TI = 1000 ms, TR = 2500 ms, and TE = 2.18 ms. A T2w image was obtained with a sampling perfection with application optimized contrast using different flip angle evolution (SPACE) sequence with the following parameters: flip angle = 8 degrees, voxel size = 0.8 × 0.8 × 0.8 mm, matrix size = 224 × 320 × 320, TR = 3200 ms, and TE = 564 ms. Total acquisition time for structural MRI was around 10 min.

Resting-state functional MRI data

On both Days 2 and 3, rsfMRI data were collected to assess the functional changes induced by QPS. These data were acquired with the same acquisition sequence and parameters as the task fMRI data on Day 1. During the scans, participants were required to gaze at a black cross located at the center of a screen for 10 min without any particular thoughts. As with task fMRI on Day 1, a pair of B0 field maps in both phase-encoding directions was obtained with the following parameters: flip angle = 90°, voxel size = 2 × 2 × 2 mm, matrix size = 108 ×

108 × 78, Multiband Acceleration Factor = 1, TR = 6240 ms, and TE = 44.00 ms. After each scan, each participant was required to self-evaluate their sleepiness during the scan using the Stanford Sleepiness Scale (Hoddes, 1972).

Diffusion MRI data

dMRI data were also acquired to assess the microstructural changes induced by QPS. These data were obtained using a 2D single-shot spin-echo echo-planar sequence with the following parameters: voxel size = 2 × 2 × 2 mm, matrix size = 106 × 106 × 75, iPAT reduction factor = 2, Multiband Acceleration Factor = 3, b = 1000 s/mm2, number of directions = 30, TR = 5000 ms, and TE = 71 ms. In each session before and after QPS, two sets of dMRI data were collected: one along with the phase-encoding direction anterior–posterior and the other with the reversed phase-encoding direction (posterior–anterior). For each dMRI data, three non-diffusion-weighted images were also obtained in every ten diffusion-weighted images with the same acquisition parameters as the diffusion-weighted images. The total acquisition time for dMRI was approximately 7 min in each session.

3.3.4 Image Analysis

For the preprocessing of MRI data, unless otherwise noted, the default settings of the preprocessing pipelines of the Human Connectome Project (HCP pipelines 4.3.0, https://github.com/Washington-University/HCPpipelines) were followed, the methods of which are detailed by Glasser et al. (2013). These pipelines utilize the FMRIB software library (FSL 6.0.5, https://fsl.fmrib.ox.ac.uk/fsl), FreeSurfer (Version 6.0.1, https://surfer.nmr.mgh.harvard.edu/ (Dale et al., 1999; Fischl et al., 1999)), and Connectome Workbench (Version 1.5.0, https://www.humanconnectome.org/software/connectome-workbench) to optimally

preprocess MRI data obtained in HCP-like fashion. After these preprocessing steps, the left M1 responsible for the right FDI from task fMRI data was defined and then seed-based correlation analysis on that seed was conducted using resting-state fMRI data obtained on Days 2 and 3. From the dMRI data, diffusion tensor imaging (DTI)-based metrics were calculated, namely fractional anisotropy (FA) and mean diffusivity (MD) values, to assess microstructural properties before and after QPS in each condition. Structural MRI data on Day 1 and resting-state fMRI data obtained before QPS on Days 2 and 3 were utilized to estimate the transformation from individual MRI data on the cerebral cortex to the MNI standard space with a multimodal surface matching algorithm (Robinson et al., 2018).

Structural MRI data

Structural MRI data obtained on Day 1 (i.e., T1w and T2w images) were preprocessed using "*PreFreeSurferPipeline.sh*," "*FreeSurferPipeline.sh*," and "*PostFreeSurferPipeline.sh*" in the HCP pipelines. Gradient nonlinearity correction was not applied because all participants' heads were placed in the conventional location (i.e., the isocenter) of the MR scanner. First, both T1w and T2w images were transformed to the ACPC space by rigid-body transformation to the Montreal Neurological Institute (MNI) standard space and brain extraction. A T2w image was co-registered to a T1w image, and the bias field was estimated from both the T1w and T2w images. After the bias field correction with this estimated bias field, these images were registered to the MNI standard space, and a modified version of the recon-all command was applied in FreeSurfer to preprocess MRI data with sub-millimeter spatial resolutions. This command generates the boundaries between the cerebrospinal fluid and gray matter (pial surface) and those between the gray and white matter (white surface) and extracts the subcortical structure. The midpoints between the pial and white surfaces were further calculated to create the mid-thickness surface. This surface was utilized to

project the fMRI or dMRI data for further surface-based analysis on the cerebral cortex. These surfaces and segmented subcortical volumes were combined and warped to the MNI standard space. Finally, T1w data were divided by T2w data to derive the myelin map (Glasser and Van Essen, 2011) to be projected onto the mid-thickness surface, which was utilized for multimodal surface matching in this study (See the *Multimodal surface matching section* below for more details regarding this).

Functional MRI data

Both task fMRI and rsfMRI data were first preprocessed using "*fMRIVolumeProcessingPipeline.sh*" and "*fMRISurfaceProcessingPipeline.sh*" in the HCP pipelines. First, image distortions caused by the inhomogeneity of the magnetic field were estimated using the corresponding B0 field maps. Then, with these estimated distortions, fMRI data were corrected for EPI image distortions, and motion correction was applied with rigid-body transformation. The corrected fMRI data were co-registered to the T1w image in the ACPC space with boundary-based registration and warped to the MNI standard space. The data in the cerebral cortex were projected onto the mid-thickness surface and resampled to the MNI standard space with spatial smoothing using a Gaussian kernel of 2 mm full-width half maximum (FWHM) along the surface. In contrast, the time series of the subcortical structures were extracted from the subcortical voxels defined from the structural MRI data using FreeSurfer. These voxels were warped to the MNI standard space and spatially smoothed with a Gaussian kernel of 2 mm FWHM.

To further denoise the time series of the rsfMRI data, the "hcp_fix" was applied to the HCP pipelines. This method is based on the FIX application of FSL, which performs spatial independent component analysis towards fMRI data to remove the noise components from these time series (Griffanti et al., 2014). These components were manually re-inspected

following the criteria described by Griffanti et al. (2017) and the noise components were regressed out from the time series. The mean framewise displacement (FD) was also calculated (Power et al., 2014) for each session to quantitatively assess the quality of the rsfMRI data in each session.

To define the left M1 responsible for the right index finger, a general linear model (GLM) analysis of task fMRI data was performed with "*TaskfMRIAnalysis.sh*" in the HCP pipelines. This script performs surface-based analysis based on the FEAT tools of the FSL. First, the data were high-pass filtered with a cut-off period of 160 s, and the event timings for tapping the right or left index finger were created with a box-car design in each session, with the contrast tapping the right index finger larger than the left one (RIGHT > LEFT). After applying a 1st-level GLM analysis, a 2nd-level GLM analysis was performed across sessions for each participant. Finally, a Permutation Analysis of Linear Models (PALM) application was used to perform a one-sample t-test towards the contrast RIGHT > LEFT across participants in the MNI standard space.

To quantify the functional changes induced by QPS in both the stimulated and non-stimulated regions, seed-based correlation analyses were conducted towards the rsfMRI data. Functional connectivity (FC) was used for this purpose because this measurement between the stimulated and non-stimulated regions was previously shown to be bidirectionally modulated by QPS (Watanabe et al., 2014). The seed was defined as a 5 mm radius of the peak location identified by the contrast RIGHT > LEFT of the group-level GLM analysis in task fMRI (i.e., the stimulated location) following a previous study (Watanabe et al., 2014). Pearson's correlation coefficient was calculated between the time series of the seed and that of each vertex or voxel in the whole brain. These coefficients were transformed using Fisher's z-transformation to conform to normal distribution.

Since a previous study showed that the change in the FC between the left and right M1 was correlated with the magnitude of the after-effect of QPS (Watanabe et al., 2014), Fisher's z-transformed Pearson's correlation was further calculated between the time series of the left and right M1. The right M1 was defined as a 5 mm radius of the peak location in the contrast LEFT > RIGHT. The functional change of QPS was measured by substituting the FC of these regions post-QPS with that of pre-QPS.

Multimodal surface matching

To further fine-tune the resampling strategy from the ACPC space to the MNI standard space of the measurements on the mid-thickness, "*MSMAllPipeline.sh*" was used in the HCP pipelines. This pipeline uses a multimodal surface matching tool (Robinson et al., 2014) of FSL customized for the HCP pipelines (MSMAll; (Glasser et al., 2016b; Robinson et al., 2018)), which utilizes multimodal features, such as the myelin map and the functional connectivity on each surface, for the registration from the ACPC space to the MNI standard space. After registration, the time-series fMRI data were resampled to the MNI standard space using the resampling strategy defined with this method.

Diffusion MRI data

To preprocess the dMRI data, "*DiffPreprocPipeline.sh*" was applied to the HCP pipelines. First, non-diffusion-weighted images were intensity-normalized and, from these images, image distortions caused by the inhomogeneity of the magnetic field were estimated. With these estimated distortions, the dMRI data were corrected for EPI image distortion and then corrected for eddy current and subject motion. These corrected images were co-registered with the T1w image in ACPC space using BBR. The quantitative measurements of the image

qualities in each scan, namely absolute and relative head motions, were calculated using the EDDY QC tools in the FSL.

After the preprocessing steps, the FA and MD values were calculated from the dMRI data with a command “dtifit” in FSL. The data of both the cerebral cortex and subcortical structures were then warped to the standard space using *NoddiSurfaceMapping* (https://github.com/RIKEN-BCIL/NoddiSurfaceMapping), the method of which is detailed in Fukutomi et al. (2018)). In brief, the data within the cerebral cortex were projected onto the mid-thickness surface and resampled to the MNI standard space with MSMAll, whereas those in the subcortical structures were warped to the MNI standard space. All these data were spatially smoothed with a Gaussian kernel of 2 mm FWHM.

To assess changes in the microstructural properties of white matter (WM), the tract-based spatial statistics (TBSS) tool of the FSL was applied (Smith et al., 2006). This method creates statistics for group-level voxel-wise analysis in WM, as detailed in my previous study (Kimura et al., 2021). In brief, the FA map of every individual was nonlinearly registered to the standard space, the main WM structure (skeleton) was created from the spatially normalized FA maps of all participants, and the FA and MD values were projected onto that skeleton.

3.3.5 Statistical Analysis

The FSL PALM application was used to test the statistical significance of the functional and microstructural changes before and after QPS and the difference in the changes induced by QPS5 and QPS50. Specifically, 10, 000 permutation tests with Threshold-Free Cluster Enhancement (Smith and Nichols, 2009) were applied to compare the FC of the left M1 and FA or MD values before and after QPS in each condition and between the changes after QPS5 and QPS50. The Bayes factor was further calculated in each comparison to investigate whether the statistical testing supported the hypothesis that there were no differences in

non-significantly different areas. The Bayes factor was calculated using bayesFactor (https://github.com/klabhub/bayesFactor). PALM was also utilized to explore the correlation between functional change (i.e., the change in FC between the left M1 and right M1) and the change in FA or MD values. All these p-values were corrected for family-wise errors to control for multiple tests.

To confirm that the neuroimaging results were not affected by other possible confounding factors, such as the stimulation intensity of QPS or the difference in image quality before and after QPS, these measurements were compared with a two-tailed paired t-test for continuous variables and with Wilcoxon signed-rank test for categorical variables. All analyses were performed using the JASP (ver. 0.16.0 for Windows, https://jasp-stats.org/), and $P < 0.05$ was considered statistically significant.

3.4 Results

All participants completed the three-day-long experiment without any adverse events. One session in QPS5 failed to be recorded by the Brainsight, and two sessions of task-fMRI could not be performed because of the difficulty in presenting the visual stimuli for the timing of the finger tapping. Paired t-tests revealed that there were no significant differences in AMT (t = 0.40, P = 0.70, Figure 3.4A) or stimulus intensity for QPS (t = 0.48, P = 0.64, Figure 3.4B) between the QPS5 and QPS50 conditions. There were no significant differences in the quality of the QPS-session (mean distance error, t = 0.77, P = 0.46, Figure 3.4C; mean angle error, t = -1.37, P = 0.19, Figure 3.4D; mean twist error, t = -0.56, P = 0.59, Figure 3.4E).

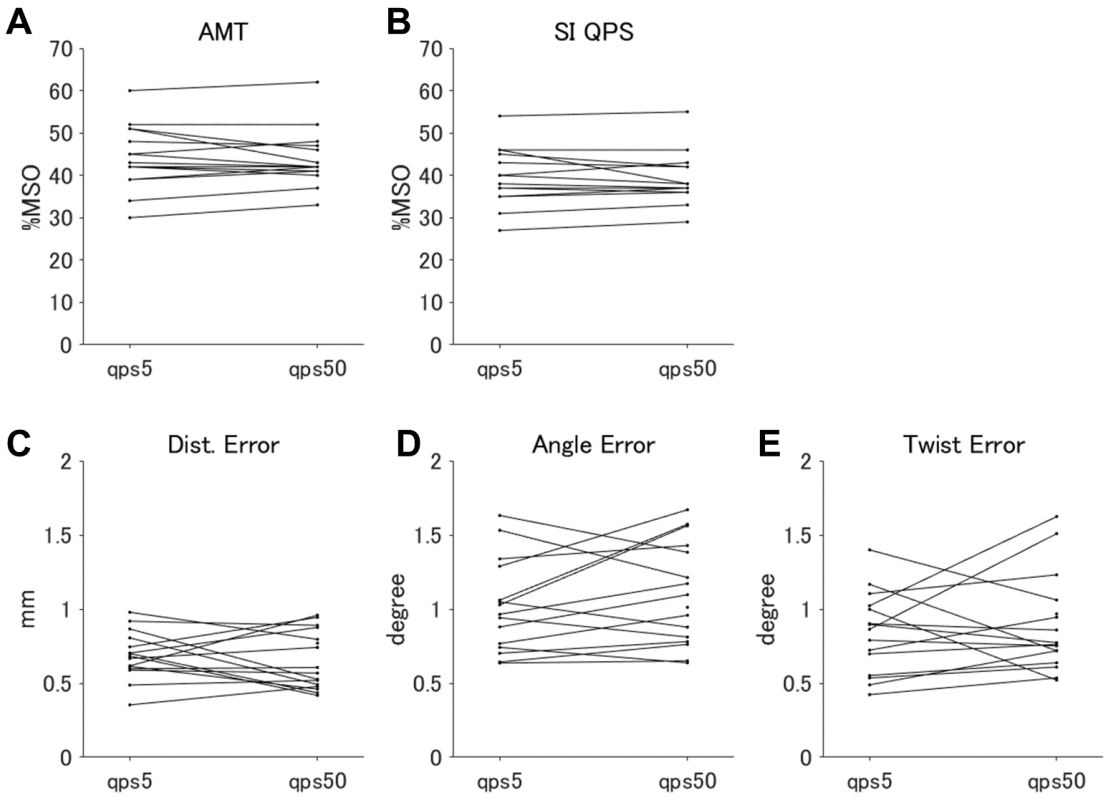

Figure 3.4 (A–B) Comparison of baseline neurophysiological features between the QPS5 and QPS50 conditions. The active motor threshold (AMT) and stimulus intensity (SI) for applying QPS were shown in (A) and (B), respectively. The vertical axes in the upper panel illustrate the percentage of maximum stimulator output (% MSO). (C–E) Comparison of the

quality in applying QPS between the QPS5 and QPS50 conditions. The mean distance error (mm; C), the mean angle error (degree; D), and the mean twist error (degree; E) in each session was shown.

3.4.1 The change of the microstructural property after quadripulse stimulation

The changes in the microstructural properties of the gray matter after QPS5 and QPS50 were then evaluated. The MD value significantly decreased in the bilateral cerebellum after both QPS5 (Figure 3.5A) and QPS50 (Figure 3.5B). No significant change in the FA value was observed after QPS5 or QPS50 (see Figure 3.6 and 3.7 for the effect size and Bayes factor comparing the FA value, respectively, and Figure 3.8 and 3.9 for the effect size and Bayes factor comparing the MD value, respectively). There was no significant difference in the changes in FA and MD values between the QPS5 and QPS50 conditions.

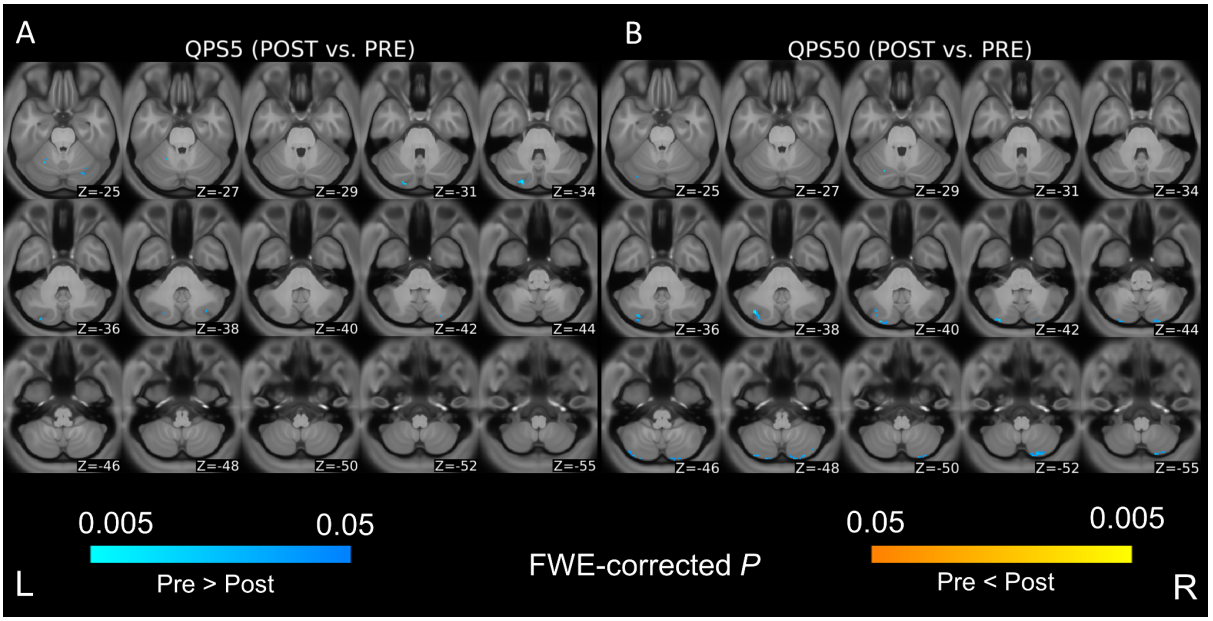

Figure 3.5. Differences in MD values between pre- and post-QPS in QPS5 (left panel) and QPS50 (right panel) conditions. Areas in blue show that MD was significantly decreased after QPS, while areas in yellow indicate that the value was significantly increased after QPS. Axial slices are shown in accordance with neurological conventions (the left side of the image is of the left of the brain) and are displayed in the MNI coordinates from z = -25 (top left) to z = -55 (bottom right).

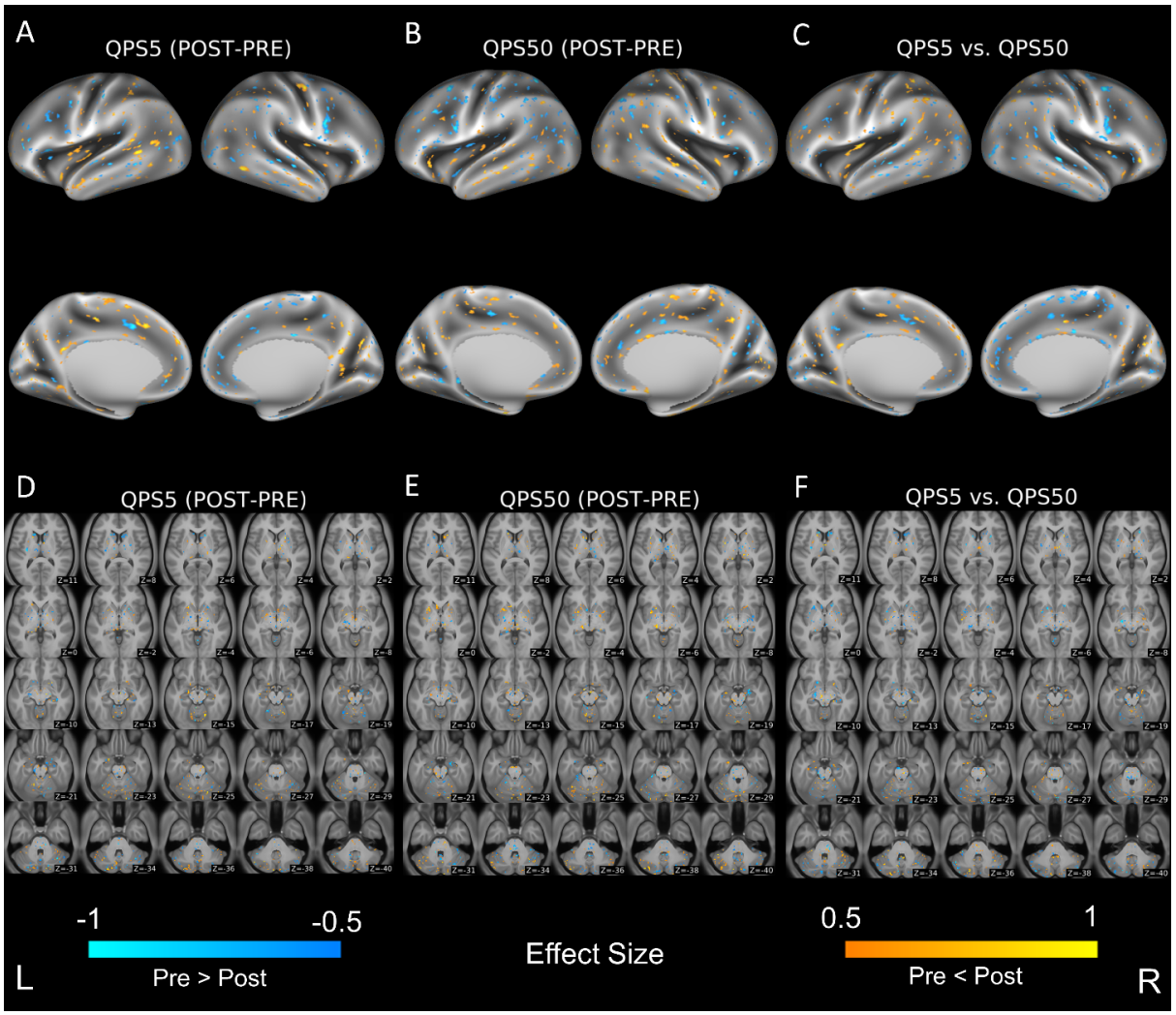

Figure 3.6 Differences in FA values of the cerebral cortex and subcortical regions between pre- and post-QPS in QPS5 (A and D) and QPS50 (B and E) conditions, and in changes of FA values across conditions (C and F). The upper panel (A–C) shows the result of surface-based analysis on the cerebral cortex, while the lower panel (D–F) shows that of voxel-based analysis in the subcortical regions. Areas in blue illustrate that the cohen's d of change in the value after QPS are smaller than -0.5, while those in yellow show that those values are higher than 0.5. Axial slices in (D–F) are shown in accordance with neurological conventions (left of the image is on the left of the brain) and are displayed in the MNI coordinates from z = 19 (left of the top) to z = -57 (right of the bottom).

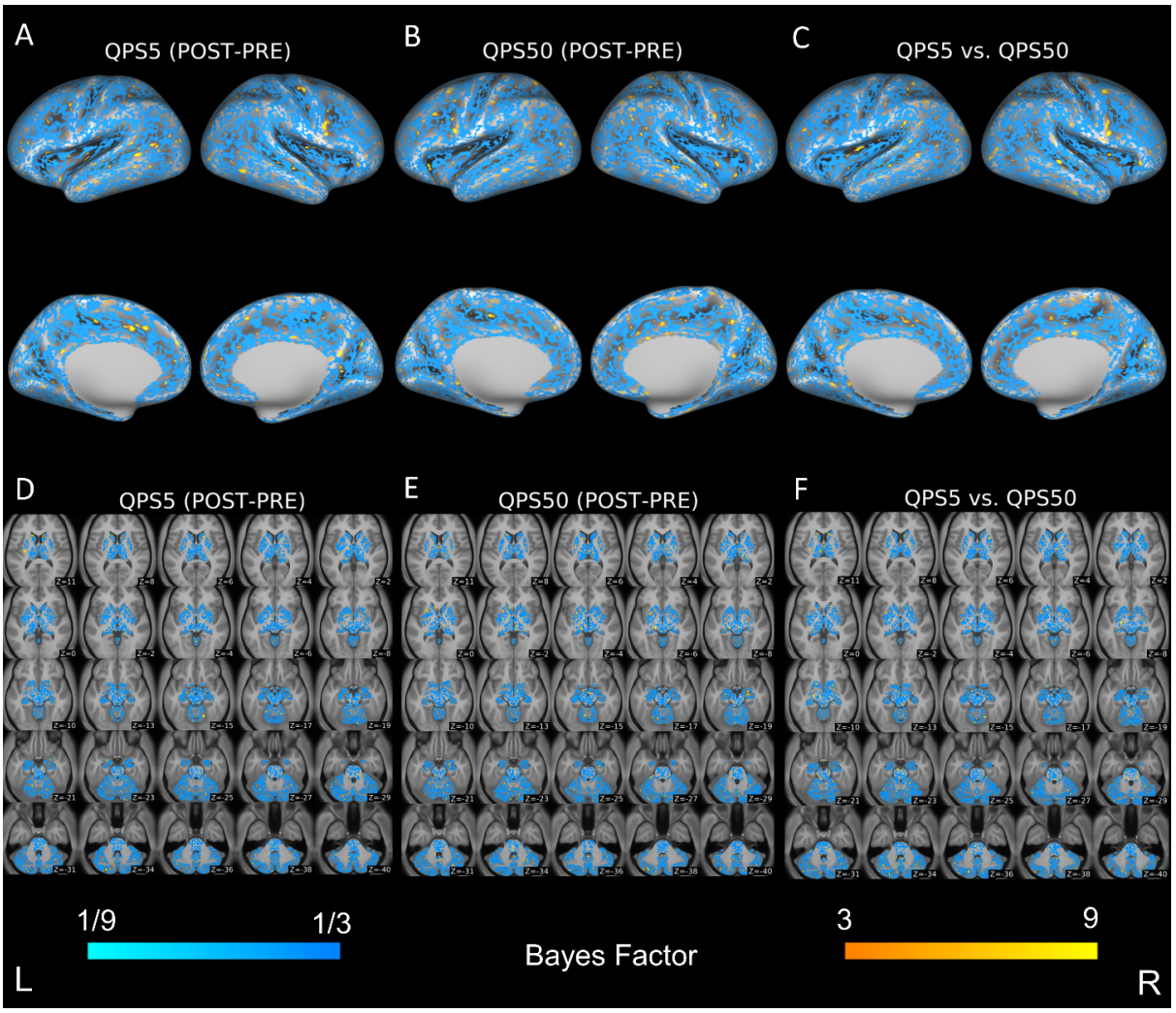

Figure 3.7 Differences in FA values of the cerebral cortex and subcortical regions between pre- and post-QPS in QPS5 (A and D) and QPS50 (B and E) conditions, and in changes of MD values across conditions (C and F). The upper panel (A–C) shows the result of surface-based analysis on the cerebral cortex, while the lower panel (D–F) shows that of voxel-based analysis in the subcortical regions. Areas in blue illustrate that the bayes factor was smaller than ⅓ in the comparison of the FA before and after QPS or the change of the FA across conditions (i.e., supports the hypothesis that the difference was zero). In contrast, those in yellow show those values are higher than 3. Axial slices in (D–F) are shown in accordance with neurological conventions (left of the image is on the left of the brain) and are displayed in the MNI coordinates from z = 19 (left of the top) to z = -57 (right of the bottom).

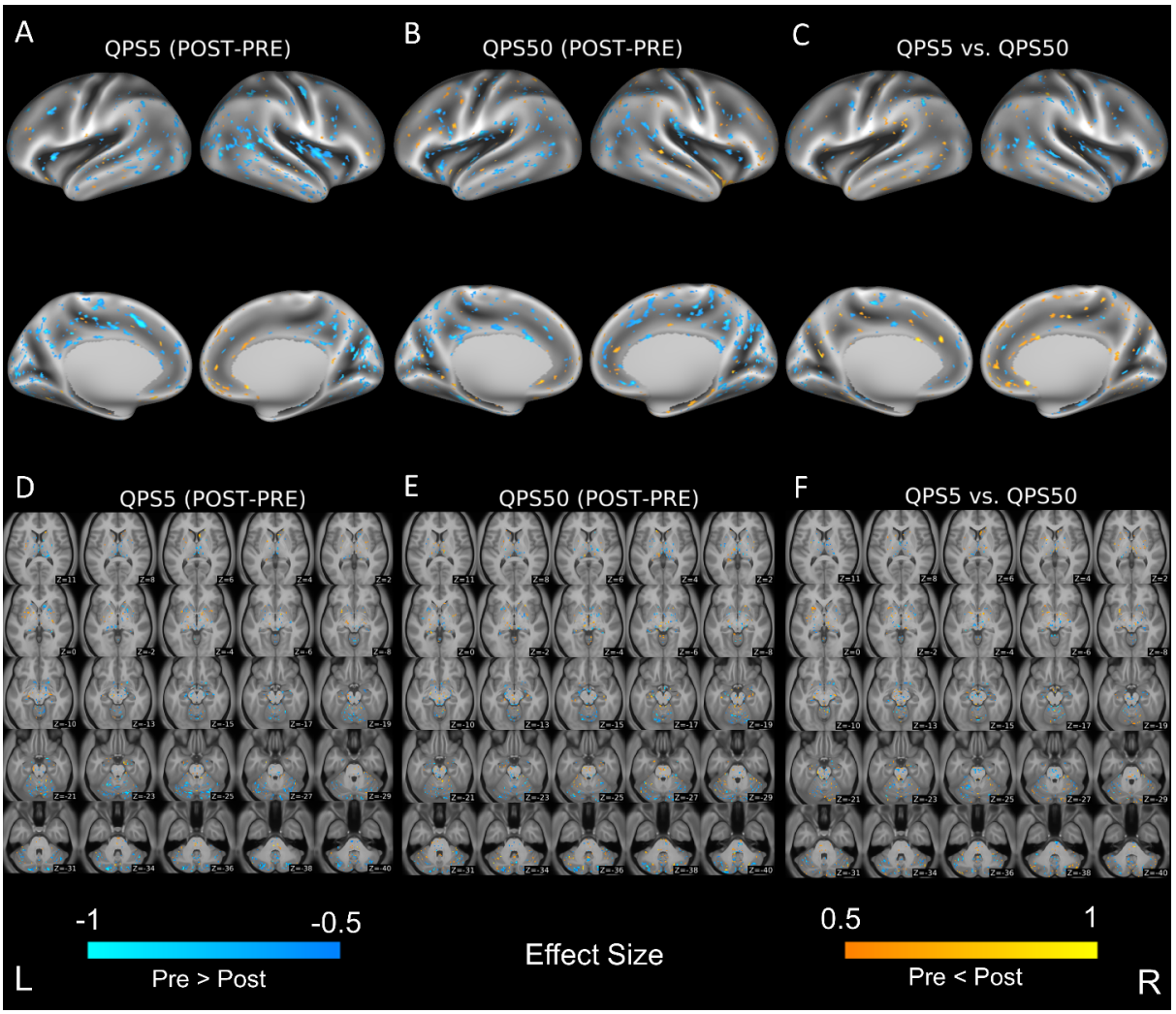

Figure 3.8 Differences in MD values of the cerebral cortex and subcortical regions between pre- and post-QPS in QPS5 (A and D) and QPS50 (B and E) conditions, and in changes of MD values across conditions (C and F). The upper panel (A–C) shows the result of surface-based analysis on the cerebral cortex, while the lower panel (D–F) shows that of voxel-based analysis in the subcortical regions. Areas in blue illustrate that the cohen's d of change in the value after QPS are smaller than -0.5, while those in yellow show that those values are higher than 0.5. Axial slices in (D–F) are shown in accordance with neurological conventions (left of the image is on the left of the brain) and are displayed in the MNI coordinates from z = 19 (left of the top) to z = -57 (right of the bottom).

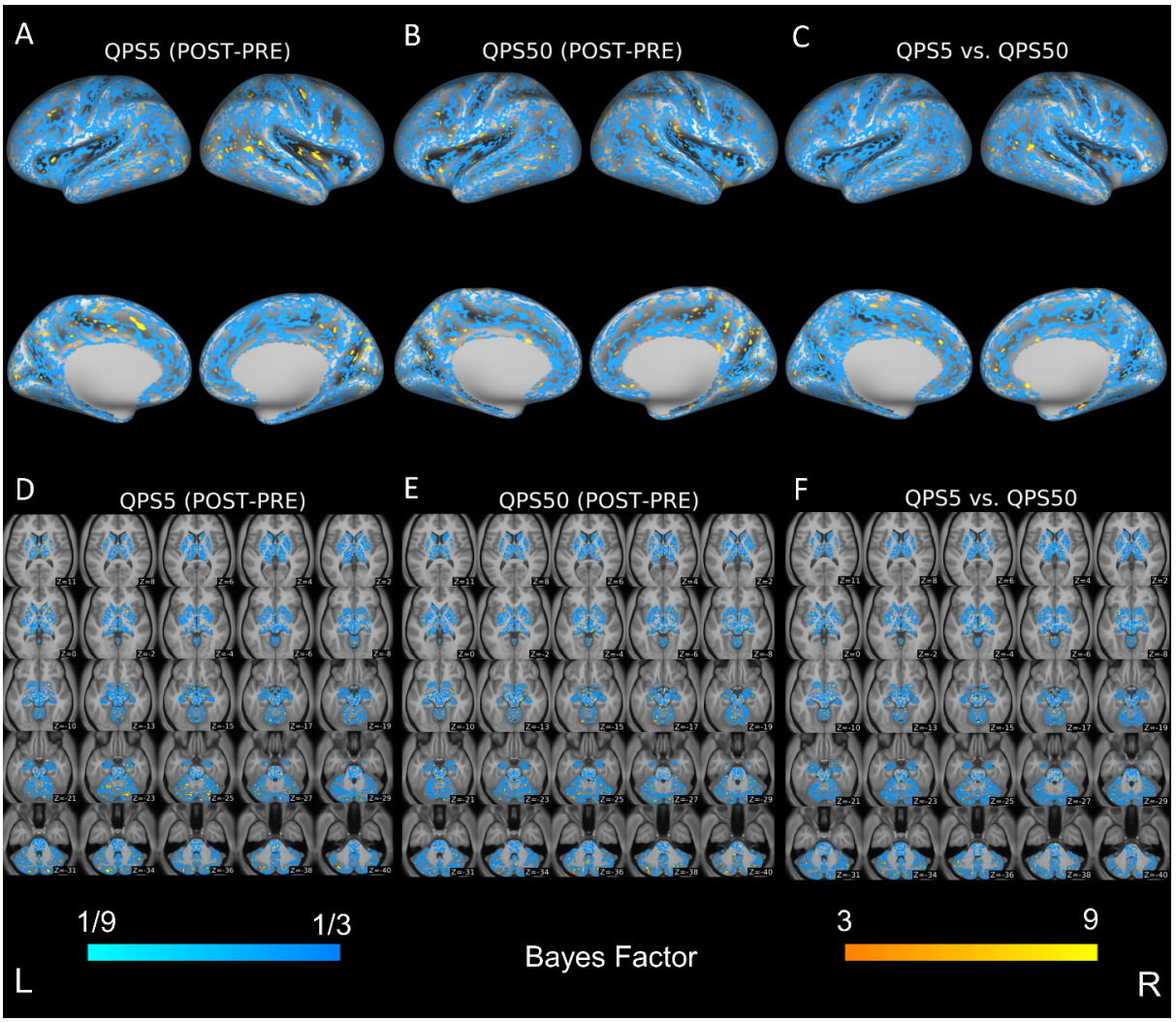

Figure 3.9 Differences in MD values of the cerebral cortex and subcortical regions between pre- and post-QPS in QPS5 (A and D) and QPS50 (B and E) conditions, and in changes of MD values across conditions (C and F). The upper panel (A–C) shows the result of surface-based analysis on the cerebral cortex, while the lower panel (D–F) shows that of voxel-based analysis in the subcortical regions. Areas in blue illustrate that the bayes factor was smaller than ⅓ in the comparison of the MD before and after QPS or the change of the MD across conditions (i.e., supports the hypothesis that the difference was zero). In contrast, those in yellow show those values are higher than 3. Axial slices in (D–F) are shown in accordance with neurological conventions (left of the image is on the left of the brain) and are displayed in the MNI coordinates from z = 19 (left of the top) to z = -57 (right of the bottom).

I then assessed the change of the microstructural property of the white matter after QPS5 and QPS50. TBSS revealed that there were no significant changes after QPS5 or QPS50 in the FA and MD values of the WM. Also, I observed no significant differences in the change of the FA and MD values in the white matter between the QPS5 and QPS50

conditions either (See Figure 3.10 and 3.11 for the effect size and bayes factor of FA, respectively, and Figure 3.12 and 3.13 for the effect size and bayes factor of MD comparing between pre and post of QPS5 or QPS50, respectively). Since TBSS only investigates the major region of the white matter (Smith et al., 2006), I additionally performed the whole-brain voxel-based analysis in the white matter. As a result, no significant difference was observed between the pre and post of QPS5 or QPS50 in the FA or MD values of the white matter or in the change of the FA or MD value in the white matter between the QPS5 and QPS50 conditions.

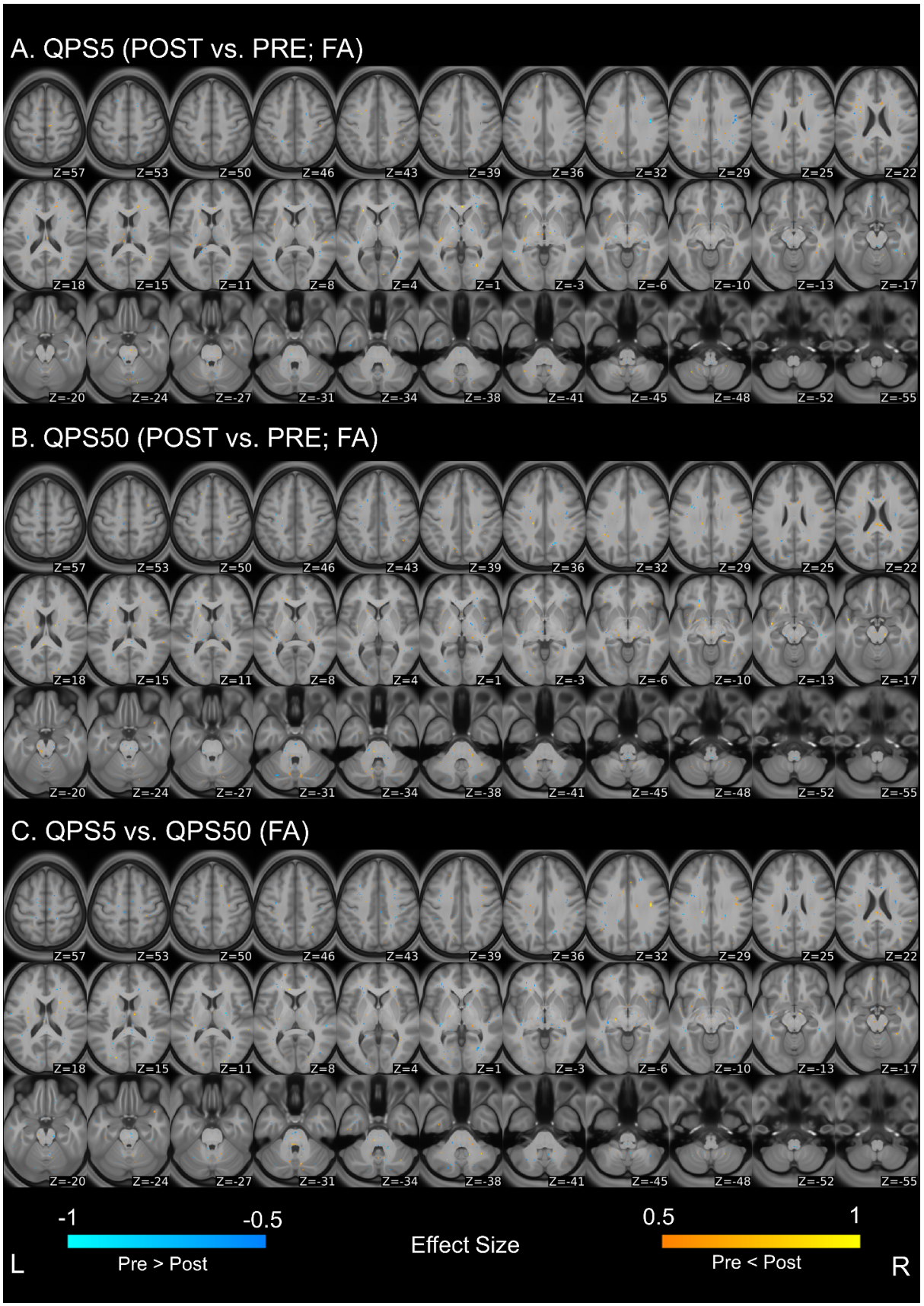

Figure 3.10 Differences in FA values of the white matter between pre- and post-QPS in QPS5 (A) and QPS50 (B) conditions, and in the change of FA values across conditions (C).

Areas in blue illustrate that the cohen's d of change in the value after QPS are smaller than -0.5, while those in yellow show that that statistical values are higher than 0.5. Axial slices are shown in accordance with neurological conventions (left of the image is on the left of the brain) and are displayed in the MNI coordinates from z = 57 (left of the top) to z = -55 (right of the bottom).

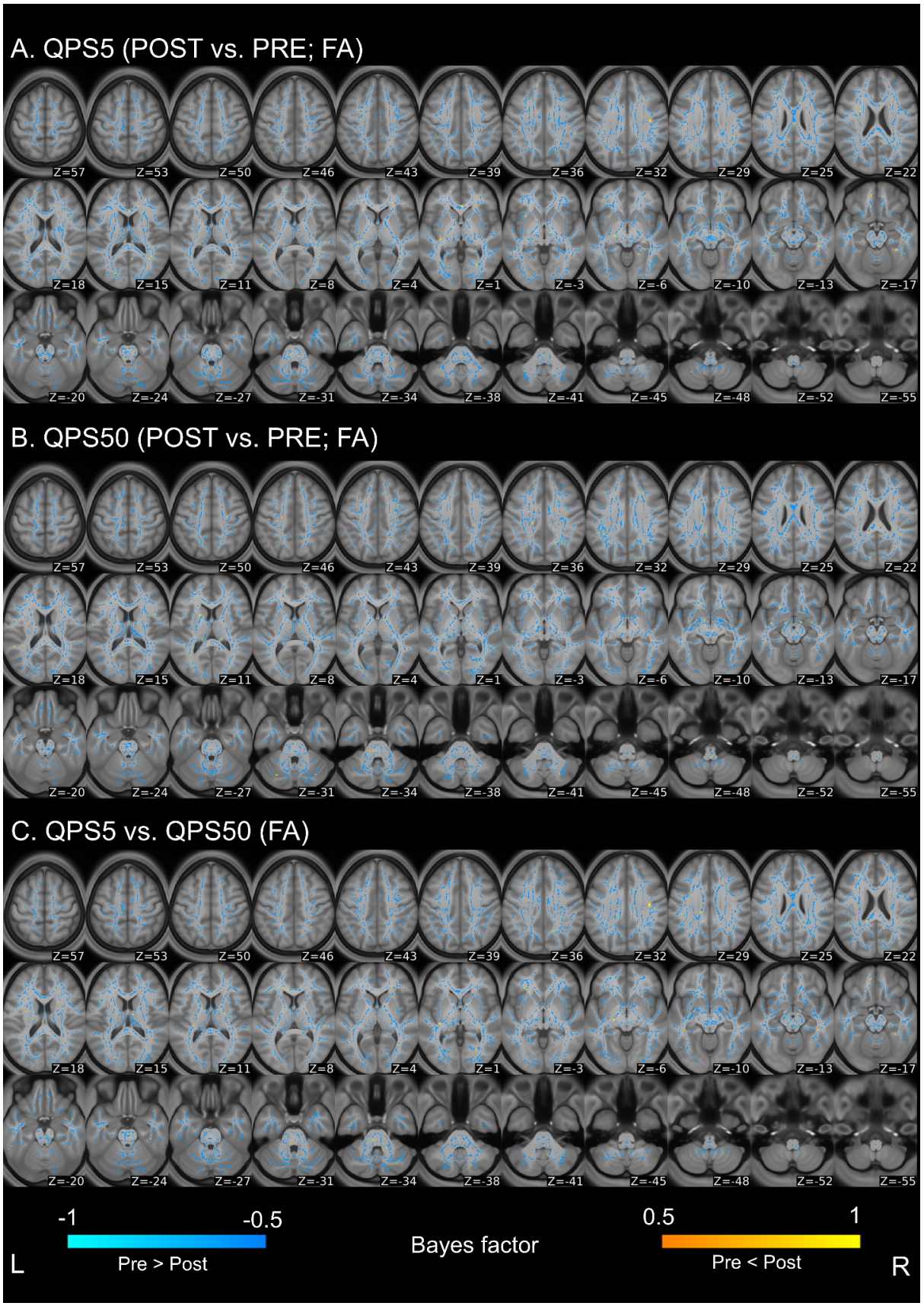

Figure 3.11 Differences in FA values of the white matter between pre- and post-QPS in QPS5 (A) and QPS50 (B) conditions, and in the change of FA values across conditions (C). Areas in blue illustrate that the bayes factor of change in the value after QPS are smaller than

1/3, while those in yellow show that those are higher than 3. Axial slices are shown in accordance with neurological conventions (left of the image is on the left of the brain) and are displayed in the MNI coordinates from z = 57 (left of the top) to z = -55 (right of the bottom).

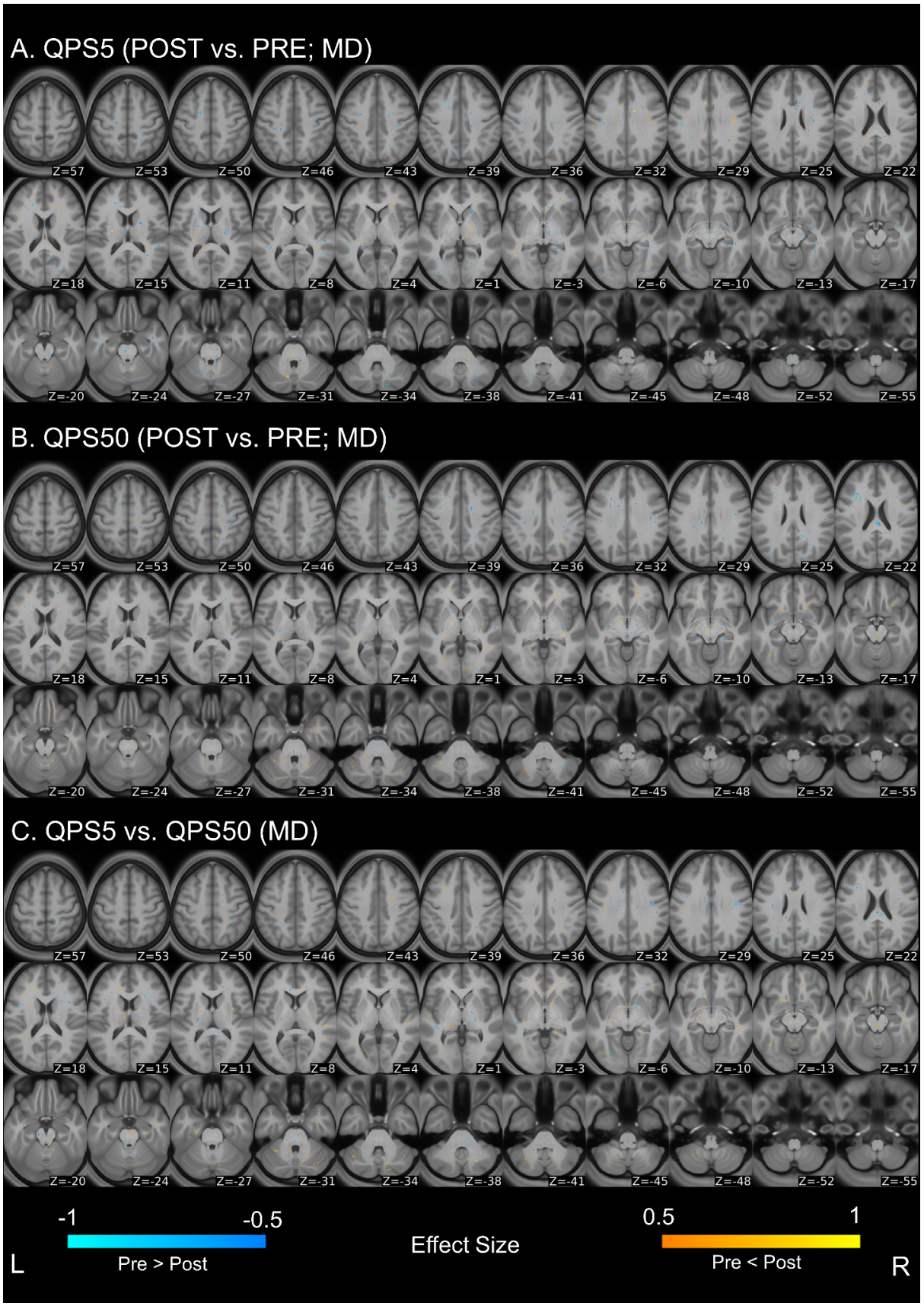

Figure 3.12 Differences in MD values of the white matter between pre- and post-QPS in QPS5 (A) and QPS50 (B) conditions, and in the change of MD values across conditions (C).

Areas in blue illustrate that the cohen's d of change in the value after QPS are smaller than -0.5, while those in yellow show that that statistical values are higher than 0.5. Axial slices are shown in accordance with neurological conventions (left of the image is on the left of the brain) and are displayed in the MNI coordinates from z = 57 (left of the top) to z = -55 (right of the bottom).

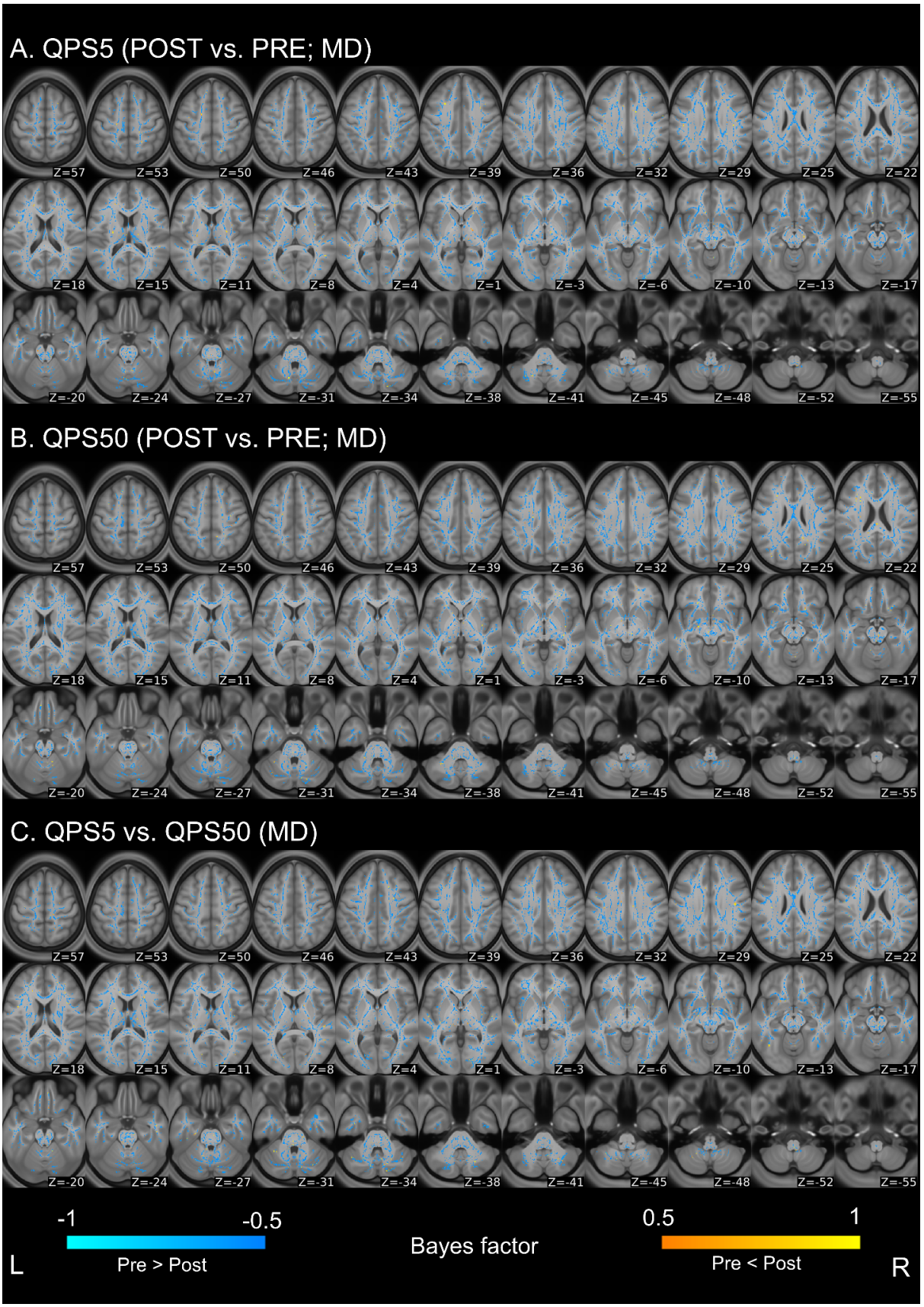

Figure 3.13 Differences in MD values of the white matter between pre- and post-QPS in QPS5 (A) and QPS50 (B) conditions, and in the change of MD values across conditions (C). Areas in blue illustrate that the bayes factor of change in the value after QPS are smaller than

1/3, while those in yellow show that those are higher than 3. Axial slices are shown in accordance with neurological conventions (left of the image is on the left of the brain) and are displayed in the MNI coordinates from z = 57 (left of the top) to z = -55 (right of the bottom).

3.4.2 The relationship between the change of the functional connectivity on the stimulated region and that of the microstructural property of the brain after quadri-pulse stimulation

To investigate the correlations between functional and microstructural change of the brain after QPS, I first evaluated the functional change after QPS5 or QPS50 by comparing the FC of the left M1 between the pre and post of QPS5 or QPS50. After QPS5, the FC of the left M1 was significantly decreased in the right dorso-medial prefrontal cortex, ventral premotor cortex, precentral gyrus, and postcentral gyrus (Figure 3.14A), while it was significantly increased in the bilateral cerebellum (Figure 3.14C). In contrast, after QPS50, I found the significant decrease of the FC of the left M1 in the left supplementary motor area, left precentral gyrus, and bilateral postcentral gyrus (Figure 3.14B), whereas no significant alteration was observed in the FC between the left M1 and subcortical structures (Figure 3.14D). The FC between the left and right M1 was decreased after QPS5 ($t = -2.60$, $P = 0.020$), whereas that FC was not significantly modulated after QPS50 ($t = -1.23$, $P = 0.24$) (Figure 3.15). There were no significant differences among QPS5 and QPS50 conditions regarding the change of the FC between these two regions after QPS ($t = -0.80$, $P = 0.44$).

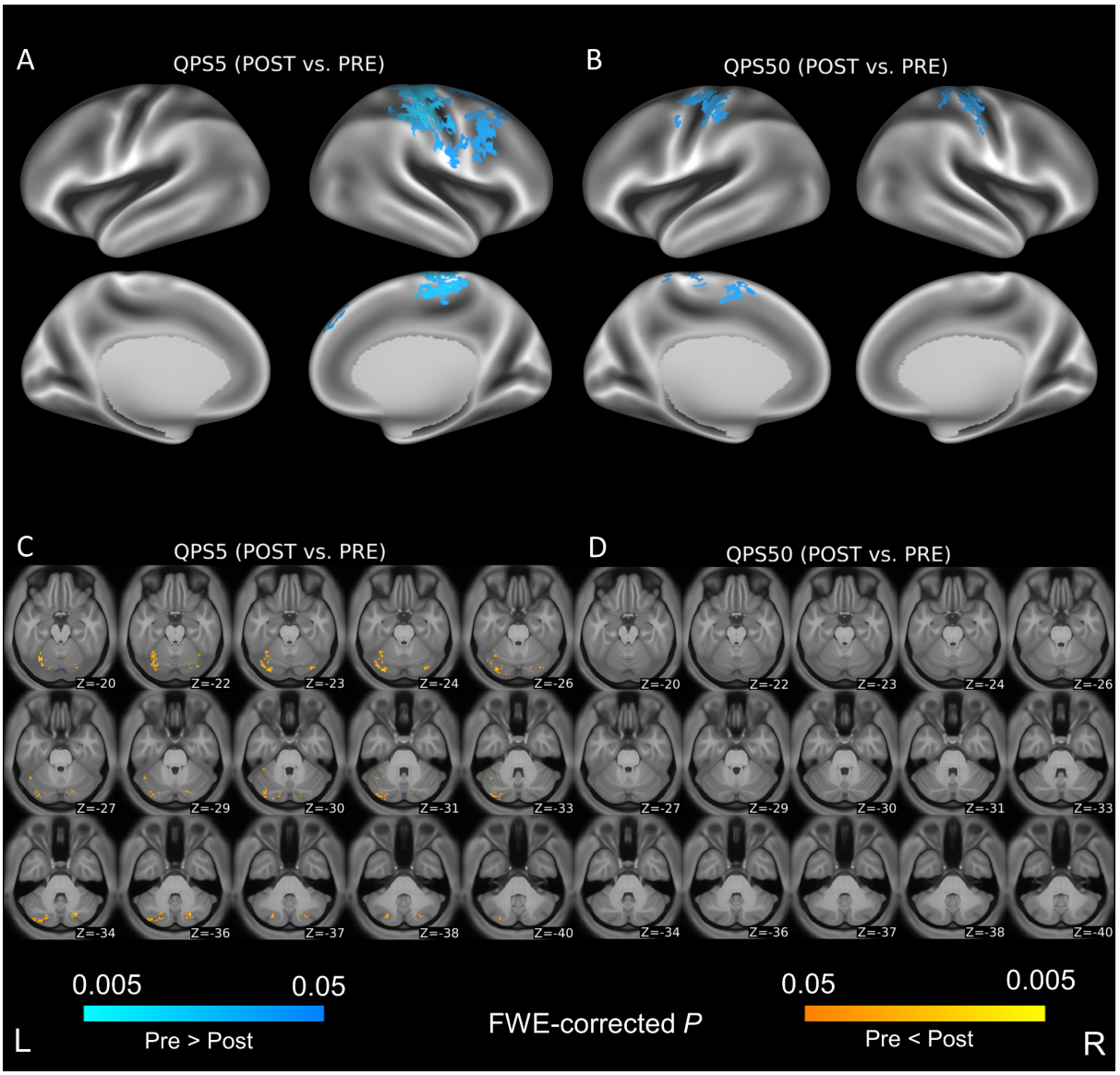

Figure 3.14 Differences in the functional connectivity (FC) of the left M1 (i.e, the stimulated region) between pre- and post-QPS in QPS5 (A and C) and QPS50 (B and D) conditions. (A) and (B) show the results of differences with surface-based analysis in the cerebral cortex, while (C) and (D) indicate those with voxel-based analysis in subcortical structures. Areas in blue show that the FC with the left M1 was significantly decreased after QPS, while areas in yellow indicate that that value was significantly increased after QPS. Axial slices are shown in accordance with neurological conventions (left of the image is on the left of the brain) and are displayed in the MNI coordinates from z = -20 (left of the top) to z = -40 (right of the bottom).

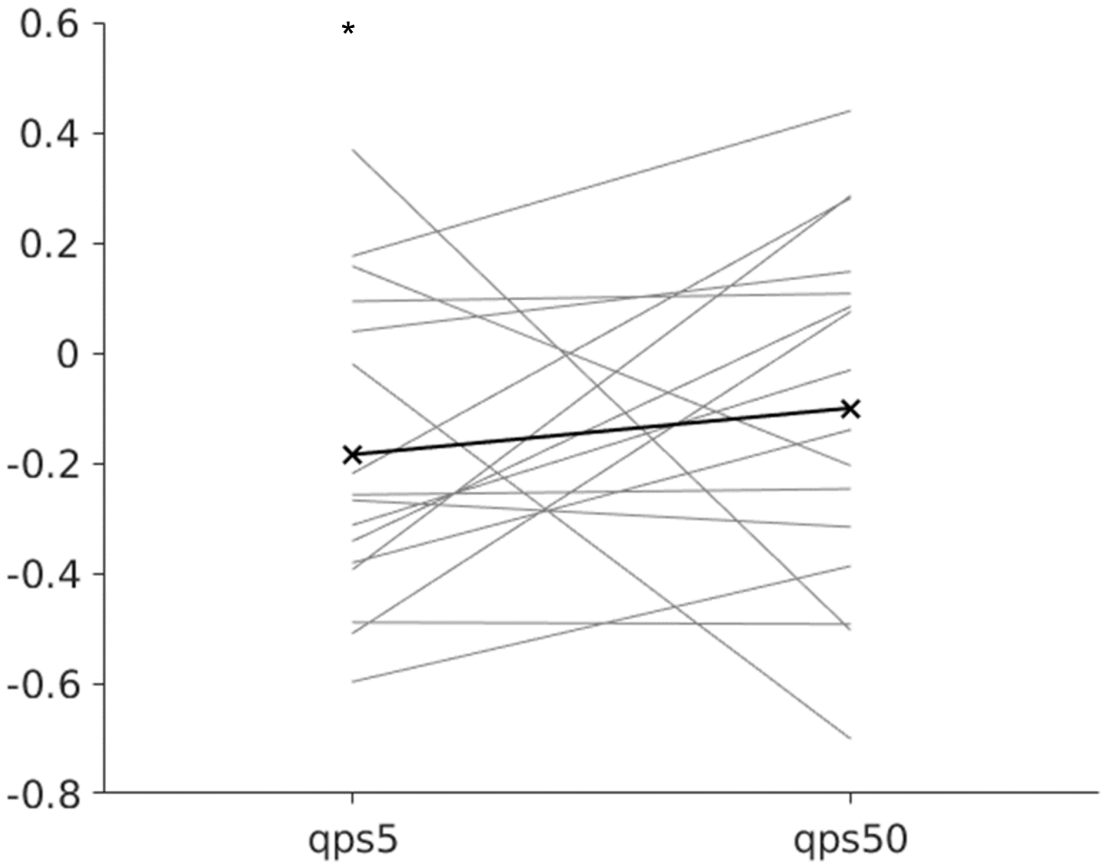

Figure 3.15 Changes in the functional connectivity (FC) between the left and right M1 after QPS. Thick black line with cross indicates the mean FC change across participants. The figure on the left denotes the change after QPS5, while that on the right denotes that after QPS50. The y-axis indicates the change in the FC after QPS. * shows the change was statistically significant ($P < 0.05$).

I then investigated the correlation between the change of the FA or MD value and the change of FC between the left and right M1 after QPS, which was significantly correlated with the after-effect of the stimulated region (i.e, MEP change) in the previous study (Watanabe et al., 2014). The regression analysis revealed that there were no significant correlations between the change of FA or MD values and the change of FC between the left

and right M1 either after QPS5 or QPS50. To confirm that the size of ROI does not change the result, I calculated Pearson's correlation coefficient between the change of FC defined by 5 mm radius and that by 2 mm radius or that by 8 mm radius in both QPS5 and QPS50 conditions. As a result, I found that all of the changes were significantly and positively correlated with each other, suggesting that the size of the ROI does not affect the change of FC between the left and right M1 (QPS5 [5 mm radius vs. 8 mm radius], rho = 0.94, $P < 0.001$; QPS5 [5 mm radius vs. 2 mm radius], rho = 0.97, $P < 0.001$; QPS50 [5 mm radius vs. 8 mm radius], rho = 0.94, $P < 0.001$; QPS50 [5 mm radius vs. 2 mm radius], rho = 0.92, $P < 0.001$). Additionally, I did not observe the significant correlation between the mean decrease of the MD value and the mean change of FC with the left M1 in the clusters of bilateral cerebellum whose MD values significantly decreased after QPS5 (rho = -0.21, $P = 0.43$) or QPS50 (rho = -0.35, $P = 0.18$).

3.4.3 Possible confounding factors both within and across the session

To detect the confounding factors affecting the change after QPS5 or QPS50 or the difference of the change between the QPS5 and QPS50 conditions, I compared the quantitative measurements of the image quality between the pre and post of the QPS-session and the change of these measurements between the QPS5 and QPS50 conditions. Regarding rsfMRI, Wilcoxson signed-rank tests revealed that there were no significant changes in the score of Stanford Sleepiness Scale (sleepiness) between the pre and post of the QPS session (QPS5, W = 65.50, $P = 0.41$; QPS50, W = 63.00, $P = 0.061$; Figure 3.16A). Though no significant change of the mean FD was found in the QPS5 condition (t = 1.24, $P = 0.23$, Figure 3.16B), there was a significant decrease in this measurement in the QPS50 condition (t = 2.69, $P = 0.017$, Figure 3.16B). No significant changes were found regarding the image quality of dMRI in either QPS5 (mean absolute motion, t = -0.99, $P = 0.34$, Figure 3.16C; mean relative motion, t = -0.52, $P = 0.61$, Figure 3.16D) or QPS50 (mean absolute motion, t = 0.51, $P =$

0.62, Figure 3.11C; mean relative motion, t = 0.78, *P* = 0.45, Figure 3.16D) conditions. I found no significant difference between the QPS5 and QP50 conditions in the change of all these measurements within the session either (Stanford Sleepiness Score, W = 49.50, *P* = 0.80, Figure 3.16A; mean framewise displacement, t = 0.99, *P* = 0.34, Figure 3.11B; mean absolute motion in dMRI, t = 1.23, *P* = 0.24, Figure 3.16C; mean relative motion in dMRI, t = 0.83, *P* = 0.42, Figure 3.16D).

Since the mean FD can be the confounding factor in the comparison of the FC on the stimulated regions, I additionally applied the analysis of covariance towards the FC on the left M1 setting the mean FD as a covariate of no interest (Figure 3.17). As a result, I found that, in the QPS5 condition, the FC of the left M1 was decreased in the right ventral premotor cortex, precentral gyrus, postcentral gyrus, and dorso-medial prefrontal cortex, while it was decreased in the QPS50 condition in the bilateral precentral gyrus, bilateral postcentral gyrus, bilateral supplementary motor area (Figure 3.17A). I also found that the FC of the left M1 was increased in the bilateral cerebellum (Figure 3.17B). No significant differences were found on the change of the FC on the left M1 between the QPS5 and QPS50 conditions. After regressing out the effect of mean FD, the FC of the left and right M1 was significantly decreased after QPS5 (t = -2.76, *P* = 0.015), while that FC was not significantly altered after QPS50 (t = -1.46, *P* = 0.17). I found no significant differences among QPS5 and QPS50 conditions in the change of FC between these two regions after QPS (t = -0.75, *P* = 0.47). I also confirmed that there were no significant correlations between the change of this FC and the change of FA or MD value after QPS5 or QPS50. All these results suggest that the mean FD did not severely affect the results related to the change of FC of left M1.

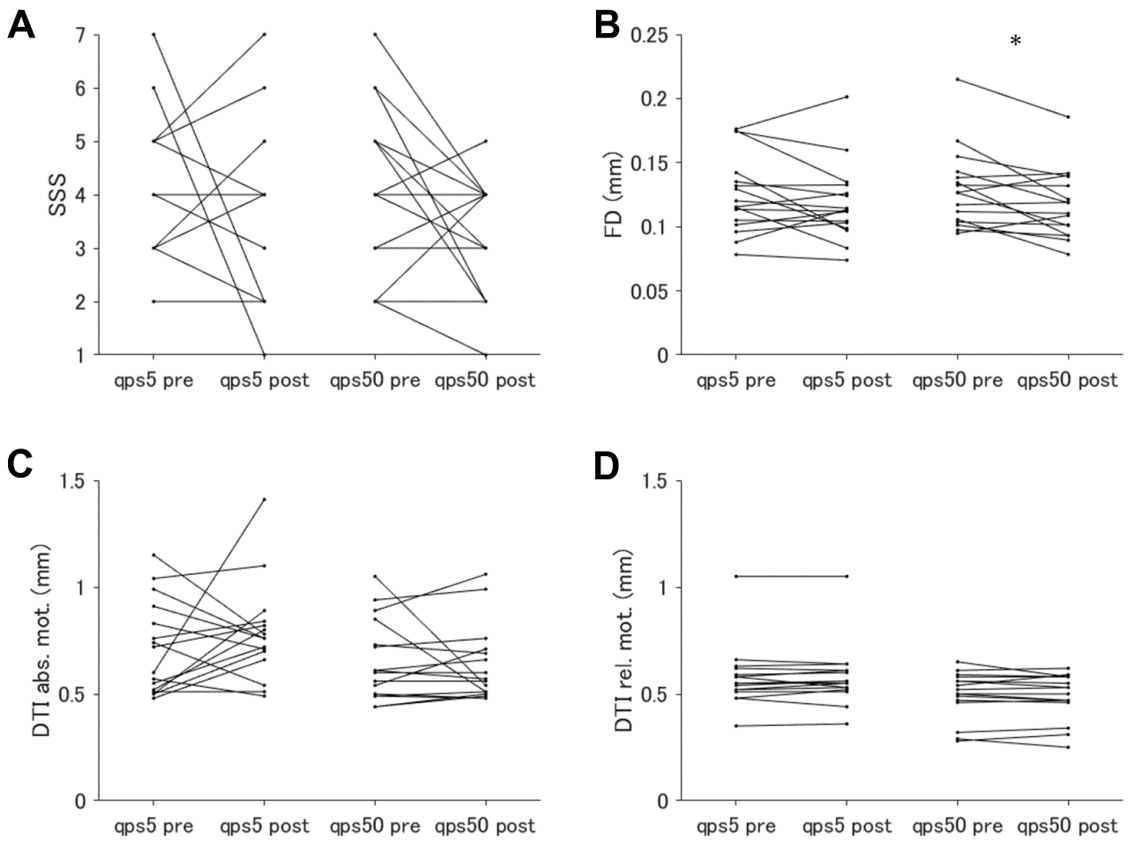

Figure 3.16 Comparison of the quantitative measurements on quality of resting-state fMRI (rsfMRI; A–B) and diffusion MRI (dMRI; C–D) measured pre- and post-QPS in QPS5 and QPS50 conditions. (A) and (B) show stanford sleepiness scale (SSS) and mean framewise displacement (FD; mm), respectively, while (C) and (D) illustrate mean absolute and relative motion (mm) during dMRI scan. * indicates that the comparison was significantly different according to the paired t-test.

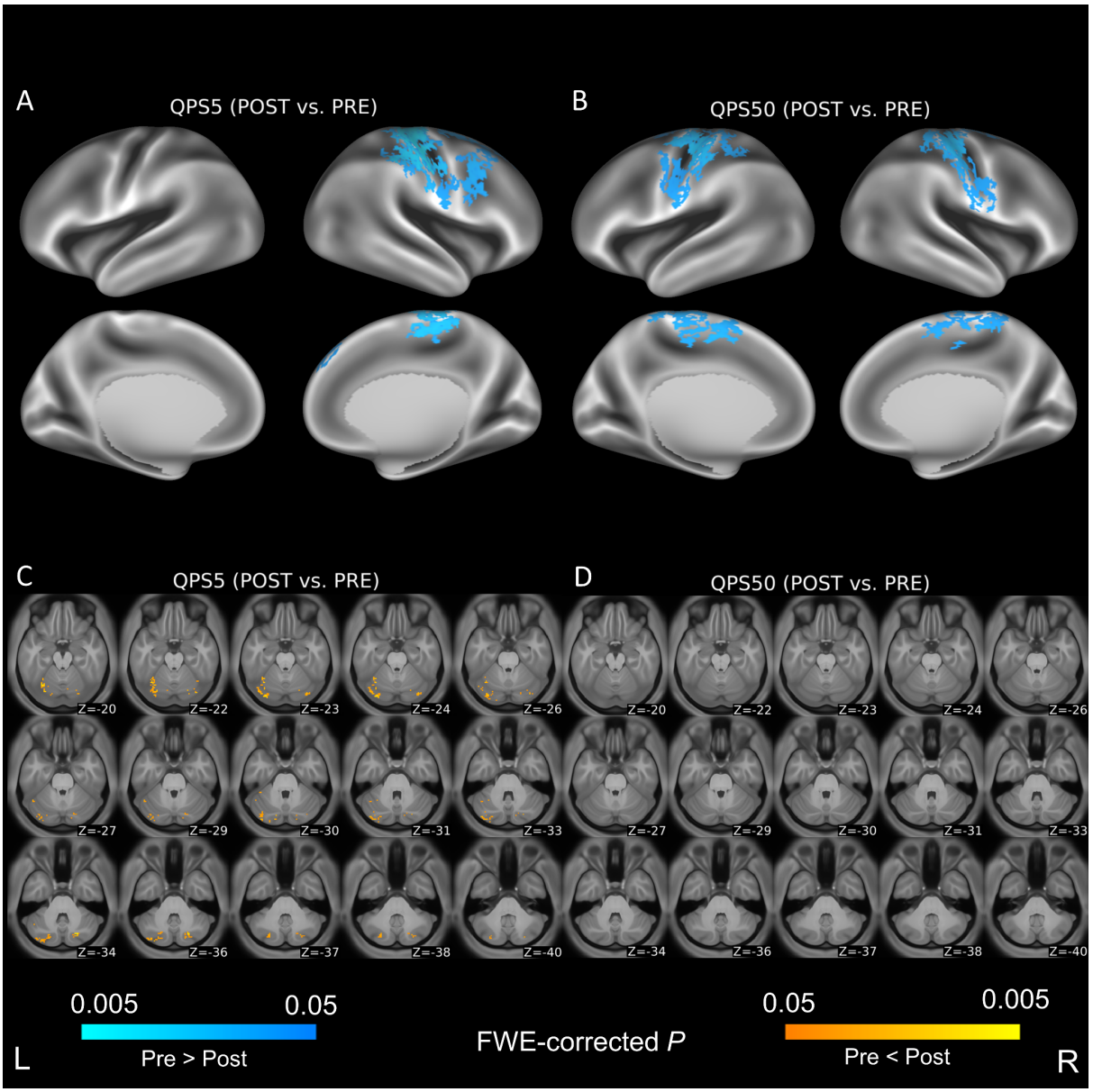

Figure 3.17 Differences in the functional connectivity (FC) of the left M1 (i.e, the stimulated region) between pre- and post-QPS in QPS5 (A and C) and QPS50 (B and D) conditions, setting the mean framewise displacement as a covariate of no-interest. (A) and (B) show the results of differences with surface-based analysis in the cerebral cortex, while (C) and (D) indicate those with voxel-based analysis in subcortical structures. Areas in blue show that the FC with the left M1 was significantly decreased after QPS, while areas in yellow indicate that that value was significantly increased after QPS. Axial slices are shown in accordance with neurological conventions (left of the image is on the left of the brain) and are displayed in the MNI coordinates from z = -20 (left of the top) to z = -40 (right of the bottom).

3.5 Discussion

Here, changes in the microstructural properties of the cerebral cortex, subcortical regions, and WM of the human brain after QPS5 or QPS50 over the left M1 were examined. As a result, no significant changes were found in the FA or MD values either after QPS5 or QPS50 in most regions other than the significant decrease in the MD value in the bilateral cerebellum after both QPS5 and QPS50. No significant correlations were observed between the change in microstructural properties and that of FC between the left and right M1 (the after-effect of QPS) in either the QPS5 or the QPS50 condition.

3.5.1 No significant change in the microstructural property of the gray matter in the cerebral cortex after QPS

No significant change was detected in the FA or MD values of the cerebral cortex after either QPS5 or QPS50. No significant correlation was observed between the change in these values and the functional changes in QPS, which was measured by the change in FC between the left and right M1. Given that FA and MD values are sensitive biomarkers for changes in the microstructural properties of both neurons (Basser et al., 1994; Zhong et al., 1993) and glial cells (Debacker et al., 2020; Sagi et al., 2012; Yi et al., 2020) in the brain, the current results suggest that the microstructural properties in the cerebral cortex were not modulated immediately after both the excitatory and inhibitory protocols of QPS. My results are consistent with previous studies reporting that the microstructural properties were not significantly changed after either the excitatory (Niehaus et al., 2000) or inhibitory (Duning et al., 2004) protocols of conventional rTMS. Regarding the process of neuroplastic changes in pyramidal neurons, microstructural changes, such as changes in the number of dendritic spines (Engert and Bonhoeffer, 1999), require protein synthesis and multiple kinase activation to modulate gene activation. This means that more time is required for

microstructural changes to occur than for functional changes (Ugawa, 2012). Therefore, QPS may not induce microstructural changes immediately after the stimulation.

In contrast, two previous studies reported microstructural alterations in the human brain immediately after rTMS. While one study observed that MD values were significantly decreased in the stimulated region (Mottaghy et al., 2003), another study reported that these values were significantly increased in both the stimulated and unstimulated regions (Abe et al., 2014) after 1 Hz rTMS. These differences might be partially explained by differences in the rTMS protocols. In previous studies, the stimulus intensity was 90% RMT (Abe et al., 2014; Mottaghy et al., 2003), which was stronger than that used in the current study (90% AMT). Moreover, the neural mechanisms evoked by QPS and 1 Hz rTMS are different. While short-interval intracortical inhibition, which measures the function of inhibitory interneurons (Kujirai et al., 2006), is modulated by 1 Hz rTMS (Chen et al., 2018), it is not modulated by QPS (Hamada et al., 2008). Animal studies confirmed that the number of calbindin-expressing inhibitory interneurons decreased after 1 Hz rTMS (Benali et al., 2011), implying that the change in the microstructural properties induced by the 1 Hz rTMS might reflect the microstructural changes in inhibitory interneurons. Therefore, the lack of significant microstructural alterations in the cerebral cortex in the current study may be specific to QPS.

The MD values of the bilateral cerebellum decreased after both QPS5 and QPS50, and the change in the MD value was not significantly different across the conditions. The cerebellum is important for shaping the internal model of action for precise movement (Buckner et al., 2013). Moreover, one study reported that patients with cerebellar degeneration failed to perform a reaching task in a new environment, suggesting that the cerebellum also plays a critical role in adapting to new environments during movement (Hanajima et al., 2015). Together with the results of the current study, these results might

imply that the microstructural properties of the bilateral cerebellum were changed to adapt to the change in the brain activity of the left M1. Nevertheless, these results must be interpreted with caution because voxel-based DTI analysis has been reported to be susceptible to registration errors (Jones et al., 2005). Furthermore, no significant correlations were found between these changes and the functional change after QPS in both QPS5 and QPS50 conditions, and no significant differences in the changes in these properties between QPS5 and QPS50 conditions, implying that the change in the microstructural properties in this study might be unspecific to the after-effect of QPS. Future animal studies or MRI studies with a high spatial resolution are required to verify whether these changes actually occur.

3.5.2 No significant change in the microstructural property of the white matter after QPS

No significant alterations were found in the FA or MD values of white matter after QPS5 or QPS50. This result is consistent with a previous study showing that white matter volume was not significantly modulated immediately after continuous theta-burst stimulation, which is an inhibitory rTMS protocol, to the temporal area (Jung and Lambon Ralph, 2021). In contrast, several studies have revealed remodeling of the microstructural properties of white matter 24 h after neuromodulation interventions, such as neurofeedback training (Sampaio-Baptista et al., 2021) and cortico-cortico paired associative stimulation (Lazari et al., 2022). These differences might be due to the differences in time evaluated after the intervention because several animal studies have shown that oligodendrogenesis or myelination can be observed more than one hour after stimulation (Sampaio-Baptista and Johansen-Berg, 2017). Since one study reported that oligodendrogenesis can occur several hours after repetitive neural activation (Gibson et al., 2014) and the after-effect of QPS lasts for more than several hours (Hamada et al., 2008), future studies are required to investigate the microstructural changes several hours after QPS.

3.5.3 Limitation

This study had several limitations. First, the microstructural properties were assessed using only the DTI-derived metrics. Although these metrics are useful in exploring changes in the microstructural properties of the human brain (Basser et al., 1994; Debacker et al., 2020; Komaki et al., 2020; Sagi et al., 2012), a previous study detected microstructural alterations after neuromodulation interventions using magnetization transfer imaging (Lazari et al., 2022), which is a sensitive biomarker of myelin. Another study implied that the microstructural metrics derived from different modalities might reflect different types of microstructural characteristics (Lipp et al., 2019). Therefore, I cannot rule out the possibility that microstructural indicators obtained with modalities other than DTI might detect the remodeling of the microstructure after QPS.

Another possible limitation of this study is that due to time constraints, the after-effect of QPS was assessed with the change in FC between the left and right M1 (Beynel et al., 2020). MEP, a more typical measure of the after-effect of TMS (Kimura et al., 2022), may have more accurately revealed the association between microstructural and functional changes after QPS. In the current study, the FC between the left and right M1 decreased after QPS5 but was not significantly modulated after QPS50. These results partially contradict the previous study showing that the FC between these two regions decreased after QPS5, whereas it increased after QPS50 (Watanabe et al., 2014). These differences could be explained by the time of measurement after QPS: immediately after QPS in the current study and 30 minutes after QPS in the study by Watanabe et al. (Watanabe et al., 2014). Given that bidirectional changes in MEP amplitude after QPS over the left M1 (increase after QPS5 and moderate decrease and QPS50) were clearly observed 30 min after QPS (Kimura et al., 2022), the changes in FC between the left and right M1 might also be observed more clearly 30 min after QPS than immediately after QPS.

Another interesting future direction is the change in astrocytes or microglial cells induced by rTMS. Several animal studies have suggested that the activity of glial cells is modulated by rTMS (Cullen and Young, 2016). Because these functional properties can also be noninvasively evaluated in the human brain using PET (Maeda et al., 2004), it would be interesting to explore the correlations between functional changes in glial cells and microstructural changes in the human brain after QPS.

3.5.4 Conclusion

There were no significant microstructural changes in the human brain immediately after QPS5 or QPS50. Future studies are needed to examine microstructural changes at different time points after the intervention and to assess these changes using different modalities.

Chapter 4. General discussion and conclusion

4.1 Integrative Summary

In this thesis, I first overviewed the principles of rTMS and neuroimaging methods to probe microstructural property in the human brain compared to those to assess its functional property. Regarding the studies of this thesis, I investigated the relationship between the microstructural property of the human brain and the after-effect of rTMS. In the first study (Chapter 2), I investigated whether the microstructural property of the human brain can predict the magnitude of the after-effect of iTBS. As a result, I found the microstructural property of the white matter, assessed with FA, was correlated with the early phase of the after-effect of iTBS, while that of the gray matter was associated with the late phase of that after-effect. In the second study (Chapter 3), I examined whether QPS in turn induces the microstructural remodeling right after the stimulation. I found no significant differences in the microstructural property of the human brain either by the excitatory or inhibitory protocol of QPS. The results obtained from these studies will be important in clarifying the after-effect of rTMS in the whole brain.

4.2 Diffusion MRI as an indicator for microstructural properties

In this study, I mainly assessed the microstructural property of the human brain with DTI-derived metrics. There are other microstructural measurements that can be calculated from diffusion MRI and other modalities of MRI, such as NODDI (Fukutomi et al., 2018; Zhang et al., 2012), Free Water Imaging (Hoy et al., 2014), Quantitative Susceptibility Mapping (Vinayagamani et al., 2021), and Myelin Water Imaging (Uddin et al., 2019). Nevertheless, DTI has the advantage for the relatively short required scanning time (5–10 min) compared to other methods, which would be useful in predicting the after-effect of

rTMS for clinical applications and assessing the transient change of the microstructures. Therefore, DTI will be of great value both in neuroscientific and clinical studies.

4.3 Potentiality of diffusion MRI as a predictive indicator of the rTMS after-effect

Predicting the efficacy of iTBS is crucial in deciding the treatment options in treating the neurological or psychiatric patients with rTMS. It has been over several years since iTBS was FDA-approved for treating depression (Blumberger et al., 2018). Since then, alternative protocols for TBS have been proposed, such as accelerated TBS (Chen et al., 2021; Cole et al., 2022) and high density TBS (Meng et al., 2022). Besides these protocols, the after-effect of QPS is stronger and more robust than that of TBS (Tiksnadi et al., 2020) and the pre-treatment with d-cycloseline might boost the after-effect of TBS (Brown et al., 2020; Cole et al., 2021). Nevertheless, the required stimulation length of the original TBS is the shortest and the administration of d-cycloserine is, for now, not recommended for the patients with renal failure, alcoholism or depression. Therefore, future studies with larger sample sizes will be required to clarify whether DTI can precisely propose the treatment option of rTMS with machine learning.

It would be also appealing, in psychological experiments, to select the population of each study from DTI measurements to ensure the robust after-effect of rTMS. However, this selection must be performed with caution because that selection can bias the result of the study. Future neuroimaging studies with large populations (Glasser et al., 2016b; Koike et al., 2021) will clarify the association between the microstructural properties of each area in the human brain and psychophysical characteristics, and the selection of the population will be cautiously performed with the microstructural property of the regions unrelated to the

examined psychophysical characteristics. Taken together, predicting the after-effect of rTMS will be important in both neuroscientific and clinical research.

4.4 Potentiality of cortico-cortico paired associative stimulation as a neuromodulation tool to modulate the microstructures

Though I could not observe the difference in the microstructural property right after QPS, one study showed that this property can be modulated 24 hr after cortico-cortico paired associative stimulation, which is one of rTMS (Lazari et al., 2022). Replication crisis has been gaining attention in neuroimaging research over the past few years (Botvinik-Nezer et al., 2020; Marek et al., 2022), and leveraging neuromodulation tools to explore the causal relationship between the neuroimaging characteristics and behavior is one of the proposed ways to exclude the false-positives obtained from the studies investigating the correlations between these characteristics and behavior (Rosenberg and Finn, 2022). It would be attractive to modulate the microstructural properties in the human brain also by rTMS to examine the causal relationship between these properties and behavior, and this might be achieved by investigating the effect 24 hr after rTMS.

4.5 Concluding remarks

Recent advancements in neuroimaging techniques have allowed quantitative and noninvasive measurements of the microstructure properties of the human brain. In this thesis, by utilizing DTI and rTMS, I demonstrated that the microstructural property in the human brain and the magnitude of the after-effect of rTMS had tight relationship, but that QPS did not, in turn, induce significant microstructural change immediately after QPS. With other modalities, these combinatorial approaches will further clarify the relationship between the structure and the after-effect of rTMS or the mechanisms occurring after rTMS in the whole brain.

Chapter 5. References

Abe, M., Fukuyama, H., Mima, T., 2014. Water diffusion reveals networks that modulate multiregional morphological plasticity after repetitive brain stimulation. Proc. Natl. Acad. Sci. U. S. A. 111, 4608–4613. https://doi.org/10.1073/pnas.1320223111

Aggarwal, M., Nauen, D.W., Troncoso, J.C., Mori, S., 2015. Probing region-specific microstructure of human cortical areas using high angular and spatial resolution diffusion MRI. Neuroimage 105, 198–207. https://doi.org/10.1016/j.neuroimage.2014.10.053

Ah Sen, C.B., Fassett, H.J., El-Sayes, J., Turco, C.V., Hameer, M.M., Nelson, A.J., 2017. Active and resting motor threshold are efficiently obtained with adaptive threshold hunting. PLoS One 12, 1–9. https://doi.org/10.1371/journal.pone.0186007

Alonso-Ortiz, E., Levesque, I.R., Pike, G.B., 2015. MRI-based myelin water imaging: A technical review. Magn. Reson. Med. 73, 70–81. https://doi.org/10.1002/mrm.25198

Andersson, J.L.R., Graham, M.S., Zsoldos, E., Sotiropoulos, S.N., 2016. Incorporating outlier detection and replacement into a non-parametric framework for movement and distortion correction of diffusion MR images. Neuroimage 141, 556–572. https://doi.org/10.1016/j.neuroimage.2016.06.058

Andersson, J.L.R., Skare, S., Ashburner, J., 2003. How to correct susceptibility distortions in spin-echo echo-planar images: application to diffusion tensor imaging. Neuroimage 20, 870–888. https://doi.org/10.1016/S1053-8119(03)00336-7

Andersson, J.L.R., Sotiropoulos, S.N., 2016. An integrated approach to correction for off-resonance effects and subject movement in diffusion MR imaging. Neuroimage 125, 1063–1078. https://doi.org/10.1016/j.neuroimage.2015.10.019

Arai, N., Okabe, S., Furubayashi, T., Mochizuki, H., Iwata, N.K., Hanajima, R., Terao, Y., Ugawa, Y., 2007. Differences in after-effect between monophasic and biphasic high-frequency rTMS of the human motor cortex. Clin. Neurophysiol. 118, 2227–2233. https://doi.org/10.1016/j.clinph.2007.07.006

Arshad, M., Stanley, J.A., Raz, N., 2017. Test-retest reliability and concurrent validity of in vivo myelin content indices: Myelin water fraction and calibrated T1 w/T2 w image ratio. Hum. Brain Mapp. 38, 1780–1790. https://doi.org/10.1002/hbm.23481

Assaf, Y., Basser, P.J., 2005. Composite hindered and restricted model of diffusion (CHARMED) MR imaging of the human brain. Neuroimage 27, 48–58. https://doi.org/10.1016/j.neuroimage.2005.03.042

Ball, G., Srinivasan, L., Aljabar, P., Counsell, S.J., Durighel, G., Hajnal, J.V., Rutherford, M.A., Edwards, A.D., 2013. Development of cortical microstructure in the preterm human brain. Proc. Natl. Acad. Sci. U. S. A. 110, 9541–9546. https://doi.org/10.1073/pnas.1301652110

Basser, P.J., Mattiello, J., LeBihan, D., 1994. MR diffusion tensor spectroscopy and imaging. Biophys. J. 66, 259–267. https://doi.org/10.1016/S0006-3495(94)80775-1

Bäumer, T., Schippling, S., Kroeger, J., Zittel, S., Koch, G., Thomalla, G., Rothwell, J.C., Siebner, H.R., Orth, M., Münchau, A., 2009. Inhibitory and facilitatory connectivity from ventral premotor to primary motor cortex in healthy humans at rest – A bifocal TMS study. Clinical Neurophysiology. https://doi.org/10.1016/j.clinph.2009.07.035

Beaulieu, C., 2002. The basis of anisotropic water diffusion in the nervous system - a technical review. NMR Biomed. 15, 435–455. https://doi.org/10.1002/nbm.782

Benali, A., Trippe, J., Weiler, E., Mix, A., Petrasch-Parwez, E., Girzalsky, W., Eysel, U.T., Erdmann, R., Funke, K., 2011. Theta-burst transcranial magnetic stimulation alters cortical inhibition. J. Neurosci. 31, 1193–1203.

https://doi.org/10.1523/JNEUROSCI.1379-10.2011
Bergel, A., Tiran, E., Deffieux, T., Demené, C., Tanter, M., Cohen, I., 2020. Adaptive modulation of brain hemodynamics across stereotyped running episodes. Nat. Commun. 11, 6193. https://doi.org/10.1038/s41467-020-19948-7
Bestmann, S., Krakauer, J.W., 2015. The uses and interpretations of the motor-evoked potential for understanding behaviour. Exp. Brain Res. 233, 679–689. https://doi.org/10.1007/s00221-014-4183-7
Betz, W.J., 1970. Depression of transmitter release at the neuromuscular junction of the frog. J. Physiol. 206, 629–644. https://doi.org/10.1113/jphysiol.1970.sp009034
Beynel, L., Powers, J.P., Appelbaum, L.G., 2020. Effects of repetitive transcranial magnetic stimulation on resting-state connectivity: A systematic review. Neuroimage 211, 116596. https://doi.org/10.1016/j.neuroimage.2020.116596
Bijsterbosch, J., Smith, S.M., Beckmann, C., 2017. An Introduction to Resting State FMRI Functional Connectivity. Oxford University Press.
Bloem, B.R., Okun, M.S., Klein, C., 2021. Parkinson's disease. Lancet 397, 2284–2303. https://doi.org/10.1016/S0140-6736(21)00218-X
Blumberger, D.M., Vila-Rodriguez, F., Thorpe, K.E., Feffer, K., Noda, Y., Giacobbe, P., Knyahnytska, Y., Kennedy, S.H., Lam, R.W., Daskalakis, Z.J., Downar, J., 2018. Effectiveness of theta burst versus high-frequency repetitive transcranial magnetic stimulation in patients with depression (THREE-D): a randomised non-inferiority trial. Lancet 391, 1683–1692. https://doi.org/10.1016/S0140-6736(18)30295-2
Boecker, M., Buecheler, M.M., Schroeter, M.L., Gauggel, S., 2007. Prefrontal brain activation during stop-signal response inhibition: an event-related functional near-infrared spectroscopy study. Behav. Brain Res. 176, 259–266. https://doi.org/10.1016/j.bbr.2006.10.009
Botvinik-Nezer, R., Holzmeister, F., Camerer, C.F., Dreber, A., Huber, J., Johannesson, M., Kirchler, M., Iwanir, R., Mumford, J.A., Adcock, R.A., Avesani, P., Baczkowski, B.M., Bajracharya, A., Bakst, L., Ball, S., Barilari, M., Bault, N., Beaton, D., Beitner, J., Benoit, R.G., Berkers, R.M.W.J., Bhanji, J.P., Biswal, B.B., Bobadilla-Suarez, S., Bortolini, T., Bottenhorn, K.L., Bowring, A., Braem, S., Brooks, H.R., Brudner, E.G., Calderon, C.B., Camilleri, J.A., Castrellon, J.J., Cecchetti, L., Cieslik, E.C., Cole, Z.J., Collignon, O., Cox, R.W., Cunningham, W.A., Czoschke, S., Dadi, K., Davis, C.P., Luca, A.D., Delgado, M.R., Demetriou, L., Dennison, J.B., Di, X., Dickie, E.W., Dobryakova, E., Donnat, C.L., Dukart, J., Duncan, N.W., Durnez, J., Eed, A., Eickhoff, S.B., Erhart, A., Fontanesi, L., Fricke, G.M., Fu, S., Galván, A., Gau, R., Genon, S., Glatard, T., Glerean, E., Goeman, J.J., Golowin, S.A.E., González-García, C., Gorgolewski, K.J., Grady, C.L., Green, M.A., Guassi Moreira, J.F., Guest, O., Hakimi, S., Hamilton, J.P., Hancock, R., Handjaras, G., Harry, B.B., Hawco, C., Herholz, P., Herman, G., Heunis, S., Hoffstaedter, F., Hogeveen, J., Holmes, S., Hu, C.-P., Huettel, S.A., Hughes, M.E., Iacovella, V., Iordan, A.D., Isager, P.M., Isik, A.I., Jahn, A., Johnson, M.R., Johnstone, T., Joseph, M.J.E., Juliano, A.C., Kable, J.W., Kassinopoulos, M., Koba, C., Kong, X.-Z., Koscik, T.R., Kucukboyaci, N.E., Kuhl, B.A., Kupek, S., Laird, A.R., Lamm, C., Langner, R., Lauharatanahirun, N., Lee, H., Lee, S., Leemans, A., Leo, A., Lesage, E., Li, F., Li, M.Y.C., Lim, P.C., Lintz, E.N., Liphardt, S.W., Losecaat Vermeer, A.B., Love, B.C., Mack, M.L., Malpica, N., Marins, T., Maumet, C., McDonald, K., McGuire, J.T., Melero, H., Méndez Leal, A.S., Meyer, B., Meyer, K.N., Mihai, G., Mitsis, G.D., Moll, J., Nielson, D.M., Nilsonne, G., Notter, M.P., Olivetti, E., Onicas, A.I., Papale, P., Patil, K.R., Peelle, J.E., Pérez, A., Pischedda, D., Poline, J.-B., Prystauka, Y., Ray, S., Reuter-Lorenz, P.A., Reynolds, R.C., Ricciardi, E., Rieck, J.R., Rodriguez-Thompson, A.M., Romyn, A., Salo, T., Samanez-Larkin, G.R.,

Sanz-Morales, E., Schlichting, M.L., Schultz, D.H., Shen, Q., Sheridan, M.A., Silvers, J.A., Skagerlund, K., Smith, A., Smith, D.V., Sokol-Hessner, P., Steinkamp, S.R., Tashjian, S.M., Thirion, B., Thorp, J.N., Tinghög, G., Tisdall, L., Tompson, S.H., Toro-Serey, C., Torre Tresols, J.J., Tozzi, L., Truong, V., Turella, L., van 't Veer, A.E., Verguts, T., Vettel, J.M., Vijayarajah, S., Vo, K., Wall, M.B., Weeda, W.D., Weis, S., White, D.J., Wisniewski, D., Xifra-Porxas, A., Yearling, E.A., Yoon, S., Yuan, R., Yuen, K.S.L., Zhang, L., Zhang, X., Zosky, J.E., Nichols, T.E., Poldrack, R.A., Schonberg, T., 2020. Variability in the analysis of a single neuroimaging dataset by many teams. Nature 582, 84–88. https://doi.org/10.1038/s41586-020-2314-9

Brodmann, K., 1909. Vergleichende Lokalisationslehre der Grosshirnrinde in ihren Prinzipien dargestellt auf Grund des Zellenbaues. Barth.

Brown, J.C., DeVries, W.H., Korte, J.E., Sahlem, G.L., Bonilha, L., Short, E.B., George, M.S., 2020. NMDA receptor partial agonist, d-cycloserine, enhances 10 Hz rTMS-induced motor plasticity, suggesting long-term potentiation (LTP) as underlying mechanism. Brain Stimul. 13, 530–532. https://doi.org/10.1016/j.brs.2020.01.005

Buckner, R.L., Krienen, F.M., Yeo, B.T.T., 2013. Opportunities and limitations of intrinsic functional connectivity MRI. Nat. Neurosci. 16, 832–837. https://doi.org/10.1038/nn.3423

Bueichekú, E., Ávila, C., Miró-Padilla, A., Sepulcre, J., 2019. Visual search task immediate training effects on task-related functional connectivity. Brain Imaging Behav. 13, 1566–1579. https://doi.org/10.1007/s11682-018-9993-y

Bullmore, E., Sporns, O., 2009. Complex brain networks: graph theoretical analysis of structural and functional systems. Nat. Rev. Neurosci. 10, 186–198. https://doi.org/10.1038/nrn2575

Buzsaki, G., 2006. Rhythms of the Brain. Oxford University Press.

Cao, N., Pi, Y., Liu, K., Meng, H., Wang, Y., Zhang, J., Wu, Y., Tan, X., 2018. Inhibitory and facilitatory connections from dorsolateral prefrontal to primary motor cortex in healthy humans at rest—An rTMS study. Neurosci. Lett. 687, 82–87. https://doi.org/10.1016/j.neulet.2018.09.032

Caporale, N., Dan, Y., 2008. Spike Timing–Dependent Plasticity: A Hebbian Learning Rule. https://doi.org/10.1146/annurev.neuro.31.060407.125639

Cárdenas-Morales, L., Volz, L.J., Michely, J., Rehme, A.K., Pool, E.M., Nettekoven, C., Eickhoff, S.B., Fink, G.R., Grefkes, C., 2014. Network connectivity and individual responses to brain stimulation in the human motor system. Cereb. Cortex 24, 1697–1707. https://doi.org/10.1093/cercor/bht023

Catani, M., de Schotten, M.T., 2012. Atlas of Human Brain Connections (all tracts). Atlas of Human Brain Connections. https://doi.org/10.1093/med/9780199541164.003.0073

Chang, Y.S., Owen, J.P., Pojman, N.J., Thieu, T., Bukshpun, P., Wakahiro, M.L.J., Berman, J.I., Roberts, T.P.L., Nagarajan, S.S., Sherr, E.H., Mukherjee, P., 2015. White Matter Changes of Neurite Density and Fiber Orientation Dispersion during Human Brain Maturation. PLoS One 10, e0123656. https://doi.org/10.1371/journal.pone.0123656

Chen, L., Thomas, E.H.X., Kaewpijit, P., Miljevic, A., Hughes, R., Hahn, L., Kato, Y., Gill, S., Clarke, P., Ng, F., Paterson, T., Giam, A., Sarma, S., Hoy, K.E., Galletly, C., Fitzgerald, P.B., 2021. Accelerated theta burst stimulation for the treatment of depression: A randomised controlled trial. Brain Stimul. 14, 1095–1105. https://doi.org/10.1016/j.brs.2021.07.018

Chen, M., Lixandrão, M.C., Prudente, C.N., Summers, R.L.S., Kimberley, T.J., 2018. Short Interval Intracortical Inhibition Responses to Low-Frequency Repetitive Transcranial Magnetic Stimulation Under Multiple Interstimulus Intervals and Conditioning Intensities. Neuromodulation 21, 368–375. https://doi.org/10.1111/ner.12773

Chiang, M.C., Barysheva, M., Toga, A.W., Medland, S.E., Hansell, N.K., James, M.R., McMahon, K.L., de Zubicaray, G.I., Martin, N.G., Wright, M.J., Thompson, P.M., 2011. BDNF gene effects on brain circuitry replicated in 455 twins. Neuroimage 55, 448–454. https://doi.org/10.1016/j.neuroimage.2010.12.053
Citri, A., Malenka, R.C., 2008. Synaptic plasticity: multiple forms, functions, and mechanisms. Neuropsychopharmacology 33, 18–41. https://doi.org/10.1038/sj.npp.1301559
Civardi, C., Cantello, R., Asselman, P., Rothwell, J.C., 2001. Transcranial Magnetic Stimulation Can Be Used to Test Connections to Primary Motor Areas from Frontal and Medial Cortex in Humans. NeuroImage. https://doi.org/10.1006/nimg.2001.0918
Cole, D.M., Smith, S.M., Beckmann, C.F., 2010. Advances and pitfalls in the analysis and interpretation of resting-state FMRI data. Front. Syst. Neurosci. 4, 8. https://doi.org/10.3389/fnsys.2010.00008
Cole, E.J., Phillips, A.L., Bentzley, B.S., Stimpson, K.H., Nejad, R., Barmak, F., Veerapal, C., Khan, N., Cherian, K., Felber, E., Brown, R., Choi, E., King, S., Pankow, H., Bishop, J.H., Azeez, A., Coetzee, J., Rapier, R., Odenwald, N., Carreon, D., Hawkins, J., Chang, M., Keller, J., Raj, K., DeBattista, C., Jo, B., Espil, F.M., Schatzberg, A.F., Sudheimer, K.D., Williams, N.R., 2022. Stanford Neuromodulation Therapy (SNT): A Double-Blind Randomized Controlled Trial. Am. J. Psychiatry 179, 132–141. https://doi.org/10.1176/appi.ajp.2021.20101429
Cole, J., Selby, B., Ismail, Z., McGirr, A., 2021. D-cycloserine normalizes long-term motor plasticity after transcranial magnetic intermittent theta-burst stimulation in major depressive disorder. Clin. Neurophysiol. 132, 1770–1776. https://doi.org/10.1016/j.clinph.2021.04.002
Cooper, L.N., Bear, M.F., 2012. The BCM theory of synapse modification at 30: interaction of theory with experiment. Nat. Rev. Neurosci. 13, 798–810. https://doi.org/10.1038/nrn3353
Corp, D.T., Bereznicki, H.G.K., Clark, G.M., Youssef, G.J., Fried, P.J., Jannati, A., Davies, C.B., Gomes-Osman, J., Stamm, J., Chung, S.W., Bowe, S.J., Rogasch, N.C., Fitzgerald, P.B., Koch, G., Di Lazzaro, V., Pascual-Leone, A., Enticott, P.G., 2020. Large-scale analysis of interindividual variability in theta-burst stimulation data: Results from the "Big TMS Data Collaboration." Brain Stimul. 13, 1476–1488. https://doi.org/10.1016/j.brs.2020.07.018
Cullen, C.L., Young, K.M., 2016. How does transcranial magnetic stimulation influence glial cells in the central nervous system? Front. Neural Circuits 10, 1–10. https://doi.org/10.3389/fncir.2016.00026
Dale, A.M., Fischl, B., Sereno, M.I., 1999. Cortical surface-based analysis. I. Segmentation and surface reconstruction. Neuroimage 9, 179–194. https://doi.org/10.1006/nimg.1998.0395
Debacker, C., Djemai, B., Ciobanu, L., Tsurugizawa, T., Le Bihan, D., 2020. Diffusion MRI reveals in vivo and non-invasively changes in astrocyte function induced by an aquaporin-4 inhibitor. PLoS One 15, e0229702. https://doi.org/10.1371/journal.pone.0229702
Deng, Z.-D., Lisanby, S.H., Peterchev, A.V., 2013. Electric field depth–focality tradeoff in transcranial magnetic stimulation: Simulation comparison of 50 coil designs. Brain Stimul. 6, 1–13. https://doi.org/10.1016/j.brs.2012.02.005
Dennis, E.L., Thompson, P.M., 2014. Functional brain connectivity using fMRI in aging and Alzheimer's disease. Neuropsychol. Rev. 24, 49–62. https://doi.org/10.1007/s11065-014-9249-6
Desikan, R.S., Ségonne, F., Fischl, B., Quinn, B.T., Dickerson, B.C., Blacker, D., Buckner,

R.L., Dale, A.M., Maguire, R.P., Hyman, B.T., Albert, M.S., Killiany, R.J., 2006. An automated labeling system for subdividing the human cerebral cortex on MRI scans into gyral based regions of interest. Neuroimage 31, 968–980. https://doi.org/10.1016/j.neuroimage.2006.01.021

Dickins, D.S.E., Sale, M.V., Kamke, M.R., 2015. Plasticity Induced by Intermittent Theta Burst Stimulation in Bilateral Motor Cortices Is Not Altered in Older Adults. Neural Plast. 2015, 323409. https://doi.org/10.1155/2015/323409

Di Lazzaro, V., Profice, P., Pilato, F., Dileone, M., Oliviero, A., Ziemann, U., 2010. The effects of motor cortex rTMS on corticospinal descending activity. Clin. Neurophysiol. 121, 464–473. https://doi.org/10.1016/j.clinph.2009.11.007

Ding, Q., Lin, T., Wu, M., Yang, W., Li, W., Jing, Y., Ren, X., Gong, Y., Xu, G., Lan, Y., 2021. Influence of iTBS on the Acute Neuroplastic Change After BCI Training. Front. Cell. Neurosci. 15, 653487. https://doi.org/10.3389/fncel.2021.653487

Doucette, J., Kames, C., Hernández-Torres, E., 2019. The role of diffusion and perivascular spaces in dynamic susceptibility contrast MRI. bioRxiv.

Drakaki, M., Mathiesen, C., Siebner, H.R., Madsen, K., Thielscher, A., 2022. Database of 25 validated coil models for electric field simulations for TMS. Brain Stimul. 15, 697–706. https://doi.org/10.1016/j.brs.2022.04.017

Drew, P.J., 2022. Neurovascular coupling: motive unknown. Trends Neurosci. https://doi.org/10.1016/j.tins.2022.08.004

Duning, T., Rogalewski, A., Steinstraeter, O., Kugel, H., Jansen, A., Breitenstein, C., Knecht, S., 2004. Repetitive TMS temporarily alters brain diffusion. Neurology. https://doi.org/10.1212/wnl.62.11.2144

Eklund, A., Nichols, T.E., Knutsson, H., 2016. Cluster failure: Why fMRI inferences for spatial extent have inflated false-positive rates. Proc. Natl. Acad. Sci. U. S. A. 113, 7900–7905. https://doi.org/10.1073/pnas.1602413113

Engert, F., Bonhoeffer, T., 1999. Dendritic spine changes associated with hippocampal long-term synaptic plasticity. Nature 399, 66–70. https://doi.org/10.1038/19978

Falahpour, M., Chang, C., Wong, C.W., Liu, T.T., 2018. Template-based prediction of vigilance fluctuations in resting-state fMRI. Neuroimage 174, 317–327. https://doi.org/10.1016/j.neuroimage.2018.03.012

Faraday, M., 1839. Experimental Researches in Electricity: Reprinted from the Philosophical Transactions of 1831-1843, 1846-1852. R. and J.E. Taylor.

Ferbert, A., Priori, A., Rothwell, J.C., Day, B.L., Colebatch, J.G., Marsden, C.D., 1992. Interhemispheric inhibition of the human motor cortex. J. Physiol. 453, 525–546. https://doi.org/10.1113/jphysiol.1992.sp019243

Fischl, B., Sereno, M.I., Dale, A.M., 1999. Cortical surface-based analysis. II: Inflation, flattening, and a surface-based coordinate system. Neuroimage 9, 195–207. https://doi.org/10.1006/nimg.1998.0396

Fried, P.J., Jannati, A., Davila-Pérez, P., Pascual-Leone, A., 2017. Reproducibility of single-pulse, paired-pulse, and intermittent theta-burst TMS measures in healthy aging, Type-2 diabetes, and Alzheimer's disease. Front. Aging Neurosci. 9, 1–13. https://doi.org/10.3389/fnagi.2017.00263

Friston, K., 2012. Prediction, perception and agency. Int. J. Psychophysiol. 83, 248–252. https://doi.org/10.1016/j.ijpsycho.2011.11.014

Friston, K., Mattout, J., Kilner, J., 2011. Action understanding and active inference. Biol. Cybern. 104, 137–160. https://doi.org/10.1007/s00422-011-0424-z

Fukutomi, H., Glasser, M.F., Murata, K., Akasaka, T., Fujimoto, K., Yamamoto, T., Autio, J.A., Okada, T., Togashi, K., Zhang, H., Van Essen, D.C., Hayashi, T., 2019. Diffusion Tensor Model links to Neurite Orientation Dispersion and Density Imaging at high

b-value in Cerebral Cortical Gray Matter. Sci. Rep. 9, 6–7. https://doi.org/10.1038/s41598-019-48671-7
Fukutomi, H., Glasser, M.F., Zhang, H., Autio, J.A., Coalson, T.S., Okada, T., Togashi, K., Van Essen, D.C., Hayashi, T., 2018. Neurite imaging reveals microstructural variations in human cerebral cortical gray matter. Neuroimage 182, 488–499. https://doi.org/10.1016/j.neuroimage.2018.02.017
García-Marín, V., Blazquez-Llorca, L., Rodriguez, J.R., Gonzalez-Soriano, J., DeFelipe, J., 2010. Differential distribution of neurons in the gyral white matter of the human cerebral cortex. J. Comp. Neurol. 518, 4740–4759. https://doi.org/10.1002/cne.22485
Genon, S., Eickhoff, S.B., Kharabian, S., 2022. Linking interindividual variability in brain structure to behaviour. Nat. Rev. Neurosci. 23, 307–318. https://doi.org/10.1038/s41583-022-00584-7
Gibson, E.M., Purger, D., Mount, C.W., Goldstein, A.K., Lin, G.L., Wood, L.S., Inema, I., Miller, S.E., Bieri, G., Zuchero, J.B., Barres, B.A., Woo, P.J., Vogel, H., Monje, M., 2014. Neuronal activity promotes oligodendrogenesis and adaptive myelination in the mammalian brain. Science 344, 1252304. https://doi.org/10.1126/science.1252304
Glasser, M.F., Coalson, T.S., Harms, M.P., Baum, G.L., Autio, J.A., Auerbach, E.J., Xu, J., Greve, D.N., Yacoub, E., Van Essen, D.C., Bock, N.A., Hayashi, T., 2021. Transmit Field Bias Correction of T1w/T2w Myelin Maps. bioRxiv. https://doi.org/10.1101/2021.08.08.455570
Glasser, M.F., Coalson, T.S., Robinson, E.C., Hacker, C.D., Harwell, J., Yacoub, E., Ugurbil, K., Andersson, J., Beckmann, C.F., Jenkinson, M., Smith, S.M., Van Essen, D.C., 2016a. A multi-modal parcellation of human cerebral cortex. Nature 536, 171–178. https://doi.org/10.1038/nature18933
Glasser, M.F., Smith, S.M., Marcus, D.S., Andersson, J.L.R., Auerbach, E.J., Behrens, T.E.J., Coalson, T.S., Harms, M.P., Jenkinson, M., Moeller, S., Robinson, E.C., Sotiropoulos, S.N., Xu, J., Yacoub, E., Ugurbil, K., Van Essen, D.C., 2016b. The Human Connectome Project's neuroimaging approach. Nat. Neurosci. 19, 1175–1187. https://doi.org/10.1038/nn.4361
Glasser, M.F., Sotiropoulos, S.N., Wilson, J.A., Coalson, T.S., Fischl, B., Andersson, J.L., Xu, J., Jbabdi, S., Webster, M., Polimeni, J.R., Van Essen, D.C., Jenkinson, M., WU-Minn HCP Consortium, 2013. The minimal preprocessing pipelines for the Human Connectome Project. Neuroimage 80, 105–124. https://doi.org/10.1016/j.neuroimage.2013.04.127
Glasser, M.F., Van Essen, D.C., 2011. Mapping human cortical areas in vivo based on myelin content as revealed by T1- and T2-weighted MRI. J. Neurosci. 31, 11597–11616. https://doi.org/10.1523/JNEUROSCI.2180-11.2011
Gomez, J., Barnett, M.A., Natu, V., Mezer, A., Palomero-Gallagher, N., Weiner, K.S., Amunts, K., Zilles, K., Grill-Spector, K., 2017. Microstructural proliferation in human cortex is coupled with the development of face processing. Science 355, 68–71. https://doi.org/10.1126/science.aag0311
Gonzalez-Castillo, J., Kam, J.W.Y., Hoy, C.W., Bandettini, P.A., 2021. How to Interpret Resting-State fMRI: Ask Your Participants. The Journal of Neuroscience. https://doi.org/10.1523/jneurosci.1786-20.2020
Griffanti, L., Douaud, G., Bijsterbosch, J., Evangelisti, S., Alfaro-Almagro, F., Glasser, M.F., Duff, E.P., Fitzgibbon, S., Westphal, R., Carone, D., Beckmann, C.F., Smith, S.M., 2017. Hand classification of fMRI ICA noise components. Neuroimage 154, 188–205. https://doi.org/10.1016/j.neuroimage.2016.12.036
Griffanti, L., Salimi-Khorshidi, G., Beckmann, C.F., Auerbach, E.J., Douaud, G., Sexton, C.E., Zsoldos, E., Ebmeier, K.P., Filippini, N., Mackay, C.E., Moeller, S., Xu, J.,

Yacoub, E., Baselli, G., Ugurbil, K., Miller, K.L., Smith, S.M., 2014. ICA-based artefact removal and accelerated fMRI acquisition for improved resting state network imaging. Neuroimage 95, 232–247. https://doi.org/10.1016/j.neuroimage.2014.03.034

Groppa, S., Werner-Petroll, N., Münchau, A., Deuschl, G., Ruschworth, M.F.S., Siebner, H.R., 2012. A novel dual-site transcranial magnetic stimulation paradigm to probe fast facilitatory inputs from ipsilateral dorsal premotor cortex to primary motor cortex. Neuroimage 62, 500–509. https://doi.org/10.1016/j.neuroimage.2012.05.023

Grussu, F., Schneider, T., Tur, C., Yates, R.L., Tachrount, M., Ianuş, A., Yiannakas, M.C., Newcombe, J., Zhang, H., Alexander, D.C., DeLuca, G.C., Gandini Wheeler-Kingshott, C.A.M., 2017. Neurite dispersion: a new marker of multiple sclerosis spinal cord pathology? Ann Clin Transl Neurol 4, 663–679. https://doi.org/10.1002/acn3.445

Guerrero, J.M., Adluru, N., Bendlin, B.B., Goldsmith, H.H., Schaefer, S.M., Davidson, R.J., Kecskemeti, S.R., Zhang, H., Alexander, A.L., 2019. Optimizing the intrinsic parallel diffusivity in NODDI: An extensive empirical evaluation. PLoS One 14, e0217118. https://doi.org/10.1371/journal.pone.0217118

Haimovici, A., Tagliazucchi, E., Balenzuela, P., Laufs, H., 2017. On wakefulness fluctuations as a source of BOLD functional connectivity dynamics. Sci. Rep. 7, 5908. https://doi.org/10.1038/s41598-017-06389-4

Hallett, M., 2007. Transcranial Magnetic Stimulation: A Primer. Neuron 55, 187–199. https://doi.org/10.1016/j.neuron.2007.06.026

Hamada, M., Hanajima, R., Terao, Y., Arai, N., Furubayashi, T., Inomata-Terada, S., Yugeta, A., Matsumoto, H., Shirota, Y., Ugawa, Y., 2007. Quadro-pulse stimulation is more effective than paired-pulse stimulation for plasticity induction of the human motor cortex. Clin. Neurophysiol. 118, 2672–2682. https://doi.org/10.1016/j.clinph.2007.09.062

Hamada, M., Murase, N., Hasan, A., Balaratnam, M., Rothwell, J.C., 2013. The role of interneuron networks in driving human motor cortical plasticity. Cereb. Cortex 23, 1593–1605. https://doi.org/10.1093/cercor/bhs147

Hamada, M., Terao, Y., Hanajima, R., Shirota, Y., Nakatani-Enomoto, S., Furubayashi, T., Matsumoto, H., Ugawa, Y., 2008. Bidirectional long-term motor cortical plasticity and metaplasticity induced by quadripulse transcranial magnetic stimulation. J. Physiol. 586, 3927–3947. https://doi.org/10.1113/jphysiol.2008.152793

Hanajima, R., Shadmehr, R., Ohminami, S., Tsutsumi, R., Shirota, Y., Shimizu, T., Tanaka, N., Terao, Y., Tsuji, S., Ugawa, Y., Uchimura, M., Inoue, M., Kitazawa, S., 2015. Modulation of error-sensitivity during a prism adaptation task in people with cerebellar degeneration. J. Neurophysiol. 114, 2460–2471. https://doi.org/10.1152/jn.00145.2015

Hanajima, R., Ugawa, Y., Machii, K., Mochizuki, H., Terao, Y., Enomoto, H., Furubayashi, T., Shiio, Y., Uesugi, H., Kanazawa, I., 2001. Interhemispheric facilitation of the hand motor area in humans. J. Physiol. 531, 849–859. https://doi.org/10.1111/j.1469-7793.2001.0849h.x

Hasan, A., Galea, J.M., Casula, E.P., Falkai, P., Bestmann, S., Rothwell, J.C., 2013. Muscle and timing-specific functional connectivity between the dorsolateral prefrontal cortex and the primary motor cortex. J. Cogn. Neurosci. 25, 558–570. https://doi.org/10.1162/jocn_a_00338

Hashemi, R.H., Bradley, W.G., Lisanti, C.J., 2012. MRI: The Basics: The Basics. Lippincott Williams & Wilkins.

Hinder, M.R., Goss, E.L., Fujiyama, H., Canty, A.J., Garry, M.I., Rodger, J., Summers, J.J., 2014. Inter- and intra-individual variability following intermittent theta burst stimulation: Implications for rehabilitation and recovery. Brain Stimul. 7, 365–371. https://doi.org/10.1016/j.brs.2014.01.004

Hoddes, E., 1972. Dement, WC. & Zarcone, V.(1972). The development and use of the Stanford Sleepiness Scale (SSS). Psychophysiology 9, 150.
Hofer, S., Frahm, J., 2006. Topography of the human corpus callosum revisited-Comprehensive fiber tractography using diffusion tensor magnetic resonance imaging. Neuroimage 32, 989–994. https://doi.org/10.1016/j.neuroimage.2006.05.044
Hoppenrath, K., Funke, K., 2013. Neuroscience Letters Time-course of changes in neuronal activity markers following iTBS-TMS of the rat neocortex. Neurosci. Lett. 536, 19–23. https://doi.org/10.1016/j.neulet.2013.01.003
Horvath, J.C., Mathews, J., Demitrack, M.A., Pascual-Leone, A., 2010. The NeuroStar TMS device: conducting the FDA approved protocol for treatment of depression. J. Vis. Exp. https://doi.org/10.3791/2345
Hoshi, E., Tanji, J., 2007. Distinctions between dorsal and ventral premotor areas: anatomical connectivity and functional properties. Curr. Opin. Neurobiol. 17, 234–242. https://doi.org/10.1016/j.conb.2007.02.003
Hoy, A.R., Koay, C.G., Kecskemeti, S.R., Alexander, A.L., 2014. Optimization of a free water elimination two-compartment model for diffusion tensor imaging. Neuroimage 103, 323–333. https://doi.org/10.1016/j.neuroimage.2014.09.053
Huang, Y.-Z., Chen, R.-S., Fong, P.-Y., Rothwell, J.C., Chuang, W.-L., Weng, Y.-H., Lin, W.-Y., Lu, C.-S., 2018. Inter-cortical modulation from premotor to motor plasticity. J. Physiol. 596, 4207–4217.
Huang, Y.-Z., Chen, R.-S., Rothwell, J.C., Wen, H.-Y., 2007. The after-effect of human theta burst stimulation is NMDA receptor dependent. Clin. Neurophysiol. 118, 1028–1032. https://doi.org/10.1016/j.clinph.2007.01.021
Huang, Y.Z., Edwards, M.J., Rounis, E., Bhatia, K.P., Rothwell, J.C., 2005. Theta burst stimulation of the human motor cortex. Neuron 45, 201–206. https://doi.org/10.1016/j.neuron.2004.12.033
Huang, Y.Z., Rothwell, J.C., Chen, R.S., Lu, C.S., Chuang, W.L., 2011. The theoretical model of theta burst form of repetitive transcranial magnetic stimulation. Clin. Neurophysiol. 122, 1011–1018. https://doi.org/10.1016/j.clinph.2010.08.016
Huettel, S.A., Song, A.W., McCarthy, G., 2009. Functional Magnetic Resonance Imaging. Oxford University Press, Incorporated.
Jackson, N., Greenhouse, I., 2019. VETA: An Open-Source Matlab-Based Toolbox for the Collection and Analysis of Electromyography Combined With Transcranial Magnetic Stimulation. Front. Neurosci. 13, 1–12. https://doi.org/10.3389/fnins.2019.00975
Jbabdi, S., Sotiropoulos, S.N., Savio, A.M., Graña, M., Behrens, T.E.J., 2012. Model-based analysis of multishell diffusion MR data for tractography: how to get over fitting problems. Magn. Reson. Med. 68, 1846–1855. https://doi.org/10.1002/mrm.24204
Jeurissen, B., Leemans, A., Tournier, J.-D., Jones, D.K., Sijbers, J., 2013. Investigating the prevalence of complex fiber configurations in white matter tissue with diffusion magnetic resonance imaging. Hum. Brain Mapp. 34, 2747–2766. https://doi.org/10.1002/hbm.22099
Johansen-Berg, H., Baptista, C.S., Thomas, A.G., 2012. Human Structural Plasticity at Record Speed. Neuron 73, 1058–1060. https://doi.org/10.1016/j.neuron.2012.03.001
Johansen-Berg, H., Behrens, T.E.J., 2013. Diffusion MRI: From Quantitative Measurement to In vivo Neuroanatomy. Academic Press.
Jones, D.K., Symms, M.R., Cercignani, M., Howard, R.J., 2005. The effect of filter size on VBM analyses of DT-MRI data. Neuroimage 26, 546–554. https://doi.org/10.1016/j.neuroimage.2005.02.013
Jung, J., Lambon Ralph, M.A., 2021. The immediate impact of transcranial magnetic stimulation on brain structure: Short-term neuroplasticity following one session of

cTBS. Neuroimage 240, 118375. https://doi.org/10.1016/j.neuroimage.2021.118375
Jung, J., Lambon Ralph, M.A., 2016. Mapping the Dynamic Network Interactions Underpinning Cognition: A cTBS-fMRI Study of the Flexible Adaptive Neural System for Semantics. Cereb. Cortex 26, 3580–3590. https://doi.org/10.1093/cercor/bhw149
Kadowaki, S., Enomoto, H., Murakami, T., Nakatani-Enomoto, S., Kobayashi, S., Ugawa, Y., 2016. Influence of phasic muscle contraction upon the quadripulse stimulation (QPS) aftereffects. Clin. Neurophysiol. 127, 1568–1573. https://doi.org/10.1016/j.clinph.2015.10.063
Kaelin-Lang, A., Luft, A.R., Sawaki, L., Burstein, A.H., Sohn, Y.H., Cohen, L.G., 2002. Modulation of human corticomotor excitability by somatosensory input. J. Physiol. 540, 623–633. https://doi.org/10.1113/jphysiol.2001.012801
Kanai, R., Rees, G., 2011. The structural basis of inter-individual differences in human behaviour and cognition. Nat. Rev. Neurosci. 12, 231–242. https://doi.org/10.1038/nrn3000
Kandel, E.R., Koester, J.D., Mack, S.H., Siegelbaum, S.A., 2021. Principles of Neural Science, Sixth Edition. McGraw Hill Professional.
Katayama, T., Rothwell, J.C., 2007. Modulation of somatosensory evoked potentials using transcranial magnetic intermittent theta burst stimulation. Clin. Neurophysiol. 118, 2506–2511. https://doi.org/10.1016/j.clinph.2007.08.011
Kharabian Masouleh, S., Eickhoff, S.B., Zeighami, Y., Lewis, L.B., Dahnke, R., Gaser, C., Chouinard-Decorte, F., Lepage, C., Scholtens, L.H., Hoffstaedter, F., Glahn, D.C., Blangero, J., Evans, A.C., Genon, S., Valk, S.L., 2020. Influence of Processing Pipeline on Cortical Thickness Measurement. Cereb. Cortex 30, 5014–5027. https://doi.org/10.1093/cercor/bhaa097
Kimura, I., Oishi, H., Hayashi, M.J., Amano, K., 2021. Microstructural Properties of Human Brain Revealed by Fractional Anisotropy Can Predict the After-Effect of Intermittent Theta Burst Stimulation. Cereb Cortex Commun. https://doi.org/10.1101/2021.08.30.458153
Koch, G., Fernandez Del Olmo, M., Cheeran, B., Ruge, D., Schippling, S., Caltagirone, C., Rothwell, J.C., 2007. Focal stimulation of the posterior parietal cortex increases the excitability of the ipsilateral motor cortex. J. Neurosci. 27, 6815–6822. https://doi.org/10.1523/JNEUROSCI.0598-07.2007
Koike, S., Tanaka, S.C., Okada, T., Aso, T., Yamashita, A., Yamashita, O., Asano, M., Maikusa, N., Morita, K., Okada, N., Fukunaga, M., Uematsu, A., Togo, H., Miyazaki, A., Murata, K., Urushibata, Y., Autio, J., Ose, T., Yoshimoto, J., Araki, T., Glasser, M.F., Van Essen, D.C., Maruyama, M., Sadato, N., Kawato, M., Kasai, K., Okamoto, Y., Hanakawa, T., Hayashi, T., 2021. Brain/MINDS beyond human brain MRI project: A protocol for multi-level harmonization across brain disorders throughout the lifespan. NeuroImage: Clinical 30, 102600. https://doi.org/10.1016/j.nicl.2021.102600
Komaki, Y., Debacker, C., Djemai, B., Ciobanu, L., Tsurugizawa, T., Le Bihan, D., 2020. Differential effects of aquaporin-4 channel inhibition on BOLD fMRI and diffusion fMRI responses in mouse visual cortex. PLoS One 15, e0228759. https://doi.org/10.1371/journal.pone.0228759
Koopmans, P.J., Barth, M., Norris, D.G., 2010. Layer-specific BOLD activation in human V1. Hum. Brain Mapp. 31, 1297–1304. https://doi.org/10.1002/hbm.20936
Kujirai, K., Kujirai, T., Sinkjaer, T., Rothwell, J.C., 2006. Associative plasticity in human motor cortex during voluntary muscle contraction. J. Neurophysiol. 96, 1337–1346. https://doi.org/10.1152/jn.01140.2005
Kumar, P., Yadav, A.K., Misra, S., Kumar, A., Chakravarty, K., Prasad, K., 2016. Prediction of upper extremity motor recovery after subacute intracerebral hemorrhage through

diffusion tensor imaging: a systematic review and meta-analysis. Neuroradiology 58, 1043–1050. https://doi.org/10.1007/s00234-016-1718-6
Lampinen, B., Szczepankiewicz, F., Mårtensson, J., van Westen, D., Sundgren, P.C., Nilsson, M., 2017. Neurite density imaging versus imaging of microscopic anisotropy in diffusion MRI: A model comparison using spherical tensor encoding. Neuroimage 147, 517–531. https://doi.org/10.1016/j.neuroimage.2016.11.053
Larson, J., Lynch, G., 1986. Induction of synaptic potentiation in hippocampus by patterned stimulation involves two events. Science 232, 985–988. https://doi.org/10.1126/science.3704635
Lassek, A.M., 1941. The Human Pyramidal Tract II. A Numerical Investigation of the Betz Cells of the Motor Area. The Journal of Nervous and Mental Disease. https://doi.org/10.1097/00005053-194194020-00026
Laumann, T.O., Snyder, A.Z., Mitra, A., Gordon, E.M., Gratton, C., Adeyemo, B., Gilmore, A.W., Nelson, S.M., Berg, J.J., Greene, D.J., McCarthy, J.E., Tagliazucchi, E., Laufs, H., Schlaggar, B.L., Dosenbach, N.U.F., Petersen, S.E., 2017. On the Stability of BOLD fMRI Correlations. Cereb. Cortex 27, 4719–4732. https://doi.org/10.1093/cercor/bhw265
Lazari, A., Lipp, I., 2021. Can MRI measure myelin? Systematic review, qualitative assessment, and meta-analysis of studies validating microstructural imaging with myelin histology. Neuroimage 230, 117744. https://doi.org/10.1016/j.neuroimage.2021.117744
Lazari, A., Salvan, P., Cottaar, M., Papp, D., Rushworth, M.F.S., Johansen-Berg, H., 2022. Hebbian activity-dependent plasticity in white matter. Cell Rep. 39, 110951. https://doi.org/10.1016/j.celrep.2022.110951
Le Bihan, D., 2003. Looking into the functional architecture of the brain with diffusion MRI. Nat. Rev. Neurosci. 4, 469–480. https://doi.org/10.1038/nrn1119
Le Bihan, D., Mangin, J.F., Poupon, C., Clark, C.A., Pappata, S., Molko, N., Chabriat, H., 2001. Diffusion tensor imaging: concepts and applications. J. Magn. Reson. Imaging 13, 534–546. https://doi.org/10.1002/jmri.1076
Lefaucheur, J.-P., Aleman, A., Baeken, C., Benninger, D.H., Brunelin, J., Di Lazzaro, V., Filipović, S.R., Grefkes, C., Hasan, A., Hummel, F.C., Jääskeläinen, S.K., Langguth, B., Leocani, L., Londero, A., Nardone, R., Nguyen, J.-P., Nyffeler, T., Oliveira-Maia, A.J., Oliviero, A., Padberg, F., Palm, U., Paulus, W., Poulet, E., Quartarone, A., Rachid, F., Rektorová, I., Rossi, S., Sahlsten, H., Schecklmann, M., Szekely, D., Ziemann, U., 2020. Evidence-based guidelines on the therapeutic use of repetitive transcranial magnetic stimulation (rTMS): An update (2014–2018). Clin. Neurophysiol. 131, 474–528. https://doi.org/10.1016/j.clinph.2019.11.002
Lehmann, N., Tolentino-Castro, J.W., Kaminski, E., Ragert, P., Villringer, A., Taubert, M., 2019. Interindividual differences in gray and white matter properties are associated with early complex motor skill acquisition. Hum. Brain Mapp. 40, 4316–4330. https://doi.org/10.1002/hbm.24704
Lemon, R.N., 2008. Descending pathways in motor control. Annu. Rev. Neurosci. 31, 195–218. https://doi.org/10.1146/annurev.neuro.31.060407.125547
Leodori, G., Fabbrini, A., Ilenia De Bartolo, M., Costanzo, M., Asci, F., Palma, V., Belvisi, D., Conte, A., Berardelli, A., 2021. Cortical Mechanisms underlying Variability in Intermittent Theta-Burst Stimulation-Induced Plasticity: A TMS-EEG Study. Clin. Neurophysiol. https://doi.org/10.1016/j.clinph.2021.06.021
Li, C.-T., Chen, M.-H., Juan, C.-H., Huang, H.-H., Chen, L.-F., Hsieh, J.-C., Tu, P.-C., Bai, Y.-M., Tsai, S.-J., Lee, Y.-C., Su, T.-P., 2014. Efficacy of prefrontal theta-burst stimulation in refractory depression: a randomized sham-controlled study. Brain 137, 2088–2098. https://doi.org/10.1093/brain/awu109

Li, C.-T., Chen, M.-H., Juan, C.-H., Liu, R.-S., Lin, W.-C., Bai, Y.-M., Su, T.-P., 2018. Effects of prefrontal theta-burst stimulation on brain function in treatment-resistant depression: A randomized sham-controlled neuroimaging study. Brain Stimul. 11, 1054–1062. https://doi.org/10.1016/j.brs.2018.04.014

Li, C.T., Huang, Y.Z., Bai, Y.M., Tsai, S.J., Su, T.P., Cheng, C.M., 2019. Critical role of glutamatergic and GABAergic neurotransmission in the central mechanisms of theta-burst stimulation. Hum. Brain Mapp. 40, 2001–2009. https://doi.org/10.1002/hbm.24485

Lipp, I., Jones, D.K., Bells, S., Sgarlata, E., Foster, C., Stickland, R., Davidson, A.E., Tallantyre, E.C., Robertson, N.P., Wise, R.G., Tomassini, V., 2019. Comparing MRI metrics to quantify white matter microstructural damage in multiple sclerosis. Human Brain Mapping. https://doi.org/10.1002/hbm.24568

Logothetis, N.K., 2008. What we can do and what we cannot do with fMRI. Nature 453, 869–878. https://doi.org/10.1038/nature06976

Logothetis, N.K., 2003. The underpinnings of the BOLD functional magnetic resonance imaging signal. J. Neurosci. 23, 3963–3971.

Logothetis, N.K., Wandell, B.A., 2004. Interpreting the BOLD signal. Annu. Rev. Physiol. 66, 735–769. https://doi.org/10.1146/annurev.physiol.66.082602.092845

López-Alonso, V., Cheeran, B., Río-Rodríguez, D., Fernández-Del-Olmo, M., 2014. Inter-individual variability in response to non-invasive brain stimulation paradigms. Brain Stimul. 7, 372–380. https://doi.org/10.1016/j.brs.2014.02.004

Maeda, J., Suhara, T., Zhang, M.-R., Okauchi, T., Yasuno, F., Ikoma, Y., Inaji, M., Nagai, Y., Takano, A., Obayashi, S., Suzuki, K., 2004. Novel peripheral benzodiazepine receptor ligand [11C]DAA1106 for PET: an imaging tool for glial cells in the brain. Synapse 52, 283–291. https://doi.org/10.1002/syn.20027

Malenka, R.C., Bear, M.F., 2004. LTP and LTD: an embarrassment of riches. Neuron 44, 5–21. https://doi.org/10.1016/j.neuron.2004.09.012

Malinow, R., Malenka, R.C., 2002. AMPA receptor trafficking and synaptic plasticity. Annu. Rev. Neurosci. 25, 103–126. https://doi.org/10.1146/annurev.neuro.25.112701.142758

Marek, S., Tervo-Clemmens, B., Calabro, F.J., Montez, D.F., Kay, B.P., Hatoum, A.S., Donohue, M.R., Foran, W., Miller, R.L., Hendrickson, T.J., Malone, S.M., Kandala, S., Feczko, E., Miranda-Dominguez, O., Graham, A.M., Earl, E.A., Perrone, A.J., Cordova, M., Doyle, O., Moore, L.A., Conan, G.M., Uriarte, J., Snider, K., Lynch, B.J., Wilgenbusch, J.C., Pengo, T., Tam, A., Chen, J., Newbold, D.J., Zheng, A., Seider, N.A., Van, A.N., Metoki, A., Chauvin, R.J., Laumann, T.O., Greene, D.J., Petersen, S.E., Garavan, H., Thompson, W.K., Nichols, T.E., Yeo, B.T.T., Barch, D.M., Luna, B., Fair, D.A., Dosenbach, N.U.F., 2022. Reproducible brain-wide association studies require thousands of individuals. Nature 603, 654–660. https://doi.org/10.1038/s41586-022-04492-9

Matsumoto, H., Ugawa, Y., 2020. Quadripulse stimulation (QPS). Exp. Brain Res. 238, 1619–1625. https://doi.org/10.1007/s00221-020-05788-w

McNab, J.A., Polimeni, J.R., Wang, R., Augustinack, J.C., Fujimoto, K., Stevens, A., Triantafyllou, C., Janssens, T., Farivar, R., Folkerth, R.D., Vanduffel, W., Wald, L.L., 2013. Surface based analysis of diffusion orientation for identifying architectonic domains in the in vivo human cortex. Neuroimage 69, 87–100. https://doi.org/10.1016/j.neuroimage.2012.11.065

Meng, Q., Nguyen, H., Vrana, A., Baldwin, S., Li, C.Q., Giles, A., Wang, J., Yang, Y., Lu, H., 2022. A high-density theta burst paradigm enhances the aftereffects of transcranial magnetic stimulation: Evidence from focal stimulation of rat motor cortex. Brain Stimul. 15, 833–842. https://doi.org/10.1016/j.brs.2022.05.017

Menon, V., Uddin, L.Q., 2010. Saliency, switching, attention and control: a network model of insula function. Brain Struct. Funct. 214, 655–667. https://doi.org/10.1007/s00429-010-0262-0
Mezer, A., Yeatman, J.D., Stikov, N., Kay, K.N., Cho, N.J., Dougherty, R.F., Perry, M.L., Parvizi, J., Hua, L.H., Butts-Pauly, K., Wandell, B.A., 2013. Quantifying the local tissue volume and composition in individual brains with magnetic resonance imaging. Nat. Med. 19, 1667–1672. https://doi.org/10.1038/nm.3390
Micu, I., Plemel, J.R., Caprariello, A.V., Nave, K.A., Stys, P.K., 2018. Axo-myelinic neurotransmission: A novel mode of cell signalling in the central nervous system. Nat. Rev. Neurosci. 19, 49–57. https://doi.org/10.1038/nrn.2017.128
Mottaghy, F.M., Gangitano, M., Horkan, C., Chen, Y., Pascual-Leone, A., Schlaug, G., 2003. Repetitive TMS temporarily alters brain diffusion. Neurology 60, 1539–1541. https://doi.org/10.1212/01.WNL.0000058903.15205.46
Murtagh, F., Contreras, P., 2012. Algorithms for hierarchical clustering: an overview. Wiley Interdiscip. Rev. Data Min. Knowl. Discov. 2, 86–97. https://doi.org/10.1002/widm.53
Nakajima, R., Kinoshita, M., Shinohara, H., Nakada, M., 2020. The superior longitudinal fascicle: reconsidering the fronto-parietal neural network based on anatomy and function. Brain Imaging Behav. 14, 2817–2830. https://doi.org/10.1007/s11682-019-00187-4
Nakamura, K., Enomoto, H., Hanajima, R., Hamada, M., Shimizu, E., Kawamura, Y., Sasaki, T., Matsuzawa, D., Sutoh, C., Shirota, Y., Terao, Y., Ugawa, Y., 2011. Quadri-pulse stimulation (QPS) induced LTP/LTD was not affected by Val66Met polymorphism in the brain-derived neurotrophic factor (BDNF) gene. Neurosci. Lett. 487, 264–267. https://doi.org/10.1016/j.neulet.2010.10.034
Nakamura, K., Groiss, S.J., Hamada, M., Enomoto, H., Kadowaki, S., Abe, M., Murakami, T., Wiratman, W., Chang, F., Kobayashi, S., Hanajima, R., Terao, Y., Ugawa, Y., 2016. Variability in Response to Quadripulse Stimulation of the Motor Cortex. Brain Stimul. 9, 859–866. https://doi.org/10.1016/j.brs.2016.01.008
Nettekoven, C., Volz, L.J., Kutscha, M., Pool, E.M., Rehme, A.K., Eickhoff, S.B., Fink, G.R., Grefkes, C., 2014. Dose-dependent effects of theta burst rTMS on cortical excitability and resting-state connectivity of the human motor system. Journal of Neuroscience 34, 6849–6859. https://doi.org/10.1523/JNEUROSCI.4993-13.2014
Nettekoven, C., Volz, L.J., Leimbach, M., Pool, E.M., Rehme, A.K., Eickhoff, S.B., Fink, G.R., Grefkes, C., 2015. Inter-individual variability in cortical excitability and motor network connectivity following multiple blocks of rTMS. Neuroimage 118, 209–218. https://doi.org/10.1016/j.neuroimage.2015.06.004
Niehaus, L., Hoffmann, K.T., Grosse, P., Röricht, S., Meyer, B.U., 2000. MRI study of human brain exposed to high-dose repetitive magnetic stimulation of visual cortex. Neurology 54, 256–258. https://doi.org/10.1212/wnl.54.1.256
Oberman, L., 2014. Repetitive Transcranial Magnetic Stimulation (rTMS) Protocols, in: Rotenberg, A., Horvath, J.C., Pascual-Leone, A. (Eds.), Transcranial Magnetic Stimulation. Springer New York, New York, NY, pp. 129–139. https://doi.org/10.1007/978-1-4939-0879-0_7
Oberman, L., Edwards, D., Eldaief, M., Pascual-Leone, A., 2011. Safety of theta burst transcranial magnetic stimulation: a systematic review of the literature. J. Clin. Neurophysiol. 28, 67–74. https://doi.org/10.1097/WNP.0b013e318205135f
Ogawa, S., Lee, T.M., Kay, A.R., Tank, D.W., 1990. Brain magnetic resonance imaging with contrast dependent on blood oxygenation. Proc. Natl. Acad. Sci. U. S. A. 87, 9868–9872. https://doi.org/10.1073/pnas.87.24.9868
Oishi, H., Takemura, H., Amano, K., 2020. Macromolecular tissue volume mapping of lateral

geniculate nucleus subdivisions in living human brains. bioRxiv. https://doi.org/10.1101/2020.12.26.424373
Oishi, H., Takemura, H., Aoki, S.C., Fujita, I., Amano, K., 2018. Microstructural properties of the vertical occipital fasciculus explain the variability in human stereoacuity. Proc. Natl. Acad. Sci. U. S. A. 115, 12289–12294. https://doi.org/10.1073/pnas.1804741115
Oldfield, R.C., 1971. The assessment and analysis of handedness: the Edinburgh inventory. Neuropsychologia 9, 97–113. https://doi.org/10.1016/0028-3932(71)90067-4
Owen, J.P., Chang, Y.S., Pojman, N.J., Bukshpun, P., Wakahiro, M.L.J., Marco, E.J., Berman, J.I., Spiro, J.E., Chung, W.K., Buckner, R.L., Roberts, T.P.L., Nagarajan, S.S., Sherr, E.H., Mukherjee, P., Simons VIP Consortium, 2014. Aberrant white matter microstructure in children with 16p11.2 deletions. J. Neurosci. 34, 6214–6223. https://doi.org/10.1523/JNEUROSCI.4495-13.2014
Ozdemir, R.A., Boucher, P., Fried, P.J., Momi, D., Jannati, A., Pascual-Leone, A., Santarnecchi, E., Shafi, M.M., 2021. Reproducibility of cortical response modulation induced by intermittent and continuous theta-burst stimulation of the human motor cortex. Brain Stimulation. https://doi.org/10.1016/j.brs.2021.05.013
Palacios, E.M., Owen, J.P., Yuh, E.L., Wang, M.B., Vassar, M.J., Ferguson, A.R., Diaz-Arrastia, R., Giacino, J.T., Okonkwo, D.O., Robertson, C.S., Stein, M.B., Temkin, N., Jain, S., McCrea, M., MacDonald, C.L., Levin, H.S., Manley, G.T., Mukherjee, P., TRACK-TBI Investigators, 2020. The evolution of white matter microstructural changes after mild traumatic brain injury: A longitudinal DTI and NODDI study. Sci Adv 6, eaaz6892. https://doi.org/10.1126/sciadv.aaz6892
Park, S.H., Russ, B.E., McMahon, D.B.T., Koyano, K.W., Berman, R.A., Leopold, D.A., 2017. Functional Subpopulations of Neurons in a Macaque Face Patch Revealed by Single-Unit fMRI Mapping. Neuron 95, 971–981.e5. https://doi.org/10.1016/j.neuron.2017.07.014
Pascual-Leone, A., Valls-Solé, J., Wassermann, E.M., Hallett, M., 1994. Responses to rapid-rate transcranial magnetic stimulation of the human motor cortex. Brain 117 (Pt 4), 847–858. https://doi.org/10.1093/brain/117.4.847
Platz, T., Adler-Wiebe, M., Roschka, S., Lotze, M., 2018. Enhancement of motor learning by focal intermittent theta burst stimulation (iTBS) of either the primary motor (M1) or somatosensory area (S1) in healthy human subjects. Restor. Neurol. Neurosci. 36, 117–130. https://doi.org/10.3233/RNN-170774
Power, J.D., Mitra, A., Laumann, T.O., Snyder, A.Z., Schlaggar, B.L., Petersen, S.E., 2014. Methods to detect, characterize, and remove motion artifact in resting state fMRI. Neuroimage 84, 320–341. https://doi.org/10.1016/j.neuroimage.2013.08.048
Puig, J., Blasco, G., Schlaug, G., Stinear, C.M., Daunis-I-Estadella, P., Biarnes, C., Figueras, J., Serena, J., Hernández-Pérez, M., Alberich-Bayarri, A., Castellanos, M., Liebeskind, D.S., Demchuk, A.M., Menon, B.K., Thomalla, G., Nael, K., Wintermark, M., Pedraza, S., 2017. Diffusion tensor imaging as a prognostic biomarker for motor recovery and rehabilitation after stroke. Neuroradiology 59, 343–351. https://doi.org/10.1007/s00234-017-1816-0
Purves, 2017. Neuroscience 6th Edition. Oxford University Press, Incorporated.
Rabinovich, M.I., Varona, P., 2011. Robust transient dynamics and brain functions. Front. Comput. Neurosci. 5, 24. https://doi.org/10.3389/fncom.2011.00024
Rafiei, F., Rahnev, D., 2022. TMS Does Not Increase BOLD Activity at the Site of Stimulation: A Review of All Concurrent TMS-fMRI Studies. eNeuro 9. https://doi.org/10.1523/ENEURO.0163-22.2022
Reti, I., 2015. Brain Stimulation: Methodologies and Interventions. John Wiley & Sons.
Ridding, M.C., Ziemann, U., 2010. Determinants of the induction of cortical plasticity by

non-invasive brain stimulation in healthy subjects: Induction of cortical plasticity by non-invasive brain stimulation. J. Physiol. 588, 2291–2304. https://doi.org/10.1113/jphysiol.2010.190314
Robinson, E.C., Garcia, K., Glasser, M.F., Chen, Z., Coalson, T.S., Makropoulos, A., Bozek, J., Wright, R., Schuh, A., Webster, M., Hutter, J., Price, A., Cordero Grande, L., Hughes, E., Tusor, N., Bayly, P.V., Van Essen, D.C., Smith, S.M., Edwards, A.D., Hajnal, J., Jenkinson, M., Glocker, B., Rueckert, D., 2018. Multimodal surface matching with higher-order smoothness constraints. Neuroimage 167, 453–465. https://doi.org/10.1016/j.neuroimage.2017.10.037
Robinson, E.C., Jbabdi, S., Glasser, M.F., Andersson, J., Burgess, G.C., Harms, M.P., Smith, S.M., Van Essen, D.C., Jenkinson, M., 2014. MSM: a new flexible framework for Multimodal Surface Matching. Neuroimage 100, 414–426. https://doi.org/10.1016/j.neuroimage.2014.05.069
Romei, V., Chiappini, E., Hibbard, P.B., Avenanti, A., 2016. Empowering Reentrant Projections from V5 to V1 Boosts Sensitivity to Motion. Curr. Biol. 26, 2155–2160. https://doi.org/10.1016/j.cub.2016.06.009
Rosenberg, M.D., Finn, E.S., 2022. How to establish robust brain–behavior relationships without thousands of individuals. Nat. Neurosci. 25, 835–837. https://doi.org/10.1038/s41593-022-01110-9
Rosenberg, M.D., Finn, E.S., Scheinost, D., Papademetris, X., Shen, X., Constable, R.T., Chun, M.M., 2016. A neuromarker of sustained attention from whole-brain functional connectivity. Nat. Neurosci. 19, 165–171. https://doi.org/10.1038/nn.4179
Rossini, P.M., Burke, D., Chen, R., Cohen, L.G., Daskalakis, Z., Di Iorio, R., Di Lazzaro, V., Ferreri, F., Fitzgerald, P.B., George, M.S., Hallett, M., Lefaucheur, J.P., Langguth, B., Matsumoto, H., Miniussi, C., Nitsche, M.A., Pascual-Leone, A., Paulus, W., Rossi, S., Rothwell, J.C., Siebner, H.R., Ugawa, Y., Walsh, V., Ziemann, U., 2015. Non-invasive electrical and magnetic stimulation of the brain, spinal cord, roots and peripheral nerves: Basic principles and procedures for routine clinical and research application. An updated report from an I.F.C.N. Committee. Clin. Neurophysiol. 126, 1071–1107. https://doi.org/10.1016/j.clinph.2015.02.001
Rounis, E., Huang, Y.Z., 2020. Theta burst stimulation in humans: a need for better understanding effects of brain stimulation in health and disease. Exp. Brain Res. 238, 1707–1714. https://doi.org/10.1007/s00221-020-05880-1
Sagi, Y., Tavor, I., Hofstetter, S., Tzur-Moryosef, S., Blumenfeld-Katzir, T., Assaf, Y., 2012. Learning in the Fast Lane: New Insights into Neuroplasticity. Neuron 73, 1195–1203. https://doi.org/10.1016/j.neuron.2012.01.025
Sampaio-Baptista, C., Johansen-Berg, H., 2017. White Matter Plasticity in the Adult Brain. Neuron 96, 1239–1251. https://doi.org/10.1016/j.neuron.2017.11.026
Sampaio-Baptista, C., Neyedli, H.F., Sanders, Z.-B., Diosi, K., Havard, D., Huang, Y., Andersson, J.L.R., Lühr, M., Goebel, R., Johansen-Berg, H., 2021. fMRI neurofeedback in the motor system elicits bidirectional changes in activity and in white matter structure in the adult human brain. Cell Rep. 37, 109890. https://doi.org/10.1016/j.celrep.2021.109890
Scholz, J., Klein, M.C., Behrens, T.E.J., Johansen-Berg, H., 2009. Training induces changes in white-matter architecture. Nat. Neurosci. 12, 1370–1371. https://doi.org/10.1038/nn.2412
Schulz, R., Wessel, M.J., Zimerman, M., Timmermann, J.E., Gerloff, C., Hummel, F.C., 2015. White Matter Integrity of Specific Dentato-Thalamo-Cortical Pathways is Associated with Learning Gains in Precise Movement Timing. Cereb. Cortex 25, 1707–1714. https://doi.org/10.1093/cercor/bht356

Shih, Y.-Y.I., Wey, H.-Y., De La Garza, B.H., Duong, T.Q., 2011. Striatal and cortical BOLD, blood flow, blood volume, oxygen consumption, and glucose consumption changes in noxious forepaw electrical stimulation. J. Cereb. Blood Flow Metab. 31, 832–841. https://doi.org/10.1038/jcbfm.2010.173

Siebner, H.R., Funke, K., Aberra, A.S., Antal, A., Bestmann, S., Chen, R., Classen, J., Davare, M., Di Lazzaro, V., Fox, P.T., Hallett, M., Karabanov, A.N., Kesselheim, J., Beck, M.M., Koch, G., Liebetanz, D., Meunier, S., Miniussi, C., Paulus, W., Peterchev, A.V., Popa, T., Ridding, M.C., Thielscher, A., Ziemann, U., Rothwell, J.C., Ugawa, Y., 2022. Transcranial magnetic stimulation of the brain: What is stimulated? - A consensus and critical position paper. Clin. Neurophysiol. 140, 59–97. https://doi.org/10.1016/j.clinph.2022.04.022

Sjöström, P.J., Turrigiano, G.G., Nelson, S.B., 2003. Neocortical LTD via coincident activation of presynaptic NMDA and cannabinoid receptors. Neuron 39, 641–654. https://doi.org/10.1016/s0896-6273(03)00476-8

Smith, S.M., 2002. Fast robust automated brain extraction. Hum. Brain Mapp. 17, 143–155. https://doi.org/10.1002/hbm.10062

Smith, S.M., Beckmann, C.F., Andersson, J., Auerbach, E.J., Bijsterbosch, J., Douaud, G., Duff, E., Feinberg, D.A., Griffanti, L., Harms, M.P., Kelly, M., Laumann, T., Miller, K.L., Moeller, S., Petersen, S., Power, J., Salimi-Khorshidi, G., Snyder, A.Z., Vu, A.T., Woolrich, M.W., Xu, J., Yacoub, E., Uğurbil, K., Van Essen, D.C., Glasser, M.F., WU-Minn HCP Consortium, 2013. Resting-state fMRI in the Human Connectome Project. Neuroimage 80, 144–168. https://doi.org/10.1016/j.neuroimage.2013.05.039

Smith, S.M., Fox, P.T., Miller, K.L., Glahn, D.C., Fox, P.M., Mackay, C.E., Filippini, N., Watkins, K.E., Toro, R., Laird, A.R., Beckmann, C.F., 2009. Correspondence of the brain's functional architecture during activation and rest. Proc. Natl. Acad. Sci. U. S. A. 106, 13040–13045. https://doi.org/10.1073/pnas.0905267106

Smith, S.M., Jenkinson, M., Johansen-Berg, H., Rueckert, D., Nichols, T.E., Mackay, C.E., Watkins, K.E., Ciccarelli, O., Cader, M.Z., Matthews, P.M., Behrens, T.E.J., 2006. Tract-based spatial statistics: voxelwise analysis of multi-subject diffusion data. Neuroimage 31, 1487–1505. https://doi.org/10.1016/j.neuroimage.2006.02.024

Smith, S.M., Miller, K.L., Salimi-Khorshidi, G., Webster, M., Beckmann, C.F., Nichols, T.E., Ramsey, J.D., Woolrich, M.W., 2011. Network modelling methods for FMRI. Neuroimage 54, 875–891. https://doi.org/10.1016/j.neuroimage.2010.08.063

Smith, S.M., Nichols, T.E., 2009. Threshold-free cluster enhancement: addressing problems of smoothing, threshold dependence and localisation in cluster inference. Neuroimage 44, 83–98. https://doi.org/10.1016/j.neuroimage.2008.03.061

Sommer, M., Alfaro, A., Rummel, M., Speck, S., Lang, N., Tings, T., Paulus, W., 2006. Half sine, monophasic and biphasic transcranial magnetic stimulation of the human motor cortex. Clin. Neurophysiol. 117, 838–844. https://doi.org/10.1016/j.clinph.2005.10.029

Sommer, M., Ciocca, M., Chieffo, R., Hammond, P., Neef, A., Paulus, W., Rothwell, J.C., Hannah, R., 2018. TMS of primary motor cortex with a biphasic pulse activates two independent sets of excitable neurones. Brain Stimul. 11, 558–565. https://doi.org/10.1016/j.brs.2018.01.001

Sommer, M., Rummel, M., Norden, C., Rothkegel, H., Lang, N., Paulus, W., 2013. Mechanisms of human motor cortex facilitation induced by subthreshold 5-Hz repetitive transcranial magnetic stimulation. J. Neurophysiol. 109, 3060–3066. https://doi.org/10.1152/jn.01089.2012

Sotiropoulos, S.N., Jbabdi, S., Xu, J., Andersson, J.L., Moeller, S., Auerbach, E.J., Glasser, M.F., Hernandez, M., Sapiro, G., Jenkinson, M., Feinberg, D.A., Yacoub, E., Lenglet, C., Van Essen, D.C., Ugurbil, K., Behrens, T.E.J., WU-Minn HCP Consortium, 2013.

Advances in diffusion MRI acquisition and processing in the Human Connectome Project. Neuroimage 80, 125–143. https://doi.org/10.1016/j.neuroimage.2013.05.057
Soulard, J., Huber, C., Baillieul, S., Thuriot, A., Renard, F., Aubert Broche, B., Krainik, A., Vuillerme, N., Jaillard, A., ISIS-HERMES Group, 2020. Motor tract integrity predicts walking recovery: A diffusion MRI study in subacute stroke. Neurology 94, e583–e593. https://doi.org/10.1212/WNL.0000000000008755
Stefan, K., Kunesch, E., Benecke, R., Cohen, L.G., Classen, J., 2002. Mechanisms of enhancement of human motor cortex excitability induced by interventional paired associative stimulation. J. Physiol. 543, 699–708. https://doi.org/10.1113/jphysiol.2002.023317
Stejskal, E.O., Tanner, J.E., 1965. Spin Diffusion Measurements: Spin Echoes in the Presence of a Time‐Dependent Field Gradient. J. Chem. Phys. 42, 288–292. https://doi.org/10.1063/1.1695690
Stock, B., Shrestha, M., Seiler, A., Foerch, C., Hattingen, E., Steinmetz, H., Deichmann, R., Wagner, M., Gracien, R.M., 2020. Distribution of Cortical Diffusion Tensor Imaging Changes in Multiple Sclerosis. Frontiers in Physiology 11, 1–7. https://doi.org/10.3389/fphys.2020.00116
Stoffers, D., Diaz, B.A., Chen, G., den Braber, A., van ’t Ent, D., Boomsma, D.I., Mansvelder, H.D., de Geus, E., Van Someren, E.J.W., Linkenkaer-Hansen, K., 2015. Resting-State fMRI Functional Connectivity Is Associated with Sleepiness, Imagery, and Discontinuity of Mind. PLoS One 10, e0142014. https://doi.org/10.1371/journal.pone.0142014
Suppa, A., Huang, Y.-Z., Funke, K., Ridding, M.C., Cheeran, B., Di Lazzaro, V., Ziemann, U., Rothwell, J.C., 2016. Ten Years of Theta Burst Stimulation in Humans: Established Knowledge, Unknowns and Prospects. Brain Stimul. 9, 323–335. https://doi.org/10.1016/j.brs.2016.01.006
Suppa, A., Ortu, E., Zafar, N., Deriu, F., Paulus, W., Berardelli, A., Rothwell, J.C., 2008. Theta burst stimulation induces after-effects on contralateral primary motor cortex excitability in humans. J. Physiol. 586, 4489–4500. https://doi.org/10.1113/jphysiol.2008.156596
Szafer, A., Zhong, J., Gore, J.C., 1995. Theoretical model for water diffusion in tissues. Magn. Reson. Med. 33, 697–712. https://doi.org/10.1002/mrm.1910330516
Tavor, I., Botvinik-Nezer, R., Bernstein-Eliav, M., Tsarfaty, G., Assaf, Y., 2020. Short-term plasticity following motor sequence learning revealed by diffusion magnetic resonance imaging. Hum. Brain Mapp. 41, 442–452. https://doi.org/10.1002/hbm.24814
Teo, J.T.H., Swayne, O.B., Rothwell, J.C., 2007. Further evidence for NMDA-dependence of the after-effects of human theta burst stimulation. Clin. Neurophysiol. 118, 1649–1651. https://doi.org/10.1016/j.clinph.2007.04.010
Thomason, M.E., Thompson, P.M., 2011. Diffusion imaging, white matter, and psychopathology. Annu. Rev. Clin. Psychol. 7, 63–85. https://doi.org/10.1146/annurev-clinpsy-032210-104507
Tiksnadi, A., Murakami, T., Wiratman, W., Matsumoto, H., Ugawa, Y., 2020. Direct comparison of efficacy of the motor cortical plasticity induction and the interindividual variability between TBS and QPS. Brain Stimul. 13, 1824–1833. https://doi.org/10.1016/j.brs.2020.10.014
Tomassini, V., Jbabdi, S., Kincses, Z.T., Bosnell, R., Douaud, G., Pozzilli, C., Matthews, P.M., Johansen-Berg, H., 2011. Structural and functional bases for individual differences in motor learning. Hum. Brain Mapp. 32, 494–508. https://doi.org/10.1002/hbm.21037
Tononi, G., Boly, M., Massimini, M., Koch, C., 2016. Integrated information theory: from consciousness to its physical substrate. Nat. Rev. Neurosci. 17, 450–461.

https://doi.org/10.1038/nrn.2016.44
Tremblay, S., Rogasch, N.C., Premoli, I., Blumberger, D.M., Casarotto, S., Chen, R., Di Lazzaro, V., Farzan, F., Ferrarelli, F., Fitzgerald, P.B., Hui, J., Ilmoniemi, R.J., Kimiskidis, V.K., Kugiumtzis, D., Lioumis, P., Pascual-Leone, A., Pellicciari, M.C., Rajji, T., Thut, G., Zomorrodi, R., Ziemann, U., Daskalakis, Z.J., 2019. Clinical utility and prospective of TMS-EEG. Clin. Neurophysiol. 130, 802–844. https://doi.org/10.1016/j.clinph.2019.01.001
Uddin, M.N., Figley, T.D., Figley, C.R., 2018a. Effect of echo time and T2-weighting on GRASE-based T1w/T2w ratio measurements at 3T. Magn. Reson. Imaging 51, 35–43. https://doi.org/10.1016/j.mri.2018.04.012
Uddin, M.N., Figley, T.D., Marrie, R.A., Figley, C.R., for the CCOMS Study Group, 2018b. Can T 1 w/T 2 w ratio be used as a myelin-specific measure in subcortical structures? Comparisons between FSE-based T 1 w/T 2 w ratios, GRASE-based T 1 w/T 2 w ratios and multi-echo GRASE-based myelin water fractions. NMR Biomed. 31, e3868. https://doi.org/10.1002/nbm.3868
Uddin, M.N., Figley, T.D., Solar, K.G., Shatil, A.S., Figley, C.R., 2019. Comparisons between multi-component myelin water fraction, T1w/T2w ratio, and diffusion tensor imaging measures in healthy human brain structures. Sci. Rep. 9, 2500. https://doi.org/10.1038/s41598-019-39199-x
Ugawa, Y., 2012. Motor cortical plasticity in basal ganglia disorders or movement disorders. Basal Ganglia 2, 119–121. https://doi.org/10.1016/j.baga.2012.08.005
Vanbellingen, T., Pastore-Wapp, M., Kübel, S., Nyffeler, T., Schüpfer, A.-C., Kiefer, C., Zizlsperger, L., Lutz, K., Luft, A.R., Walther, S., Bohlhalter, S., 2020. Interhemispheric facilitation of gesturing: A combined theta burst stimulation and diffusion tensor imaging study. Brain Stimul. 13, 457–463. https://doi.org/10.1016/j.brs.2019.12.013
Vinayagamani, S., Sheelakumari, R., Sabarish, S., Senthilvelan, S., Ros, R., Thomas, B., Kesavadas, C., 2021. Quantitative Susceptibility Mapping: Technical Considerations and Clinical Applications in Neuroimaging. J. Magn. Reson. Imaging 53, 23–37. https://doi.org/10.1002/jmri.27058
Vogt, K.E., Canepari, M., 2010. On the Induction of Postsynaptic Granule Cell–Purkinje Neuron LTP and LTD. The Cerebellum. https://doi.org/10.1007/s12311-010-0174-9
Walsh, V., Cowey, A., 2000. Transcranial magnetic stimulation and cognitive neuroscience. Nat. Rev. Neurosci. 1, 73–79. https://doi.org/10.1038/35036239
Watanabe, T., Hanajima, R., Shirota, Y., Ohminami, S., Tsutsumi, R., Terao, Y., Ugawa, Y., Hirose, S., Miyashita, Y., Konishi, S., Kunimatsu, A., Ohtomo, K., 2014. Bidirectional effects on interhemispheric resting-state functional connectivity induced by excitatory and inhibitory repetitive transcranial magnetic stimulation. Hum. Brain Mapp. 35, 1896–1905. https://doi.org/10.1002/hbm.22300
Wessel, M.J., Draaisma, L.R., Morishita, T., Hummel, F.C., 2019. The effects of stimulator, waveform, and current direction on intracortical inhibition and facilitation: A TMS comparison study. Front. Neurosci. 13, 703. https://doi.org/10.3389/fnins.2019.00703
Wiratman, W., Murakami, T., Kobayashi, S., Enomoto, H., Ugawa, Y., 2017. Paired associative quadripulse stimulation (PAS-QPS) - a new protocol combining homo- and hetero-synaptic plasticity. Brain Stimul. 10, 395. https://doi.org/10.1016/j.brs.2017.01.170
Wriessnegger, S.C., Bauernfeind, G., Schweitzer, K., Kober, S., Neuper, C., Müller-Putz, G.R., 2012. The interplay of prefrontal and sensorimotor cortices during inhibitory control of learned motor behavior. Front. Neuroeng. 5, 17. https://doi.org/10.3389/fneng.2012.00017
Yarrow, K., Brown, P., Krakauer, J.W., 2009. Inside the brain of an elite athlete: the neural

processes that support high achievement in sports. Nat. Rev. Neurosci. 10, 585–596. https://doi.org/10.1038/nrn2672
Yi, S.Y., Stowe, N.A., Barnett, B.R., Dodd, K., Yu, J.-P.J., 2020. Microglial Density Alters Measures of Axonal Integrity and Structural Connectivity. Biol Psychiatry Cogn Neurosci Neuroimaging 5, 1061–1068. https://doi.org/10.1016/j.bpsc.2020.04.008
Zhang, H., Schneider, T., Wheeler-Kingshott, C.A., Alexander, D.C., 2012. NODDI: Practical in vivo neurite orientation dispersion and density imaging of the human brain. Neuroimage 61, 1000–1016. https://doi.org/10.1016/j.neuroimage.2012.03.072
Zhong, J., Petroff, O.A., Prichard, J.W., Gore, J.C., 1993. Changes in water diffusion and relaxation properties of rat cerebrum during status epilepticus. Magn. Reson. Med. 30, 241–246. https://doi.org/10.1002/mrm.1910300214
Zhou, K., Stawicki, T.M., Goncharov, A., Jin, Y., 2013. Position of UNC-13 in the active zone regulates synaptic vesicle release probability and release kinetics. Elife 2, e01180. https://doi.org/10.7554/eLife.01180
Zucker, R.S., Regehr, W.G., 2002. Short-term synaptic plasticity. Annu. Rev. Physiol. 64, 355–405. https://doi.org/10.1146/annurev.physiol.64.092501.114547

Chapter 6. Acknowledgement

First of all, I would like to express my sincere gratitude to my mentor, Prof. Kaoru Amano, for his thorough support and guidance for this thesis. The fruitful discussions with him have inspired me a lot.

I am also thankful to Prof. Toshio Yanagida and Prof. Shigeru Kitzawa for creating and maintaining such a wonderful research environment at CiNet. Besides, Prof. Shigeru Kitzawa was also my previous mentor at MD Researcher Training Program, Faculty of Medicine, Osaka University. I learnt many important things from him, including conducting psychological experiments and neuroimaging research; performing statistical testing and programming; and performing oral and poster presentations. Without his guidance, I would never have considered doing research in this field.

I would like to thank Prof. Yoshikazu Ugawa, Dr. Masamichi J. Hayashi, Dr. Koichi Hosomi, and Dr. Nobuhiko Mori. They told me how to do the rTMS experiment. I would also like to thank Dr. Tomoya Kawashima and Dr. Hiroki Oishi for their helpful comments and kind advice on my analysis, presentation, and paper of my research. I would also like to thank Dr. Ian Greenhouse for guiding me to apply his toolbox to the output of BrainSight.

I am also grateful to the staff of the department of Neurology at Osaka University, especially: Prof. Hideki Mochizuki, Dr. Tatsusada Okuno, and Dr. Yuta Kajiyama. Without them, I would never have imagined taking a step into the clinical research of neurology.

I would like to thank my other lecturers, especially Prof. Yasufumi Kaneda, Prof. Yasushi Okamura, Prof. Toshihide Yamashita, Prof. Shoichi Shimada, Prof. Makoto Sato, and Prof. Manabu Ikeda. My current research is largely based on the knowledge gained from their lectures.

I also thank my previous/present supervisors and colleagues, particularly Dr. Tamami Nakano, Dr. Toshimitsu Takahashi, Dr. Motoaki Uchimura, Dr. Hiroki Kumano, Dr.

Nobuyuki Nishimura, Dr. Tomoko Isomura, Dr. Yuki Kakuda, Dr. Mayuka Abe, Dr. Junya Asai, Dr. Tang Long, Prof. Watabe Kenji, Dr. Mitsuhiro Yamaguchi, Dr. Hideyuki Kanai, Dr. Fumihisa Soga, Dr. Yosuke Kokunai, Dr. Rika Yamashita, Dr. Shota Segawa, Dr. Tomoya Wadayama, Dr. Takahiro Ajiki, Dr. Masaichi Nakamura, Prof. Noriaki Hattori, Dr. Toru Koda, Dr. Yasuyoshi Kimura, Dr. Gajanan S. Revankar, Dr. Yuko Yokoro, Dr. Hiroshi Miyawaki, Dr. Mitsuaki Takemi, Dr. Ryohei Nakayama, Dr. Ayumu Yamashita, Dr. Shuka Shibusawa, and Masakazu Sugimoto. I owe them a lot for their daily conversation and helpful advice regarding scientific or clinical topics, career as a scientist, and daily lives. Finally, I am thankful to my old friends and family, especially my beloved wife, Ena Kimura, for their understanding and continuous support for me to do the basic research.

Chapter 7. Achievements

7.1 Related to this thesis

PEER-REVIEW JOURNAL ARTICLES

Kimura, I., Oishi, H., Hayashi, M.J., Amano K. Microstructural properties of human brain revealed by fractional anisotropy can predict the after-effect of intermittent theta burst stimulation. *Cerebral Cortex Communications*, 3(1), 1-11, 2021

Kimura, I., Ugawa, Y., Hayashi, M.J., Amano K. Quadripulse stimulation: A replication study with a newly developed stimulator. *Brain Stimulation*, 15(3), 579-581, 2022

INTERNATIONAL CONFERENCES

Poster presentation

Kimura, I., Oishi, H., Hayashi M.J., Amano, K., 2021, Predicting the response to intermittent theta burst stimulation (iTBS) from the microstructural properties of the white matter, Cognitive Neuroscience Society 2021 Virtual Meeting, Online, March 2021

Kimura, I., Oishi, H., Hayashi M.J., Amano, K., 2021, The microstructural changes in human brain induced by intermittent theta burst stimulation, Brain Box Initiative Conference 2021, Online, September 2021

DOMESTIC CONFERENCES

Invited talk

木村一皓、脳の微細構造による rTMS の事後効果の予測、第52回日本臨床神経生理学会学術大会、京都、2022年11月

Oral presentation

木村一皓、大石浩輝、林正道、天野薫、間欠的シータバースト刺激による脳の微細構造の変化と運動誘発電位の変化の関連性、第51回日本臨床神経生理学会学術大会、仙台、2021年12月

Poster presentation

木村一皓、大石浩輝、林正道、天野薫、間欠的シータバースト刺激による運動誘発電位の変化と白質の微細構造の関連性、第23回日本ヒト脳機能マッピング学会、オンライン、2021年3月

木村一皓、大石浩輝、林正道、天野薫、間欠的シータバースト刺激による運動誘発電位の変化と脳微細構造との関連性、第2回時間生成学領域会議、オンライン、2021年1月

AWARDS

奨励賞, 第2回時間生成学領域会議, 2021年1月

若手奨励賞, 第23回ヒト脳機能マッピング学会, 2021年3月

7.2 Other achievements

PREPRINT

Kimura, I., Revankar, G.S., Ogawa, K., Amano, K., Kajiyama, Y., Mochizuki, H. Neural Correlates of Impulsive Compulsive Behaviors in Parkinson's Disease: A Japanese Retrospective Study. *medRxiv*, 2022

INTERNATIONAL CONFERENCES

Poster presentation

Kimura, I., Kajiyama, Y., Revankar, G.S., Ogawa, K., Amano, K., Mochizuki, H. Neuroimaging characteristics of impulse control disorders and dopamine dysregulation syndrome in Parkinson’s Disease. Neuroscience 2022, USA, November 2022

DOMESTIC CONFERENCES

Poster presentation

木村一皓、梶山裕太、Revankar S. Gajanan、小河浩太郎、天野薫、望月秀樹、パーキンソン病に伴う衝動的行動における機能的結合の解析－本邦での後方視的検討、第24回日本ヒト脳機能マッピング学会、オンライン、2022年2月

木村一皓、梶山裕太、Revankar S. Gajanan、小河浩太郎、天野薫、望月秀樹、パーキンソン病に伴う衝動的行動の神経基盤－本邦での後方視的検討、NEURO2022、沖縄、2022年6月

AWARDS

JNS-SfN Exchange Travel Award, Neuroscience 2022, 2022年11月